DESIGN, FABRICATION AND TESTING OF AN ACOUSTIC RESONATOR-BASED BIOSENSOR FOR THE DETECTION OF CANCER BIOMARKERS

A Thesis
Presented to
The Academic Faculty

by

Anthony Dickherber

In Partial Fulfillment
of the Requirements for the Degree
Doctorate of Philosophy in the
School of Electrical and Computer Engineering

Georgia Institute of Technology
December 2008

DESIGN, FABRICATION AND TESTING OF AN ACOUSTIC RESONATOR-BASED BIOSENSOR FOR THE DETECTION OF CANCER BIOMARKERS

Approved by:

Dr. William Hunt, Advisor
School of Electrical and Computer Engineering
Georgia Institute of Technology

Dr. Robert Butera
School of Electrical and Computer Engineering
Georgia Institute of Technology

Dr. Peter Hesketh
School of Mechanical Engineering
Georgia Institute of Technology

Dr. Alfred Merrill
School of Biology
Georgia Institute of Technology

Dr. John Petros
Winship Cancer Institute
Emory University

Date Approved: October 28, 2008

DESIGN, FABRICATION AND TESTING OF AN ACOUSTIC RESONATOR-BASED BIOSENSOR FOR THE DETECTION OF CANCER BIOMARKERS

Approved by:

Dr. William Hunt, Advisor
School of Electrical & Computer Engineering
Georgia Institute of Technology

Dr. Alfred Merrill
School of Biology
Georgia Institute of Technology

Dr. Robert Butera
School of Electrical & Computer Engineering
Georgia Institute of Technology

Dr. John Petros
Winship Cancer Institute
Emory University

Dr. Peter Hesketh
School of Mechanical Engineering
Georgia Institute of Technology

Date Approved: October 28, 2008

ACKNOWLEDGEMENTS

I would like to first acknowledge the incredible assistance I've received toward completion of this thesis research from all of my friends, family, research colleagues, and my generous thesis committee. There are so many individuals that have contributed significantly towards whatever success I have been able to achieve, I must insist on not trying to name them, lest I forget any or leave any impression that some contributions were of less significance. I must, however, acknowledge those individuals that have had the greatest impact on the accomplishments summarized in this thesis.

First I must acknowledge the incredibly stimulating and absolutely supportive work environment provided by the Microelectronic Acoustics Group, run by Professor William Hunt. I am particularly in debt to Professor Hunt, for giving me so many opportunities over the course of this research, and for providing me with great leadership and mentorship that I will never forget. A very special thank you I must extend to Christopher Corso, with whom I worked very closely over the last several years. He is a brilliant man, a hard worker, and a true friend. I am truly thankful to all group members, past and present, including Shawn Pinkett, Desmond Stubbs, Sang Hun Lee, Ryan Westafer, Eric Massey, Farasat Munir, Adam Wathen, John Perng, Steve Ruff, Alice Wang, Stephen Welch and Sean McGee. From this distinguished group, I have always gotten the inspiration, stimulation, and validation I have needed to keep on progressing.

I must also thank my parents and my sister for always letting me believe that there was nothing I couldn't do. Finally, I must thank my loving wife who has supported me in every way possible over the course of this research. This absolutely would have been impossible without her.

TABLE OF CONTENTS

LIST OF TABLES

LIST OF FIGURES

Page

Page

Page

Page

LIST OF ABBREVIATIONS

AA	Amino Acid
AACR	American Association for Cancer Research
Ab	Antibody
AFM	Atomic Force Microscopy
ANOVA	Analysis of Variance
APS	3-Aminopropyl triethoxy Silane
AUC	Area Under the Curve
BAW	Bulk Acoustic Wave
BMI	Body Mass Index
BPH	Benign Prostatic Hyperplasia
BVD	Butterworth-Van Dyke
CDMRP	Congressionally Directed Medical Research Program
CM	Conditioned Medium
CVD	Chemical Vapor Deposition
DI H_2O	Deionized Water
DNA	Deoxy-ribonucleic Acid
ELISA (EIA)	Enzyme Linked Immunosorbent Assay
EPCA	Early Prostate Cancer Antigen
FBAR	Thin Film Bulk Acoustic Resonator
FITC	Fluorscein Isothiocyanate
FWHM	Full Width at Half Maximum
GHz	Gigahertz (10^9)
GMBS	N-γ-maleimido Butyryloxy Succinimide Ester

GPS	3-Glycidoxy-Propyl trimethoxy Silane
HMDS	Hexamethyldisilazane
HPLC	High Performance Liquid Chromatography
IC	Integrated Circuit
IDT	Interdigitated Transducers
IgX	Immunoglobulin X
kHz	Kilohertz (10^3)
LFE	Lateral Field Excitation
mAb	Monoclonal Antibody
MHz	Megahertz (10^6)
MOCVD	Metal-organic CVD
MPF	Megakaryocyte Potentiating Factor
MTS	3-Mercapto-propyl Trimethoxy Silane
NCI	National Cancer Institute
NIH	National Institutes of Health
NOC	Non-Organ Confined
OC	Organ Confined
PAP	Prostatic Acid Phosphatase
PBS	Phosphate Buffer Solution
PCa	Prostate Cancer
PCB	Printed Circuit Board
PCR	Polymerase Chain Reaction
PCRP	Prostate Cancer Research Program
PSA	Prostate Specific Antigen
PVD	Plasma Vapor Deposition

QCM	Quartz Crystal Microbalance
RF	Radio Frequency
RGB	Red Green Blue
RNA	Ribonucleic Acid
ROC	Receiver Operator Characteristic
S_{11}	Reflection Scattering Response
SAM	Self-Assembled Monolayer
SAW	Surface Acoustic Wave
SELEX	Systematic Evolution of Ligands by Expontial Enrichment
SEM	Scanning Electron Microscope
SHH	Sonic Hedge Hog
SH-SAW	Shear Horizontal SAW
SMR	Solidly Mounted Resonator
SPR	Surface Plasmon Resonance
TCE	Trichloro Ethylene
TCF	Temperature Coefficient of Resonant Frequency
TE	Thickness Excitation
TFE	Thermally Assisted Field Emission
TSM	Thickness Shear Mode
USAMRMC	United States Army Medical Research and Materiel Command
USFDA	United States Food and Drug Administration
VDC	Voltage DC
WCA	Water Contact Angle
XRD	X-ray Diffraction

SUMMARY

The objective of this thesis research is to develop microelectronic acoustic technology towards biosensor applications. The development of a simple and robust resonator that employs simple microelectronic fabrication techniques for its construction could provide the foundation for a cost-effective sensor platform. Subsequent development of an appropriate surface chemistry treatment would functionalize the resonator as a biosensor. Implementation of this design in an array configuration allows for the development of ligand microarrays, which subsequently allows for multi-ligand recognition signatures as well as testing redundancy. The applications for such a tool extend to a myriad of applications, but the focus of this research is to develop this technology towards an early cancer detection capability.

Specifically, I develop a solidly-mounted resonator with thin-film ZnO as my active piezoelectric layer. These resonators undergo an extensive development process to arrive at a final device design and are fully characterized throughout by X-ray diffraction and scattering analysis. Employing silane chemistry, these resonators are functionalized as immunosensors by covalently binding antibodies to the surface of the device. The quality of the surface chemistry is fully assessed using water contact angle, atomic force microscopy and confocal laser scanning microscopy. Functionalized biosensors are then used to quantify the concentration of known proteins marker in both a purified medium and a physiologically-relevant medium.

CHAPTER 1

INTRODUCTION

The objective of my research was to develop a biosensor technology appropriate for application towards the early detection of cancer. Biosensors can generally be broken down as follows: (shown in Figure 1.1)

1. A specific molecular recognition event (generally achieved by an immobilized capture agent) occurs at a particular location due to exposure of the sensor to a sample medium
2. This event causes a change in the operation of an adjacent or otherwise proximal transducer.
3. The change in operating conditions of that transducer is detected by associated electronic detection equipment.

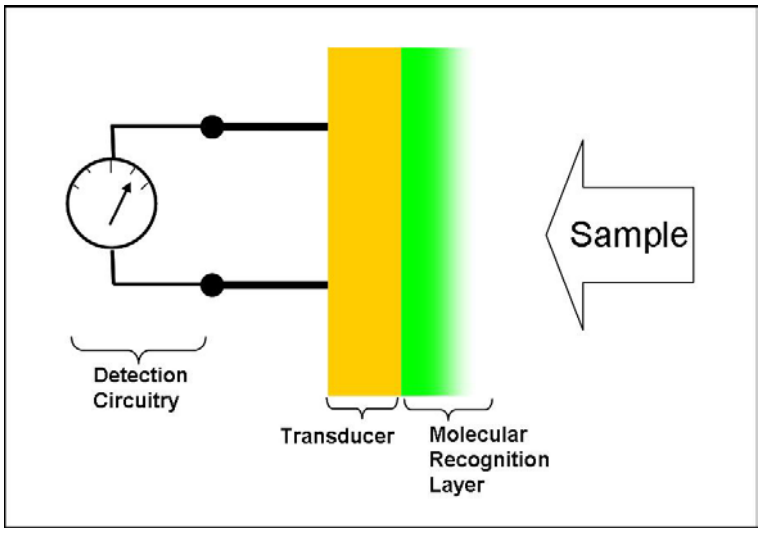

Figure 1.1. Principles of a biosensor.

Given that prostate cancer represents one of the best understood at the earliest stages of development, I will focus on application of this sensor towards detection of prostate cancer relevant biomarkers. The overall goal, therefore, is to develop a microelectronic acoustic sensor design that will lead to point-of-care, label-free detection capability with the following three attributes:

1. a cost-effective design that allows for simple mass production using currently available facilities;
2. a sensor capable of sufficient sensitivity and selectivity to detect targets at pathologically relevant concentrations in physiologically relevant media; and
3. a simple sensing protocol that accommodates little training and near real-time response while minimizing false negatives and false positives.

There exist many problems to be solved in accomplishing such a system. For such an early detection system to be useful for broader clinical diagnostic applications, the sensor design must be highly cost effective. The microelectronics industry has made extraordinary progress in pushing economies of scale to reduce the price of any hardware produced by microelectronic fabrication. A sensor can be developed that takes advantage of the use of these techniques. Medical diagnostics are generally made more expensive by the duration and complexity of the testing protocol. The more complex the system, the greater the qualifications required of the technician performing the test, generally increasing the cost. Development of a near real-time reporting system that requires little training to perform would significantly mitigate these costs.

The applications for such a sensor technology are extensive. In the field of cancer treatment alone, such sensors could be used for early diagnosis, post-treatment monitoring, and by proteomics researchers for new marker exploration and validation. Beyond cancer research, such devices could be employed for everything from battlefield chemical weapons detection, to narcotics and explosives detection, to water quality monitoring [1-3].

I will demonstrate significant progress towards realizing such a tool. Specifically, contributions by the author include:

A. The development of a novel thickness shear mode bulk acoustic resonator array utilizing zinc oxide (ZnO).
B. The novel application of an appropriate surface chemistry protocol for functionalization of planar ZnO with monoclonal antibodies.
C. Combination of these two and demonstration of capability as a sensor.

The first point represents an original contribution by the author that simultaneously addresses points 1-3 enlisted on page 2 of this dissertation. The resonator design can be fabricated with existing microelectronic fabrication equipment with a small footprint, easily implemented in a microarray configuration. The device array can easily yield as many as 1,000 arrays with eight devices each on a single 3-inch wafer. Further, the design is such that it could be fabricated on nearly any polished substrate. The second point is also an original contribution by the author, allowing for the application of the resonators developed as biosensors, as well as the functionalization of any other ZnO-

based transducer. As neither of the first two components had ever existed before, the third point is obviously another original contribution by the author. The accomplishments listed above have led to the following peer-reviewed publications:

- Christopher D Corso, Anthony Dickherber, William D. Hunt, 'An investigation of antibody immobilization methods employing organosilanes on planar crystalline ZnO surfaces for biosensor applications,' *Biosensors & Bioelectronics* 2008, Article in Press

- Cleon Davis, Anthony Dickherber, William D. Hunt, Gary S. May, 'In-Situ acoustic temperature measurement during variable frequency microwave curing,' *IEEE Transactions on Electronics Packaging Manufacturing*, 2008, Article in Press

- Anthony Dickherber, Christopher D Corso, William D. Hunt, 'Optimization and characterization of a ZnO biosensor array,' *Sensors & Actuators A: Physics*, 144(1) pg 7-12, May 28, 2008

- Christopher D Corso, Anthony Dickherber (joint first author), William D. Hunt, 'Lateral field excitation of thickness shear mode waves in a thin film ZnO solidly mounted resonator,' *Journal of Applied Physics*, 101, 054514, 2007
  - Article was independently selected for publication in the *Virtual Journal of Biological Physics Research*, May 2007, indicating recognition of the potential impact of this research

the following conference presentations:

- Anthony Dickherber, Christopher D Corso, William D. Hunt, 'Stability of a RF sputtered ZnO solidly mounted resonator sensor in varying temperature and conductivity environments,' *IEEE Sensors Conference*, Atlanta, GA Oct 30 2007

- Anthony Dickherber, Christopher D Corso, William D. Hunt, 'Dual Mode Sensing,' *IEEE Engineering in Medicine and Biology Conference*, NYC NY, Sept 2 2006

- Anthony Dickherber, William D. Hunt, 'Towards integration of ZnO resonator components with GaAs microelectronics,' *Motorola University Partnership in Research Program Conference*, Chicago IL, Oct 2004

and the following professional poster presentations:

- Anthony Dickherber, Christopher D. Corso, John Petros, William D. Hunt, 'A microelectronic bulk acoustic wave biosensor array for the detection of PSA in

complex solutions,' *2008 Annual Meeting of American Association for Cancer Research*, San Diego, CA, April 10-16, 2008

- Christopher D. Corso, Anthony Dickherber, and William D. Hunt, 'A thickness shear mode zinc oxide liquid sensor with off-axis excitation,' *IEEE Sensors Conference*, Atlanta GA, Oct 29-31 2007

- Anthony J. Dickherber, Christopher D. Corso, William D. Hunt, Ira Pastan, Mitchell Ho, Raffit Hassan, 'Mesothelin-fc fusion protein detection using a novel microelectronic acoustic sensor platform,' *2007 AACR International Conference on Molecular Diagnostics in Cancer Therapeutic Development*, Atlanta, GA Sept 17-20, 2007

- Anthony Dickherber, William Hunt, 'Breaking Down Cost Barriers to Improve Public Health,' *The Sam Nunn Bank of America Policy Forum*, Atlanta, GA March 27 2006

- Christopher Corso, Anthony Dickherber, Payal Shah, Alexandra Migdal, Milton Datta, Sumana Datta, William Hunt, 'Development of a Simple Inexpensive Bulk Acoustic Wave Nanosensor for Cancer Biomarkers: Detection of Secreted Sonic Hedgehog from Prostate Cancer Cells,' *2006 Annual Meeting of American Association for Cancer Research*, Washington DC, April 4, 2006

- William Hunt, Christopher Corso, Anthony Dickherber, 'Piezoelectric Bulk Acoustic Wave Biosensors for Real-Time Biomarker Detection in Complex Media,' *Moving Biosensors to Point-of-Care Cancer Diagnostics* (National Cancer Institute Conference), Rockville, MD, June 8-9, 2005

In addition, this research was supported by a pre-doctoral training award to the author of $67,824 from the US Army Medical Research and Materiel Command's (USAMRMC) Prostate Cancer Research Program (PCRP). The USAMRMC is a research initiative of the Congressionally Directed Medical Research Program (CDMRP).

I will begin with a discussion of the need for a tool that meets the criteria described at the beginning of this chapter and lay out the specific aims of this thesis research. In Chapter 2, I will explore the advantages of acoustic wave biosensors, as opposed to alternative transducer technologies, and discuss the principles of their operation. Chapter 3 will include a theoretically confirmation of the proposed acoustic wave transducer (or

resonator) and the subsequent development of that design. In Chapter 4 I will discuss the challenges of developing an appropriate molecular recognition layer for the resonator followed by a thorough characterization of the chosen protocol. Chapter 5 will demonstrate the performance of the device in various sensor applications and challenges therein. Chapter 6 will provide a concluding discussion of the accomplishments made.

Motivation

President Richard Nixon launched the US war against cancer in his 1971 State of the Union Address, in which he pledged an extraordinary boost to the National Cancer Institute's (NCI) budget and granted cancer researchers the US Army's Fort Detrick as a research center [4]. Considered his most significant act was the signing of the National Cancer Act later that year, at which time he famously declared, "I hope in the years ahead we will look back on this action today as the most significant action taken during my Administration." While historians are quite likely to argue that point, the question remains regarding how we've progressed on this "War on Cancer." Since that time, extraordinary progress has been made in understanding the etiology of various cancers and in providing new lines of therapies. The need to maintain efforts regarding this campaign, however, are still very strong.

Today the National Institutes of Health (NIH) estimate that more than 1,500 people die each day from a cancer-related cause in the U.S., accounting for one in four American deaths overall [5]. Perhaps more disturbing, however, is the fact that mortality rates for *most* cancers have not improved significantly over the past three decades [6]. As can be

seen in Figure 1.2, cancer mortality has recently surpassed heart disease mortality rates for individuals under the age of 85, making it the largest killer in the US for that age group [5]. One major component of the progress to date involves advances made through genomic and proteomic studies revealing the presence of serum level molecular targets, or biomarkers, indicative of various cancers and their proliferation [6]. Detection of these biomarkers in circulating blood is one of the clearest paths to achieving early detection. While early detection of any cancer has been identified as likely the best determinant for long-term survival, broadly available diagnostic tools and techniques available for general clinical diagnostics have not yet emerged to significantly take advantage of these discoveries [7, 8].

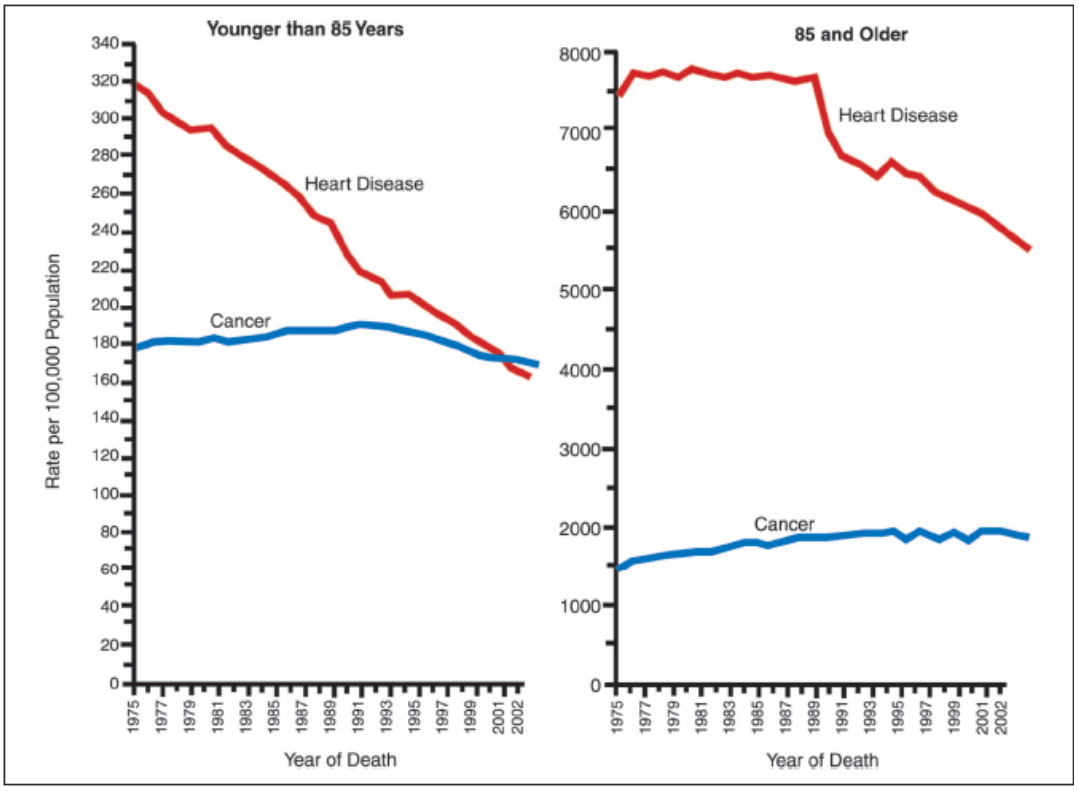

Figure1.2. Death rates from cancer and heart disease, US 1975-2002. [5]

The incidence and mortality rates for the top ten cancers for both men and women in the US are depicted in Figure 1.3. According to the NIH's National Cancer Institute (NCI), death rates decreased for 11 of the 15 most common cancers in men, but actually increased for prostate cancer between 1995 and 2003.[5] As demonstrated in Figure 1.3, it is currently estimated that prostate cancer accounts for a little less than one third of all new cancer cases in the US in men, with more than 218,000 new cases expected from 2007. Figure 1.4 reveals that while mortality rates due to prostate cancer have slowed recently, it still represents the second largest cause of cancer-related deaths in US males.

Figure 1.3. Ten Leading Cancer Types for the Estimated New Cancer Cases and Deaths, by Sex, US, 2007.[5]

A further breakdown of the mortality rates for the top four occurring cancers is depicted in Figure 1.5. These four cancers represent more than half of the diagnosed cancers in the general population and nearly half of all mortality due to cancer. For all but lung cancer, diagnosis in the localized stage of development dramatically improves 5-year and 10-year survival rates towards nearly 100%, as shown in Figure 1.5. It is widely believed that a winning strategy to realizing this goal involves the detection of serum-level biomarkers (those evident in circulating blood) that are currently being discovered for various cancers through genomic and proteomic investigations [6].

The future of cancer diagnostics will therefore likely involve ultra-sensitive screening tools that identify multiple markers indicative of the earliest stages of cancer development. These markers have been difficult to find as they exist in extremely low concentrations in circulating blood. In order to make use of these discoveries at a clinical level, ultra-sensitive biosensors exhibiting high degrees of specificity will be required to

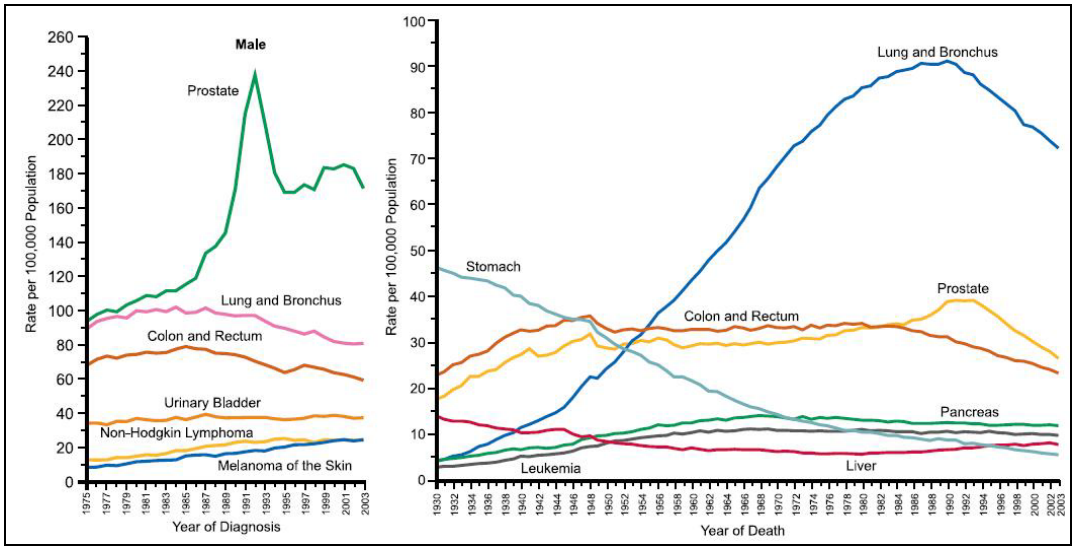

Figure 1.4. Annual-adjust cancer incidence (left) and death (right) rates from the U.S. among males for selected cancers [5].

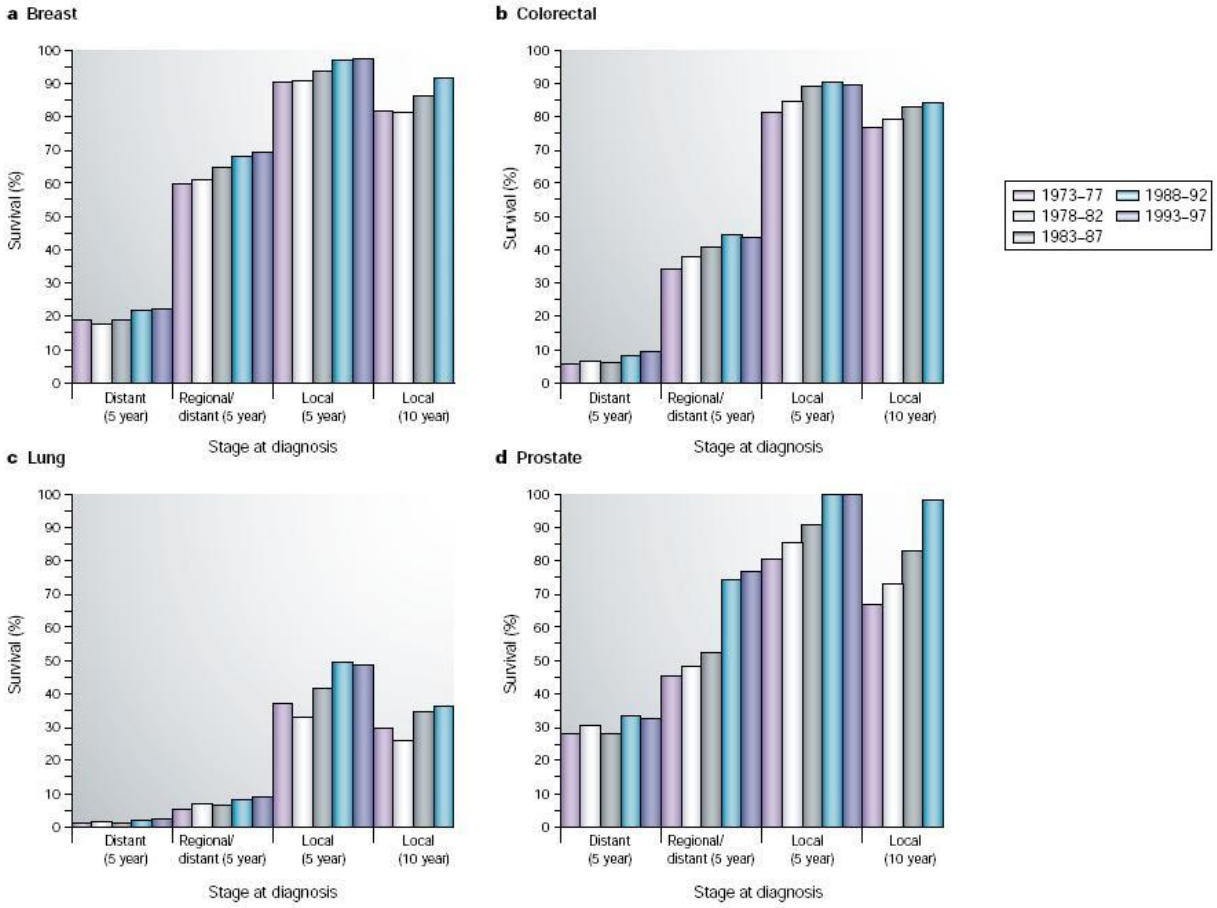

Figure 1.5. Relative survival (5 and 10 year) among selected cancers diagnosed with distant, regional or distant, or localized disease at the time of diagnosis [6].

identify these proteins in clinical samples (such as patient blood plasma or urine). A general review of the cancer literature regarding the use of molecular markers quickly reveals that there is no known single marker sufficient for positive diagnosis of any cancer [9-11]. A sensing technology that identifies a multi-protein signature for diagnosis is most likely to minimize false positives and false negatives [9]. A sensor array incorporating high sensitivity and high specificity could have an impact at multiple levels including early detection screening, post-therapy monitoring, as well as on the proteomic discovery process. This is discussed more thoroughly in Chapter 5.

The goal of this research is therefore to provide a tool for detecting multiple known targets in complex media at the earliest stages of neoplastic growth and proliferation. Prostate cancer represents an excellent test case as the early carcinogenesis and subsequent proliferation of this cancer are among the best understood in all of oncology. It is estimated that 91% of new cases of prostate cancer between 1995 and 2001 were diagnosed at local or regional stages of progression [5]. Not only does this indicate broad clinical understanding of prostate cancer, but it also indicates a wealth of tissue samples available for study at earlier stages of progression.

The most commonly used techniques in clinical laboratories for detecting specific proteins in very low concentration in complex media (such as blood or urine) are immunoassays. One of the most popular is the enzyme linked immunosorbent assay (ELISA or EIA) test. While there are many variants to the ELISA test, conventional ELISA's are considered to have a limit of detection on the order of ~ 1 ng/mL [12]. In its simplest form, conventional ELISA's involve significant preparation and then application of various reagents, each separated by washing steps, then processing with a microplate reader and final analysis. The entire procedure can take anywhere between several hours to a couple of days to perform. Overall, ELISA's are relatively expensive, time consuming and labor intensive processes requiring at least some training and a significant amount of practical experience to perform successfully. Desired improvements on ELISA capability would include label-free detection, near real-time response, greater sensitivity, and capacity for multiplexing. Emerging technologies such as optically-based biosensors [13] or marker-tagged nanoparticles [14] offer excellent alternatives for clinicians, but are currently expensive to produce.

At the outset of this research, the leading technology in label-free detection of protein interactions was surface plasmon resonance (SPR) based devices [15]. While many advancements have been made in the intervening years [13, 16, 17], including improved multiplexing capability, they still suffer from two significant limiting factors. The first is cost. SPR has gained broad use by clinical researchers of late, generating a significant commercial market for these sensors [16]. Significantly, however, the cost of a single SPR sensor is approximately $160 (Biacore's CM5 SPR sensor chip available through GE Healhcare), even in this more developed market. Note, this cost is simply for the transducer component of the overall sensor, and still requires both the monitoring electronic system and the application of appropriate capture agents. For multiple sensors used in a multiplexed system, the commensurate price rises rapidly. Furthermore, there is a limitation on how many channels can be introduced for multiplexed operation, based on the monitoring system being used. It is not feasible that these sensors could be utilized by the broader public for routine testing of multiple targets on a massive scale. The second limiting factor of the SPR system is that the sensitivity range is narrow and fixed by the precision of the detection mechanism.

The sensors I have proposed take advantage of advances made in the microelectronics industry allowing for fabrication of piezoelectric resonator-based sensors in an array package to provide multiplexed sensors at a much lower cost. A microelectronic mass-production facility could quite easily produce these sensor arrays and significantly take advantage of economies of scale and drive down the price as the market size increased. Another advantage of this approach comes from the fact that the detection limit of acoustic sensors is a function of their resonant frequency, which can be controlled by

physical parameters of the resonator. As fabrication technology and capabilities continue to improve, the detection capabilities of these sensors should improve correspondingly.

The specific aims of this thesis research are therefore as follows:

1. To develop a bulk acoustic resonator device appropriate for application as a highly sensitive biosensor.
2. To develop an appropriate biosensor preparation procedure by immobilization of appropriate capture agents.
3. Demonstrate the functionality of these biosensors towards known cancer biomarkers.

CHAPTER 2

BACKGROUND & SIGNIFICANCE

To make clear what I am attempting to do, it is necessary to clearly explain the principles that I will be employing towards developing the proposed sensor and also describe how this work fits into the broader body of research regarding biosensor design and development. First, I will describe the principles of acoustic-based sensors, as opposed to electrochemical or optical transduction devices. As part of this discussion, I will include a discussion of how my work fits within the field of acoustic sensor device technology. Second, I will describe how acoustic wave devices can be employed toward biosensor applications and the potential advantages of using such a platform over alternative label-free detection methods. Finally, I will argue for importance of multiplexing and the development of a biomarker micro-array.

Principles of acoustic resonators

Acoustic wave resonators function by the excitation of the piezoelectric class of crystals due to an alternating electric field. That is to say, piezoelectric crystals have the capacity to launch and support a mechanical acoustic wave as the result of transducing energy from an excitatory RF electric field [18]. All crystals are classified into one of seven categories, based on their degrees of symmetry. The seven systems are in turn sub-divided into point groups, or classes, according to their symmetry with respect to a point. This yields thirty-two classes of crystal in total. Twenty-one of the thirty-two existing

crystal classes exhibit a lack of centro-symmetry, or an inversion asymmetry. Of these twenty-one, all but one exhibit non-zero piezoelectric constants [19]. This piezoelectric crystal family of twenty is characterized by this inversion center, which form electrically neutral dipoles in their natural state. The crystal of interest for this research is zinc oxide (ZnO), which is a hexagonal *6mm* class crystal, and belongs to this piezoelectric family.

When an external stress is applied to a piezoelectric crystal, the symmetry is disturbed causing a charge asymmetry, resulting in an electric displacement across the material. This is the direct piezoelectric effect. The inverse piezoelectric effect, as the name implies, describes the strain of the material under an electric field due to the realignment of unit crystal dipoles in response to that field. Thus, an acoustic wave can be launched through the bulk of the material by exposing the crystals to an oscillating electric field. By matching the oscillation of the electric field to the physical parameters of the crystal that bounds the mechano-acoustic wave, a resonance condition is achieved in which the maximum amount of energy is being transduced into mechanical energy due to the favorable conditions.

The fundamental equations that describe the relationship between the electric dipole and external forces is described by the following constitutive relations:

$$\overline{T} = \overline{\overline{c}} : \overline{S} - \overline{\overline{e}} : \overline{E} \tag{2.1}$$

$$\overline{D} = \overline{\overline{\varepsilon}} : \overline{E} + \overline{\overline{e}} : \overline{S} \tag{2.2}$$

Note that equation (2.1) is an extension of Hooke's law in three dimensions, where T is stress, S is strain, c is the stiffness tensor. The second term in (2.1) represents the effect of piezoelectric stiffening under an electric field where E is the electric field and e is the

piezoelectric coupling tensor. Equation (2.2) is Maxwell's definition for electric displacement, D, where ε is the permittivity tensor of the material and E is again the apparent electric field. Equation (2.2) is modified by the inverse piezoelectric strain component of the electric displacement formed by the product of the piezoelectric tensor, e, and the external strain, S. A more extensive treatment of the generation and propagation of acoustic waves in crystals can be found in Rosenbaum [20].

Propagation of an acoustic wave in a solid can take several forms, or modes. In general, these waves can be either longitudinal (particle displacement in parallel with the propagation direction), shear (particle displacement perpendicular to the wave propagation direction) or a combination of the two. For the purpose of developing a biosensor application, any resonator device used must employ an acoustic mode that exhibits particle displacement parallel to the surface of the device. This is necessary as any particle displacement not parallel to the surface would be readily absorbed by either the viscoelastic surface coating comprising the capture molecules necessary to functionalize the sensor, or by the liquid test media itself as compression waves.

Acoustic wave devices are broadly categorized by those that travel within the crystal bulk, known as bulk acoustic waves (BAW), or those that travel along the crystal surface, known as surface acoustic waves (SAW). This research will not investigate the shear-horizontal surface acoustic wave (SH-SAW) family of devices which have been applied in numerous studies towards sensing in a liquid phase environment [21-24]. The sensitivity of shear-mode resonator-based biosensors has been characterized by many, including Sauerbrey [25], Kanazawa [26, 27], and more recently Hunt [28], (and will be

discussed in greater detail later in this chapter) but all agree that the sensitivity of these devices is proportional to a power of the fundamental resonant frequency, f_o.

The resonance frequency of a SAW device is controlled by a surface parameter of the electrode fabrication. SAW devices are created by depositing an electrode configuration called 'interdigitated trandsducers' (IDTs) onto the surface of an appropriately aligned polished crystal surface, as seen in Figure 2.1. The smaller the distance between "fingers" of the IDT exciting the surface acoustic wave, the higher the resonant frequency, as the transducer spacing defines the wavelength of the acoustic wave.

For bulk acoustic devices, the resonant frequency is a function of the thickness of the film. Piezoelectric crystal films can be deposited with extremely small thicknesses through a variety of liquid and vapor film deposition techniques [29]. In order to achieve ultra-high frequencies (e.g. GHz) of operation in a SAW device, extremely high resolution photolithography equipment is required, which is neither cheap nor widely

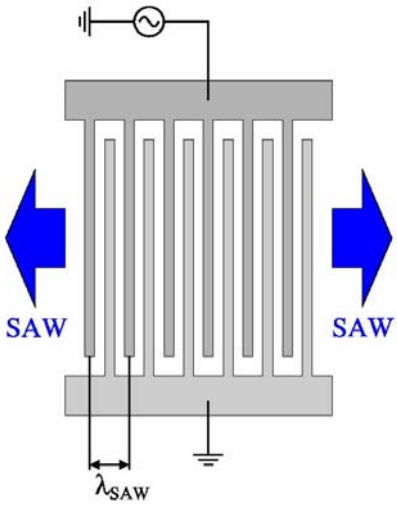

Figure 2.1. IDT electrode configuration commonly employed for fabrication of a SAW transducer. [Taken from www.sp.phy.cam.ac.uk]

available. For this reason, it is much simpler to achieve higher fundamental resonant frequencies in BAW devices than in SAW devices. For this reason, this research will focus on a BAW design.

Resonator Design

Piezoelectric ZnO thin films have most often been used in the past as high frequency filters for a multitude of telecommunications applications [30, 31]. Typically these devices are operated in the thickness-excited (TE) longitudinal mode in which the frequency can be tuned simply by varying the thickness of the ZnO thin film. Methods of excitation will be discussed in greater detail later in this chapter. When operated with an adjacent liquid medium, the longitudinal mode energy is dissipated, as described earlier, into the liquid as compression waves for devices utilizing waves that propagate at a velocity higher than the sound velocity in the liquid. This results in a highly reduced quality factor, Q, and poor mass resolution in a sensor application. Q is a common parameter used to characterize the strength of a resonator. Resonator Q is broadly defined as:

$$Q = \frac{2\pi \cdot \text{Energy Conserved per cycle}}{\text{Energy Dissipated per cycle}}$$

There exist many methods of estimating Q, which receives discussion by Rosenbaum [20]. As previously mentioned, acoustic waves can travel in a variety of modes. The thickness shear mode (TSM) is better suited for liquid sensing applications due to the shear particle displacement of the acoustic wave in the piezoelectric film. Since the

adjacent liquid medium cannot effectively support a shear wave, very little energy is transferred into the liquid resulting in minimal damping of the acoustic wave.

The term 'TSM resonator' is often used interchangeably with quartz crystal microbalance (QCM). That is because the QCM is by far the most widely used resonator in commercial applications that operates in the TSM mode. QCMs are fabricated by taking thin slices at the appropriate angle from a single crystal bulk, as shown in Figure 2.2. Application of TSM resonators in biosensor applications are described in greater depth later in this chapter.

The sensitivity of acoustic waves in AT-cut quartz plates has been widely exploited with QCMs as gravimetric sensors in both vapor phase and in liquid phase sensing [32-35] which uses TE to excite the wave. It has been shown, however, that lateral field excitation (LFE) can also be used to excite the TSM wave in QCMs [36-39] and that the resulting device may be more sensitive to surface perturbations than the standard TE QCM for liquid-phase sensing applications [40-42]. The LFE configuration is demonstrated in Figure 2.3 below, in comparison to the TE configuration. The

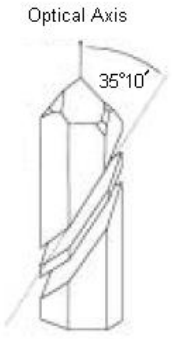

Figure 2.2. A quartz plate is cut at an angle of 35˚10' with respect to the optical axis to form AT-cut quartz suitable for QCM applications. A deviation of only 5' from this angle leads to a significant change in the temperature coefficient.[43]

advantages of LFE over TE liquid-phase applications are mainly attributed to the fact that in LFE, the electrodes that generate the electric field are not directly in the path of the acoustic wave, as in TE. Since the metal material that forms the electrode is a source of acoustic wave scattering and damping, its removal from the acoustic path results in higher *Q* values. Other advantages include increased stability at a given harmonic, and reduced aging of the crystal since the electrode is absent from the area of greatest vibrational motion [44]. For biosensor applications, removing the electrode from the acoustic path also means that biological molecules can be immobilized directly onto the region of highest particle displacement which should result in greater sensitivity of the sensor.

There are numerous disadvantages to using QCMs as biosensors, however. QCMs typically operate in the frequency range between 5-35 MHz. In AT-cut quartz plates, it is difficult to further increase the fundamental operating frequency because of its

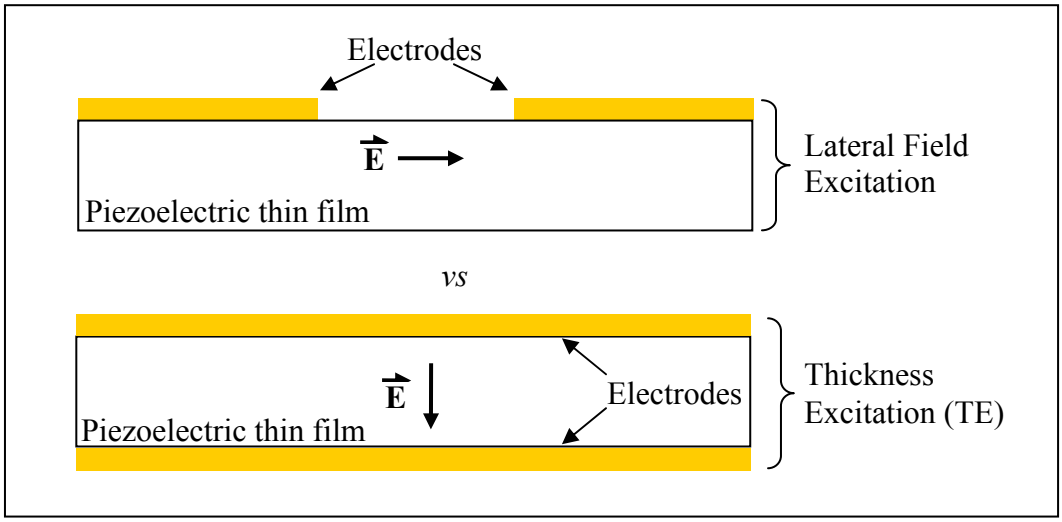

Figure 2.3. Lateral field excitation resonator configuration as compared with the more common thickness excitation configuration.

dependence on the thickness of the quartz plate. At very low thicknesses, the quartz plate becomes extremely fragile and is too difficult to handle. It is possible to achieve higher frequencies with the QCM by monitoring harmonic modes beyond the fundamental, but these become progressively diminished with increasing harmonic number [45, 46].

It is therefore necessary to develop a TSM resonator that can be easily fabricated in a robust design that can achieve higher frequencies of operation than the QCM. The first aim of this research is therefore to develop a thin film ZnO bulk resonator operating a TSM, which requires two fundamental criteria to be met. First is excitation of the TSM itself. One method of achieving this is LFE of *c*-axis oriented ZnO and involves an electrode configuration similar to the one seen in Figure 2.3. LFE of ZnO will be discussed in greater detail in Chapter 3. Second, a resonator requires that the acoustic wave be maintained in the crystal. A fundamental rule of mechanics is that acoustic energy has a preference to propagate through a denser media, with particles free to move and carry the wave. For that reason, it is often asserted that acoustic waves prefer to travel in media with a slower acoustic velocity. The acoustic velocity of a crystal film is described by

$$v_a = \sqrt{c_n / \rho_n} \tag{2.3}$$

where ρ_n is the film density and c_n is the appropriate stiffness parameter. A second fundamental rule is that high acoustic impedance mismatches between adjacent media encourage a high reflection response of an incident acoustic wave. Acoustic impedance can be described by [47]

$$Z_n = \sqrt{c_n \rho_n} \tag{2.4}$$

As air has very low stiffness and density compared to piezoelectric crystals, its effective acoustic impedance is zero. That is why a common technique for fabricating thin film bulk acoustic resonators (FBARs) requires the etching of an air barrier beneath the piezoelectric film. In this configuration, the vast majority of acoustic energy is reflected at each surface and remains within the piezoelectric crystal film.

This etching step is both difficult to achieve and requires an additional and expensive fabrication step. Furthermore, the films of ZnO necessary to produce the very high frequencies desirable for higher orders of sensitivity would cause these devices to be extremely delicate. The solution to this problem is to deposit the piezoelectric film onto a solid structure that mimics the acoustic impedance of air, which is referred to as a solidly mounted resonator (SMR). Newell first described the concept of SMRs in 1965 [48], in which an acoustic mirror (analogous to an optical Bragg reflector) is deposited beneath the piezoelectric crystal film, as shown in Figure 2.4. I employ this configuration in order to develop a design that is both robust and easy to fabricate.

Excitation of shear mode bulk waves in thin film ZnO have been reported as early as 1974 [49]. More recent success has been reported by Krishnaswamy, *et al.*, who attempted the growth of inclined *c*-axis oriented films coupled with an electrode pattern in which the electrodes are situated on opposing surfaces of the thin film to produce an electric field through the thickness [50]. The incline of the ZnO axis would thereby allow for excitation of the crystal orthogonal to the *c*-axis and stimulate a shear mode acoustic

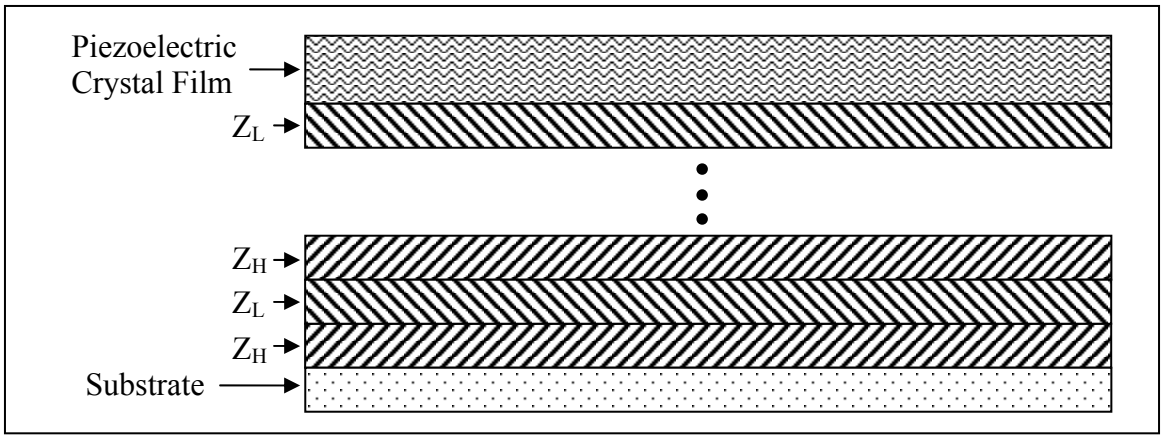

Figure 2.4. The solidly mounted resonator configuration (SMR) consisting of alternating layers of ¼-λ low and high acoustic impedance films.

wave. Wang and Lakin took a similar approach and had excellent success in fabricating oriented films with the *c*-axis of the hexagonal crystal oriented 40° to the substrate normal [51]. While their resonator quality factor, Q, and electro-mechanical coupling, K^2, were high, the operating frequency attempted was low (~293 MHz) and the fabrication procedure required bulk etching of the Si wafer to produce air-backed ZnO membrane resonators. More recently, Link *et al.* have revived the inclined ZnO growth research with the intent of developing ZnO TSM resonators for liquid phase sensing [52, 53]. Their device design is demonstrated in Figure 2.5. A shortcoming of the inclined ZnO growth method, in general, is that the thickness excitation requires that the electrodes be in the path of the acoustic wave. While it offers the benefit of a higher operating frequency than the QCM for sensing, it still suffers from the same pitfalls as the QCM because the electrodes are located in the area of highest sensitivity.

In a study by Woo Wai *et al.* focusing on non-inclined *c*-axis oriented ZnO, the TSM was excited through LFE [54]. The devices were fabricated through the use of a self-

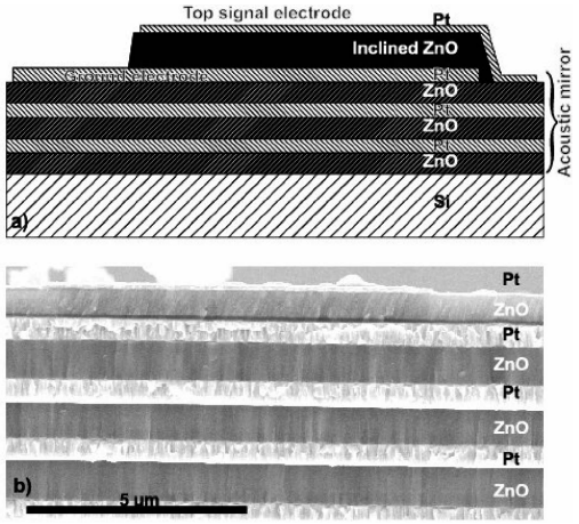

Figure 2.5. a) Schematic cross section and b) scanning electron microscopy of solidly mounted resonators. The upper ZnO film is *c*-axis inclined [53].

aligning process that involved ZnO liftoff and a spiral electrode structure spanning 2 mm in diameter. Operating close to 4.1 GHz, the devices illustrated the ability for ZnO FBARs to be operated at high frequencies with relative ease. An acoustic mirror was not implemented in the design, however, and the resonator Q was very low (roughly 35).

Acoustic velocity calculations made from the numbers given in the study yield ~3,280 m/s. Given that the acoustic velocity, v_a, of a resonator is defined by Equation (2.3), a theoretical estimation of ~2,841 m/s is calculated using single-crystal bulk stiffness properties of ZnO available in Auld [55]. This value is reasonable considering the polycrystalline variations in depositions of thin film ZnO.

Acoustic Biosensors

Acoustic resonators were first recognized as an appropriate platform for highly sensitive sensors in the 1950's. The mechanism for detection relies on the stable resonance of an acoustic wave in a fixed space. The physics of an acoustic wave propagating through a crystal, oscillating between opposing boundaries, is well understood and has been thoroughly characterized by Auld [55]. For sensor applications of acoustic resonators, the acoustic wave acts as a probe that indirectly queries the surfaces for changes in the boundary conditions. Perturbations of those boundary conditions results in a measurable frequency shift.

Sauerbrey was the first to observe that the resonance condition of a piezoelectric resonator was impacted by the loading of one surface. He worked to characterize the sensitivity of acoustic sensors using the QCM as part of his dissertation research in the late 1950's. One publication in particular is often cited in the literature in regard to acoustic sensors, in which Sauerbrey observes that the resonant frequency of the QCM shifts in accordance with the following [25]:

$$\Delta f = \frac{-2 f_o^2 \Delta m}{A\sqrt{\rho_q \mu_q}} \tag{2.5}$$

where f_o is the unloaded resonant frequency of the sensor, A is the acoustically active surface area, ρ_q is the crystal density, μ_q is the crystal stiffness, and m is the mass loading at the surface of the crystal. As can be seen from Equation (2.5), the shift in resonant frequency of the sensor is proportional to the change in mass at the surface boundary via

a coefficient scaled by the square of the unloaded resonance frequency. The higher f_o, the more sensitive the resonator is to a corresponding mass loading at the surface.

The derivation of this equation requires assumptions that are not valid, however, for operation in a liquid environment or for loading of biological materials at the surface. One assumption, for example, is that the loaded mass must be a rigid film. As noted earlier, the acoustic waves have a propensity to travel in materials of higher acoustic impedance. For the case of a liquid film, there exists a decay length in which the shear acoustic wave propagates into the liquid film. This decay length, δ, is defined as

$$\delta = \sqrt{2\eta_L / \omega\rho_L} \tag{2.6}$$

where η_L is the viscosity of the liquid, and ρ_L the liquid density. For the case of a 5 MHz QCM resonator, the acoustic wave would travel 250 nm into water.

Kanazawa and Gordon were the first to address an appropriate description for acoustic resonators operating in a liquid, deriving the following relationship [26]:

$$\Delta f = -f_o^{3/2} \sqrt{\frac{\eta_L \rho_L}{\pi \rho_q \mu_q}} \tag{2.7}$$

William Hunt, alternatively, approaches the entire relationship afresh, seeking "to go beyond the static Sauerbrey equation to a more dynamic equation" to more precisely define the change in boundary conditions as a description of the molecular recognition event [28]. Beginning with the complex reciprocity relation described by Auld [55], Hunt employs time-dependent perturbation theory to derive the following relation for frequency shifts experienced by the QCM in a biosensor application:

$$t\frac{\partial \Delta\omega}{\partial t}+\Delta\omega=\frac{\omega_u h_f}{\pi\sqrt{\rho_q\mu_q}}\left\{-\omega_u\left[\Delta\rho-\frac{\Delta\mu}{V_S^2}\right]+i\cdot\left[\frac{\Delta\rho}{\partial t}-\frac{1}{V_S^2}\cdot\frac{\Delta\mu}{\partial t}\right]\right\} \tag{2.8}$$

where ω_u is the unperturbed frequency (in radians), t is time, h_f is the height of the film, $\Delta\rho$ and $\Delta\mu$ are the density and stiffness of the film, and V_S represents the acoustic shear wave velocity. If $\Delta\rho$ and $\Delta\mu$ were known, it would then be possible to solve (2.8) using the integrating factor method, which would yield:

$$\Delta\omega=\frac{1}{t}\left(\int^t\frac{\omega_u h_f}{\pi\sqrt{\rho_q\mu_q}}\left\{-\omega_u\left[\Delta\rho(\tau)-\frac{\Delta\mu(\tau)}{V_S^2}\right]\right\}d\tau+i\cdot\left[\Delta\rho(t)-\frac{\Delta\mu(t)}{V_S^2}\right]+C\right) \tag{2.9}$$

It must be noted that Hunt assumes a stress-free boundary in which no acoustic energy transfers into the adjacent liquid/air space beyond the biofilm. That is to say, $T\cdot\hat{n}=0$. He acknowledges that this is not accurate, of course, but the assumption is required to simplify the derivation. Proceeding with this assumption and assuming that ω, ρ and μ do not vary with time, Equation (2.8) becomes

$$\Delta f=\frac{-2f_o^2 h_f}{\sqrt{\rho_q\mu_q}}\left[\Delta\rho-\frac{\Delta\mu}{V_S^2}\right]. \tag{2.10}$$

Note that Equation (2.10) has a striking similarity to the Sauerbrey Equation (2.5) with the exception that the frequency shift is now a function of both a change of mass loading at the surface as well as a change in the mechanical stiffness of the film. This has significance when the film consists of biological molecules that are known to undergo a conformational change upon binding a target. This provides both the opportunity that

TSM resonators could have an enhanced detection capability and the cautionary note towards interpreting the meaning of collected data.

The work of Sauerbrey established the potential for acoustic wave devices as a viable sensor platform. QCMs became widely used because they demonstrated exceptional conservation of energy as a resonator, characterized by Q values of up to 70,000 and excellent frequency stability between 0-50˚C [47]. Breakthroughs in oscillator technology allowed Nomura and Okuhara in 1982 to demonstrate that these sensors could be employed in a bioanalytic capacity by operating them in liquids [56]. Since then, they have been employed quite extensively as biosensors [47], with several commercial QCM systems available today [45]. As mentioned earlier, QCMs are limited by the fact that films thin enough to reach the GHz range of operation are far too fragile to handle if cut from a single-crystal bulk and cannot be deposited onto a support substrate with the crystal texture required.

Sensor Arrays

As mentioned earlier, it is generally agreed that there is little chance that a single biomarker will be able to provide definitive evidence of cancer proliferation [57]. One of the most successful and widely used marker screening tests involves the diagnosis of prostate cancer (PCa) by measuring the serum concentration of prostate specific antigen (PSA) in conjunction with a digital rectal exam, describing an examination performed with the examiner's finger. There exists significant controversy over the use of PSA testing as a means of diagnosing PCa, predominantly due to the high false positive rate

[58-62]. Extensive long-term studies (including such studies as the Prostate, Lung, Colorectal and Ovarian Screening Trial ff to be completed in 2015) begun in the 1990s have yet to provide conclusive evidence of the efficacy of the PSA screening test for those under 75. For individuals over 75, however, the US Preventive Services Task Force has already issued a recommendation against the regular practice of PSA screening. Given the average lifespan of males and taking into consideration the generally slow progression rate of PCa, this recommendation was made because the cancer itself tends to not have a significant impact on these individuals overall survival or quality of life. Taken together with high false positive rate of the PSA test itself, the negative psychological impacts of a positive diagnosis, and the trauma associated with available treatments, the negative impacts are considered to outweigh the benefits of screening [63]. This recommendation has understandably been met with some contention from clinicians, and as a result is likely to be considered as a suggestion rather than as a rule, by most. Obviously, a more definitive screening mechanism is required in general, that will allow for the quantification of multiple molecular targets.

It is further desirable to minimize false negatives and false positives. Sensor arrays allow for implementing redundancy in the system by preparing multiple sensors in the same array for the same target and thereby delivering enough data to employ statistical analysis of the results. For this reason, sensor arrays that can test for multiple targets simultaneously offer the most useful tool for an early detection system for cancer. A cursory search of the literature quickly reveals that many researchers are already pursuing sensor array systems rather than single sensor systems [31, 48, 55-63]. These array

systems often include, however, delicate designs that are difficult and expensive to fabricate.

A recognition of the importance of this approach is exemplified by one of the primary initiatives of the NCI's Early Detection Cancer Network (EDRN), whose mission is "to make molecular diagnostics a reality [allowing for] individualized treatment for cancer patients." The initiative of interest is the identification of proteomic technologies that allow for rapid identification of cancer proliferation *signatures*. That is to say, the proliferation of a particular cancer is revealed by the quantification of multiple targets in a patient's sample. Their efforts have converged upon various protein and nucleic acid microarray technologies that allow for rapid screening and subsequent validation of new circulating biomarkers. Some of the technologies highlighted in their latest annual report include the LUMINEX Corporation's xMAP system and the nucleic acid programmable protein array (NAPPA) system from Harvard Medical School [64].

Acoustic biosensor research in the past has largely focused on the application of QCM devices [65, 66]. As is the case for most biosensors, these sensors are comprised of two fundamental components (described in Figure 1.1). The first being the base transducer device, or resonator, that excites and maintains a resonating acoustic wave in the piezoelectric crystal. The second component is the immobilization of appropriate capture agents at the surface of the crystal, thereby functionalizing the resonator as a biosensor. When a target molecules from the test medium interact or bind with the capture molecules, the boundary conditions are altered which in turn changes the resonance conditions for the acoustic wave. This is measured as a resonant frequency shift.

Theoretically, the sensitivity of an acoustic biosensor is directly related to the value of that resonant frequency, as discussed previously in this chapter. While QCM technology offers excellent detection capabilities, it is limited in several ways with respect to biosensor applications. The most significant limitations include the relatively low frequency of operation, as mentioned in Chapter 2, but also the relative difficulty in multiplexing the sensors due to their large size. Cost is also a drawback to QCM technology as the sensors are comprised of quartz plates which can be expensive to manufacture to the required specifications. SAW devices have provided several advantages in addressing many of the aforementioned criteria [65, 66], but mass fabrication tools still limit commercially available SAW devices to the sub-gigahertz (GHz) range of operation.

This research proposes an acoustic-based solution that meets all of the requirements proposed by Erickson, *et al* [57]. In summary, those requirements include sensitivity and specificity, multiplexing capability, and a reduction in measurement complexity and cost. The simple design is compatible with existing microelectronic fabrication processes that allow for cost-effective mass production, and has a very small footprint (< 5 mm^2). As mentioned earlier, with moderate spatial arrangement, one could easily fit as many as 1,000 arrays, each consisting of eight devices, onto a single 3-inch wafer. The design will also allow for expandable array configurations. The sensing mechanism involved is entirely electronic and occurs as the capture molecules bind their target. The sensors thereby provide a means of label-free, near real-time reporting with minimal electronic hardware.

CHAPTER 3

RESONATOR DESIGN & IMPLEMENTATION

The development of a novel microelectronic resonator requires two fundamental problems be solved. Primary is the identification of an appropriate material with the proper crystal orientation that will support the acoustic mode of interest. As identified in the previous chapter, the TSM is the mode of interest for the purpose of biosensor application. Further, a robust and low-cost design is desired, which will be achieved by pursuing a solidly mounted ZnO resonator configuration. This encompasses the second problem, which is the development of an appropriate acoustic mirror to reflect the acoustic energy back into the piezoelectric crystal. I will begin this chapter with a theoretical confirmation that *c*-axis oriented ZnO can support the desired TSM wave. I will then discuss the chosen resonator package design and derive a theoretical model for the desired acoustic mirror and subsequent implementation of the solidly mounted TSM thin film ZnO resonator. Finally, I will discuss efforts to improve the device design for the purpose of biosensor applications.

Thickness Shear Mode in ZnO

Propagation of an acoustic wave via piezoelectric excitation in a crystal bulk is described by the Christoffel equation:

$$k^2 \Gamma_{ij} v_j = \rho \omega^2 v_i \tag{3.1}$$

where k is the wave number defined as ω / v_a (or frequency/acoustic velocity), ρ is the density of the material, v_i and v_j are the particle polarization direction vectors, and Γ_{ij} is the piezoelectrically stiffened Christoffel matrix. Γ_{ij} is defined as,

$$\Gamma_{ij} = l_{iK}\left(c_{KL}^{E} + \frac{\left(e_{Kj}E_j\right)\left(E_i e_{iL}\right)}{E_i \varepsilon_{ij}^{S} E_j} \right) l_{Ij} \tag{3.2}$$

where E_n is the three dimensional electric field vector and the l_{iK} matrix describes the divergence of the acoustic wave propagation, taking the following form:

$$l_{iK} = \begin{bmatrix} l_x & 0 & 0 & 0 & l_z & l_y \\ 0 & l_y & 0 & l_z & 0 & l_x \\ 0 & 0 & l_z & l_y & l_x & 0 \end{bmatrix} . \tag{3.3}$$

In (3.3), the nonzero terms come from the propagation vector

$$\hat{\mathbf{l}} = l_x \hat{\mathbf{i}} + l_y \hat{\mathbf{j}} + l_z \hat{\mathbf{k}} . \tag{3.4}$$

The l_{Ij} matrix is simply the transpose of l_{iK}, and c_{KL}^{E} is the material stiffness tensor at a constant electric field rotated by the appropriate Euler angles. As mentioned above, the crystal orientation was confirmed by X-ray diffraction to be a highly *c*-axis aligned *6mm* hexagonal ZnO crystal, so no Euler angle rotations need be applied. Further assuming wave propagation in the direction of the thickness of the film and also aligned with the substrate surface normal, the terms l_x and l_y go to zero and l_z can be assumed to be unity.

In order to generate a TSM wave in normally aligned *c*-axis oriented ZnO, it is necessary to use LFE of the ZnO bulk. As demonstrated in Figure 2.3, LFE involves co-planar electrodes generating an electric field parallel to the film surface, or laterally.

Given that the electric field has been maximized in the *x*-*y* plane, it can be assumed that E_z goes to zero (i.e. the electric field in the *z* direction) and the electric field parameters can be described as $E_x^2 + E_y^2 = 1$.

The standard stiffness tensor for the *6mm* class of hexagonal crystals is defined as

$$c = \begin{bmatrix} c_{11} & c_{12} & c_{13} & 0 & 0 & 0 \\ c_{12} & c_{11} & c_{13} & 0 & 0 & 0 \\ c_{13} & c_{13} & c_{33} & 0 & 0 & 0 \\ 0 & 0 & 0 & c_{44} & 0 & 0 \\ 0 & 0 & 0 & 0 & c_{44} & 0 \\ 0 & 0 & 0 & 0 & 0 & c_{66} \end{bmatrix} \tag{3.5}$$

where the subscripts exhibit the abbreviated Einstein summation notation [20] that allows the true 9 x 9 stiffness tensor to be reduced via symmetry to the 6 x 6 in (3.5). The corresponding piezoelectric coupling tensor takes the form

$$e = \begin{bmatrix} 0 & 0 & 0 & 0 & e_{15} & 0 \\ 0 & 0 & 0 & e_{15} & 0 & 0 \\ e_{31} & e_{31} & e_{33} & 0 & 0 & 0 \end{bmatrix}. \tag{3.6}$$

By defining the electric field *E* as

$$E_j = \begin{bmatrix} E_x \\ E_y \\ 0 \end{bmatrix} = E_i^T, \tag{3.7}$$

it is now possible to solve for (3.2) symbolically, yielding the following solution to the Christoffel matrix:

$$\Gamma_{ij} = \begin{bmatrix} c_{44} + \dfrac{e_{15} E_x^2}{\varepsilon_{11}} & \dfrac{e_{15}^2 E_x E_y}{\varepsilon_{11}} & 0 \\ \dfrac{e_{15}^2 E_x E_y}{\varepsilon_{11}} & c_{44} + \dfrac{e_{15} E_y^2}{\varepsilon_{11}} & 0 \\ 0 & 0 & c_{33} \end{bmatrix}. \tag{3.8}$$

Substituting (3.8) into (3.1), we find that the Christoffel equation is a simple eigenvalue problem, where the corresponding eigenvalues and respective eigenvectors solutions are

$$x_1 = \begin{bmatrix} -E_y \\ E_x \\ 0 \end{bmatrix}, \lambda_1 = c_{44} \ , \ x_2 = \begin{bmatrix} E_x \\ E_y \\ 0 \end{bmatrix}, \lambda_2 = c_{44} + \frac{e_{15}^2}{\varepsilon_{11}} \ , \ x_3 = \begin{bmatrix} 0 \\ 0 \\ 0 \end{bmatrix}, \lambda_3 = c_{33} \ . \tag{3.9}$$

Each of the three solutions, x_n, describes the particle displacement associated with an acoustic wave mode. The associated eigenvalues describe that mode's acoustic velocity, v_a, and direction. As can be seen, the only term that exhibits piezoelectric stiffening is the x_2 term, which indicates particle direction only in the x-y plane. The associated eigenvector, λ_2, describes shear wave propagation due to piezoelectric transduction in the z-direction through the c_{44} term. The acoustic velocity of this wave can thus be described by

$$v_a = \sqrt{\frac{c_{44} + \dfrac{e_{15}^2}{\varepsilon_{11}}}{\rho}} \ . \tag{3.10}$$

ZnO single-crystal bulk values taken from Auld [55] can be used for the terms in (3.10) in order to determine a theoretical velocity. This yields a shear wave velocity traveling in the thickness direction of 2,841 m/s in hexagonal *6mm* ZnO. It is important to stress that this value is ideal based on bulk single crystal values. Most ZnO thin films,

including the films used for this research, are both polycrystalline and involve dopants that mitigate the conductive properties of pure ZnO. For these reasons, it is reasonable to assume that shear values will vary from the ideal velocity calculated above. Indeed, other investigators that have demonstrated TSM ZnO resonators have empirically determined values of 3,280 m/s [19], and 3,370 m/s [54]. It is worth noting that applying the appropriate stiffness values from Auld, a longitudinal wave traveling in the thickness direction should travel at 6,100 m/s, by comparison. This has been verified by numerous implementations of longitudinal wave FBAR devices [67-69], as well as those achieved in the very same lab in which this thesis research was accomplished [70, 71].

Thus I have demonstrated that the TSM is possible in *c*-axis oriented ZnO. It remains, therefore, to determine a device design that allows for growth of *c*-axis oriented ZnO films in a configuration that is both a robust and low cost implementation.

Solidly Mounted Resonator

Traditionally, FBARs are fabricated by etching the support layer upon which the piezoelectric film was deposited in order to create an air boundary on both the top and bottom of the piezoelectric film. Recall from Chapter 2 that acoustic energy prefers to travel in a medium where it travels slower, which is characterized by the mode acoustic velocity. More critical, however, is the magnitude of the impedance mismatch regarding the medium on either side of a boundary. As for electromagnetic waves, if the perceived acoustic impedance across a boundary is matched, the wave would pass through the boundary with practically no reflection. If a substantial impedance difference is

perceived, however, then a substantial amount of the acoustic energy would be reflected. Theoretical estimation of the characteristic acoustic impedance of a material, Z_a, is often determined using the relation described in Equation (2.4). Using bulk properties for ZnO given by Auld [55], one can estimate the shear mode acoustic impedance of ZnO to be 15.53 kg/m^{2}s. Given the extremely low density and stiffness properties of air, one can reasonably assume that air has an effective acoustic impedance of zero. As described in Chapter 2, this low impedance boundary is necessary for containing the acoustic energy within the piezoelectric film. As I also explained in Chapter 2, the etching process required to accomplish this configuration is both often difficult to achieve (especially when ZnO is the piezoelectric film of interest) and does not accommodate the goal of producing a simple and cheap fabrication process.

For this reason, a solidly mounted resonator (SMR) configuration was chosen, as described in Figure 3.1. The SMR configuration was introduced by Newell [48], in which he describes the fabrication of an acoustic mirror below the piezoelectric film. The theory behind this configuration is similar to that of a Bragg reflector for reflecting optical waves, in which alternating materials of high and low impedance at ¼-wavelength thickness can mimic a zero acoustic impedance boundary at the piezoelectric layer.

The theory has been modeled by several using transmission line theory [72-74]. Ballato presents a networked transmission line model for piezoelectric acoustic wave excitation and propagation employing networked electromagnetic models of electro-elastic activity as perfect analogs of mechano-acoustic activity, both within the bulk at any point and also at the boundaries. According to Ballato, appropriate analogs from the electrical input impedance of multiple transmission lines in series (representing multiple

material films adjacently layered on top of each other) are identical to the effective acoustic impedance of the overall structure and substrate. Ballato's electric circuit model is actually designed to model the coupling of electrical inputs to mechanical wave propagation through a piezoelectric bulk via transformers, but is entirely appropriate for modeling the propagation of mechanical waves in the non-piezoelectric films that make up the acoustic mirror. This model can be represented as the one shown in Figure 3.1.b. Ballato's model will be revisited later when discussing the resonator design.

From transmission line theory, we know that the characteristic electrical input impedance, Z_{in}, at a junction is given by [75]

$$Z_{in} = Z_o\left(\frac{Z_L + jZ_o\tan(kl)}{Z_o - jZ_L\tan(kl)}\right) \tag{3.11}$$

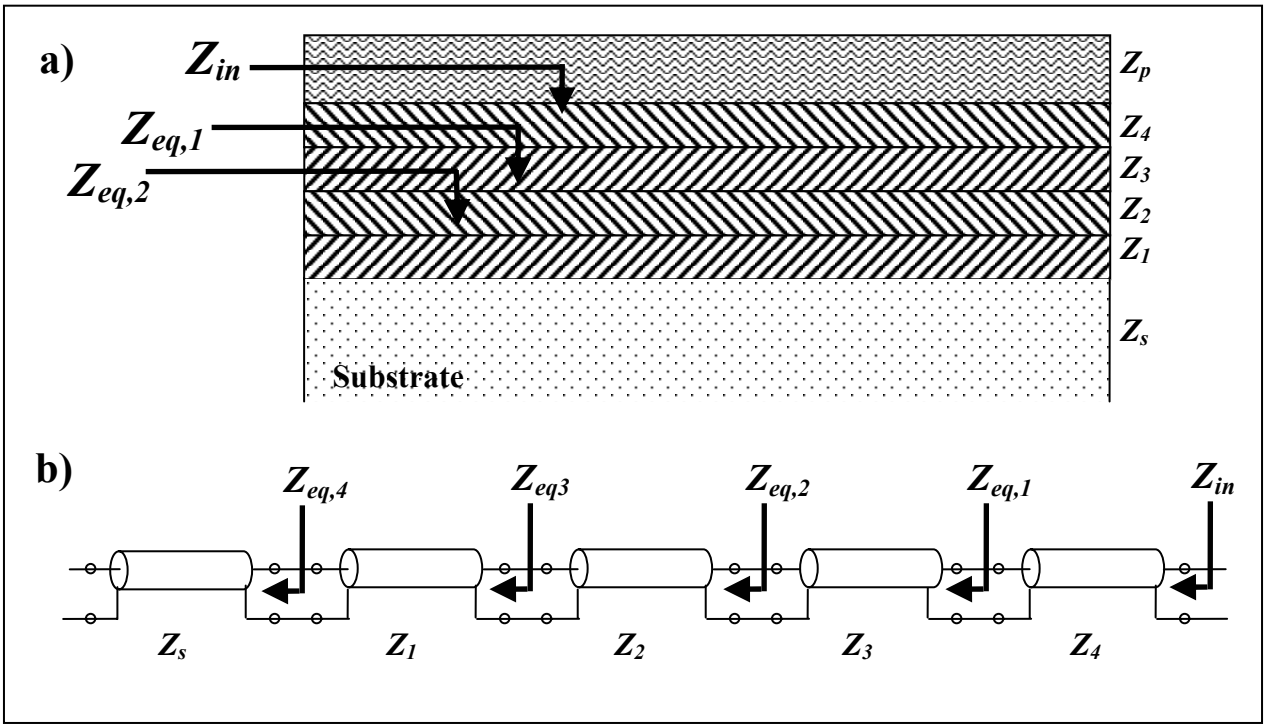

Figure 3.1. Schematic of a) the SMR configuration and b) the transmission line representation.

where k is the wave number, l is the length of the transmission line, Z_o is its characteristic impedance of the incident material, and Z_L is the apparent load impedance of the material beyond the boundary. In order to calculate the apparent acoustic impedance seen at the bottom boundary of the piezoelectric layer, shown in Figure 3.1 as Z_{in}, Equation (3.11) can be rewritten to estimate the effective impedance of the acoustic mirror and substrate as follows [76]

$$Z_{in} = Z_4\left(\frac{Z_{eq,1} + jZ_4\tan(kd)}{Z_4 + jZ_{eq,1}\tan(kd)}\right) \tag{3.12}$$

where d is the film thickness, Z_4 is the acoustic impedance of layer 4 and $Z_{eq,1}$ is calculated by

$$Z_{eq,1} = Z_3\left(\frac{Z_{eq,2} + jZ_3\tan(kd)}{Z_3 - jZ_{eq,2}\tan(kd)}\right). \tag{3.13}$$

This recursion is continued until all layers have been defined through to the substrate. This calculation is easily accomplished through the MATLAB script I created, which is presented in Appendix A.

Having implemented a script to model the mirror response, it was therefore easy to consider multiple material options for the mirror layers. Recall from Chapter 2 that alternating materials of high and low acoustic impedance yield a stronger reflection response. With that in mind, the materials considered are enlisted in Table 3.1, in which the acoustic impedances and shear velocities were calculated using Equations (2.3) and (2.4), respectively, and bulk values from Auld [55]. Note that the shear velocity is obviously required to determine the ¼-wavelength film thickness.

Table 3.1. Material options for use in the acoustic mirror. *Material properties for Ta_2O_5 were obtained from [77]. All others from Auld [55].

Material	Vertical Shear Stiffness, c_{44} (10^{10} N/m^2)	Density (kg/m^3)	Velocity (m/s)	Impedance (kg/m^{2}s)
ZnO	4.247	5680	2841	15.53 x 10^6
Fused SiO_2	3.12	2200	5132	11.3 x 10^6
Ta_2O_5*	5.69	8200	2634	21.6 x 10^6
$LiTaO_3$	9.4	7450	3552	26.5 x 10^6
Al_2O_3	14.5	3986	6031	24.0 x 10^6
W	15.2	19200	2814	54.0 x 10^6
Si	7.956	2332	5841	13.62 x 10^6

It is desirable to choose the material immediately adjacent to the piezoelectric ZnO to have a lower acoustic impedance, rather than a high one, as explained by Lakin, *et al* [31]. Multiple mirror pairings were considered and modeled using a center frequency of 2.0 GHz and 6 layers of alternating mirror materials, with the results demonstrated in Figure 3.2. As expected, the material pairing exhibiting the strongest degree of impedance mismatching demonstrated the most significant mirror response, though the responses shown in Figure 3.2 suggest that most of these mirror configurations should respond adequately when 6 layers are implemented.

Since Ta_2O_5 was on hand and demonstrated efficacy for previous designs for longitudinal devices [76], it was thought that this would work sufficiently for ZnO TSM devices. As is true for reflector gratings for SAW devices, the greater the number of gratings, the more efficient the reflector. Simulations were executed for various numbers of layers for alternating ¼-wavelength layers of fused silica (SiO_2) and Ta_2O_5. As can be

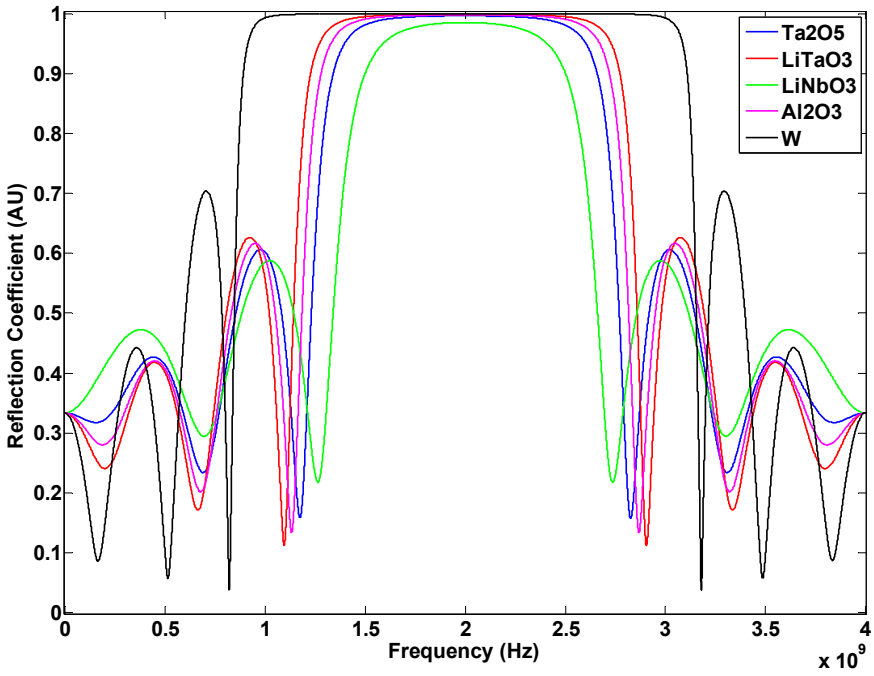

Figure 3.2. Modeled mirror reflection response from 0 to 4 GHz for multiple 6-layer mirror configurations.

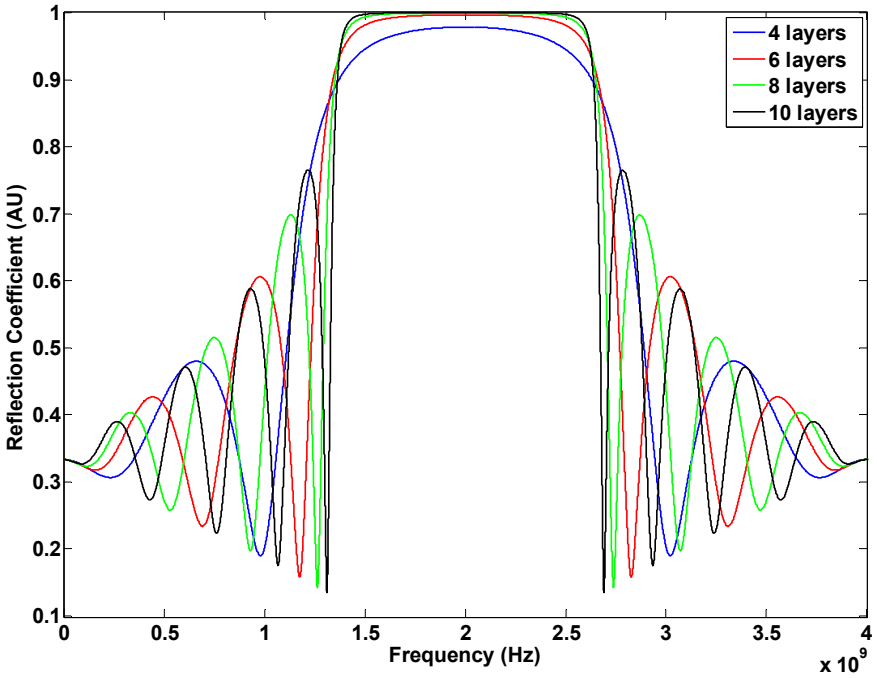

Figure 3.3. Modeled response of acoustic mirror using Ta_2O_5 and fused silica with 4, 6, 8 and 10 alternating layers at 1/4 wavelength thickness.

seen in Figure 3.3, significant improvement is demonstrated from 4 layers to 6 layers, with only slight improvement in efficiency from 6 layers to 8 layers (and practically no benefit extending to 10 layers). An important result of these simulations is broadband response of these mirror simulations. The reason this is advantageous is due to a significant shortcoming of RF sputtering thin films onto a substrate, which is the tendency for significant variation in film thickness. The parallel resonance frequency of a TSM BAW resonator is determined by

$$f_p = \frac{v_a}{2 \cdot d} \tag{3.14}$$

where d is the film thickness and v_a is the acoustic velocity. Significant variation in the film thickness will cause a commensurate variation in resonance frequency. The Unifilm PVD-300 sputtering system uses a patented deposition process that allows it to achieve 99.7% thickness uniformity across a three inch wafer. Even with this quality, a variation of 1% for a device intended to operate at 2 GHz would result in ± 215 MHz across the wafer. Therefore the broadband response of the mirror is desirable as it would accommodate these variations.

Simulations were also implemented with an odd number of mirror layers. The results of these simulations are shown in Figure 3.4. As can be seen, a notch feature appears at the center frequency where the desired resonance activity should be. This is expected due to the alternating nature of the low to high impedance clamped boundary versus the high to low impedance free boundary of the mirror [31]. Therefore odd layer implementations were not attempted.

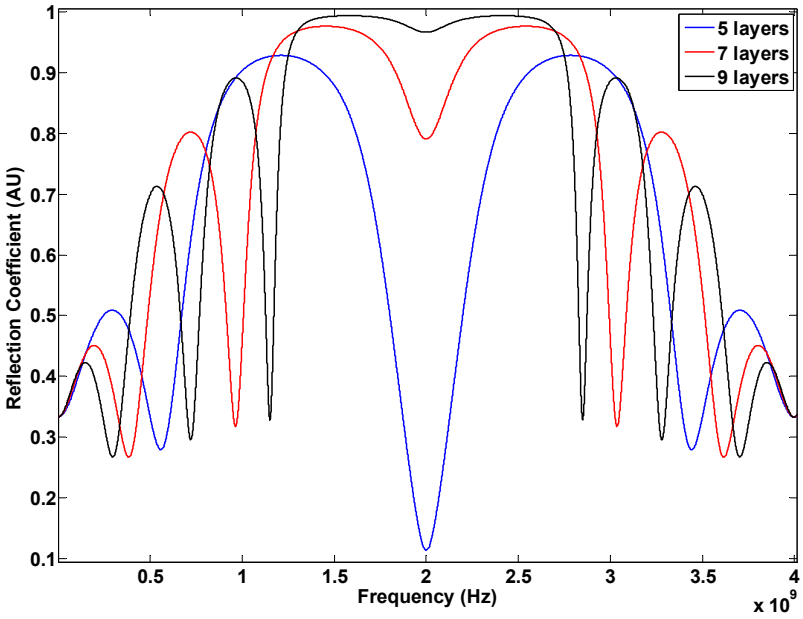

Figure 3.4. Modeled response of acoustic mirror using Ta_2O_5 and fused silica with 5, 7 and 9 alternating layers at ¼-wavelength thickness.

Deposition of *c*-Axis Oriented Thin Film ZnO

It is well known that ZnO can be deposited as a thin film through various methods, including chemical vapor deposition (CVD) [78, 79], metal-organic CVD [80-82], molecular beam epitaxy [83-85], electron beam (E-beam) evaporation [86], pulsed laser ablation [87], and the sol-gel method [88] to name but a few. Highly *c*-axis oriented films are consistently deposited, however, by means of RF magnetron sputtering [89-93]. RF magnetron sputtering involves the bombardment and energetic release of atoms, or sputtering, of a target material by an ion plasma beam. Magnetron sputtering is generally desired for slower deposition at lower vacuum levels which yields relatively well ordered crystal films with high uniformity. This method will be employed in this research for this

reason and because of the compatibility of the method with existing low-cost commercial fabrication. The *c*-axis orientation is important for the implementation of the desired thickness shear mode, as I shall demonstrate later in this chapter.

Multiple investigations testing one or more parameters for optimizing RF magnetron sputtering of ZnO have been performed including RF power (stepped and constant) [93, 94], oxygen:argon ratio and pressure [90, 92, 95], surface roughness [91], substrate/electrode material [96], and substrate temperature [97]. Interestingly, in nearly all studies, researchers concluded that the parameter (or parameters) under investigation was the most important variable for the high *c*-axis orientation of sputtered ZnO. Gardeniers *et al*, report one of the more thorough examinations by testing a variety of factors, including substrate material, substrate temperature, RF power, and distance between the target and the substrate [89]. Indicative of the findings broadly in the literature, they conclude that all parameters have a significant impact on the quality of the ZnO film.

For the purpose of this research, a protocol for high quality *c*-axis oriented ZnO has been employed by a former member of the lab, Dr. Shawn Pinkett, in collaboration with Dr. Jerry Siebert. Dr. Pinkett achieves high *c*-axis oriented ZnO using the parameters outlined in Table 3.2, the derivation of which are fully treated in [76]. All films were sputtered using the Unifilm PVD-300 RF/DC sputtering system, which employs a moving platform for the substrate wafer, both spinning the wafer and moving it periodically beneath the plasma beam in an effort to achieve a highly uniform coating across the wafer.

Table 3.2. Sputtering parameters used for deposition of highly *c*-axis oriented ZnO using the Unifilm PVD-300 sputtering system.

Parameter	Value
Temperature	325ºC
Deposition Pressure	5.02 x 10^{-3} Torr
Argon:Oxygen ratio	97.5 : 2.5
RF Power	135 W
Distance from target to substrate	6.9”
Substrate material	<0 0 1> Silicon, mechanical grade

X-ray Diffraction Characterization

The crystallinity of thin films is often gauged by making X-ray diffraction (XRD) measurements of the film. Crystallinity describes the condition under which atoms are arranged in a regular pattern. Single-crystal films require that there is a smallest volume element that by repetition in three dimensions sufficiently describes the crystal. This is extremely difficult to achieve through conventional synthetic thin-film deposition methods, of course, so it is necessary to gauge the degree of ‘poly-crystallinity’ of a thin film in order to assess its quality. The measurements most often used for assessing thin films are the full width at half maximum (FWHM) of the θ–2θ scan and of the 2θ-ω rocking curve scan, in which Figure 3.5 describes the terms used. θ describes the angle of incidence from the target platform supporting the wafer while 2θ represents the angle from that incidence vector to the receiver device. ω is the term used to describe any tilt applied to the support platform. The θ–2θ scan varies the θ and 2θ angles and gives the diffraction angle peak revealing the predominant crystal orientation. The FWHM is a measure of the span of the reflection peak at half-maximum and the θ–2θ FWHM in particular is the parameter most often described in the literature to characterize the crystal

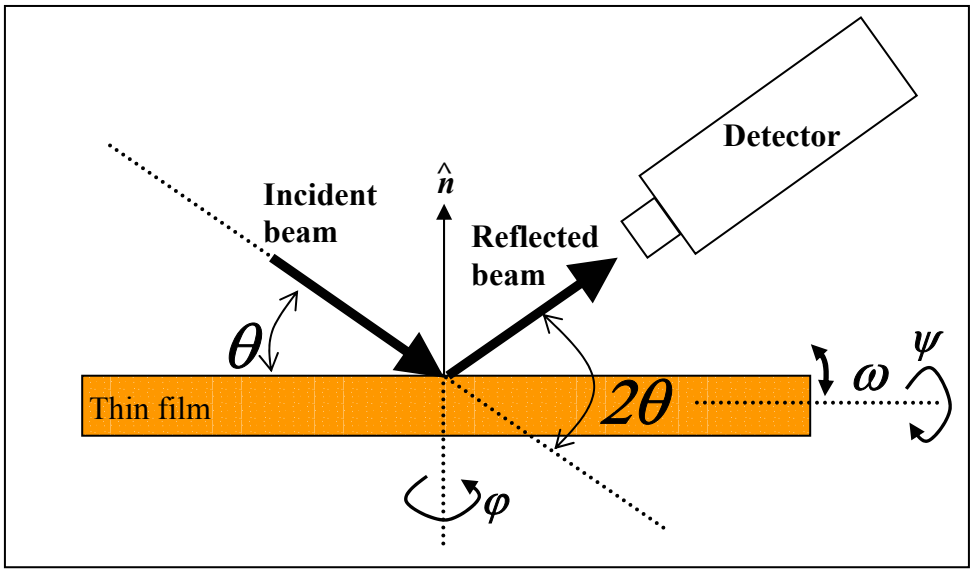

Figure 3.5. XRD for assesmment of thin film crystallinity.

uniformity of a thin film. The 2θ-ω rocking curve scan is generally considered a better assessment of the quality of the film [98] and involves varying ω at a fixed 2θ angle, which reveals a detailed structure of the peak being analyzed. Due to the prevalence of θ–2θ scans demonstrated in the literature, these were used for the purpose of this film characterization.

The films were characterized using a Philips X'Pert Materials Research Diffractometer using a hybrid mirror/monochromator incident optics and a ¼-degree receiving slit in the diffracted optics beam path. Considering that high c-axis orientation is a principle component of achieving the desired TSM resonator, it was decided that ZnO should be deposited on multiple substrates to find out how much of an impact the underlying substrate crystal structure would have on the epitaxial growth of ZnO. ZnO was deposited on DC sputtered W, RF sputtered Ta_2O_5, RF sputtered SiO_2, polished (1 0 0) silicon, polished (1 0 0) gallium arsenide (GaAs), and polished (0 0 1) sapphire (Al_2O_3). The first 3 surfaces were chosen due to their potential as components of the

acoustic mirror, and the final three for general comparison purposes. The polished sapphire was of particular interest, as it is considered lattice matched to *c*-axis oriented ZnO and should yield the highest degree of orientation [89, 96]. By contrast, the polished GaAs is not lattice matched and should therefore yield a relatively lower degree of crystallinity. The results of these depositions are demonstrated in Figure 3.6 below. Note

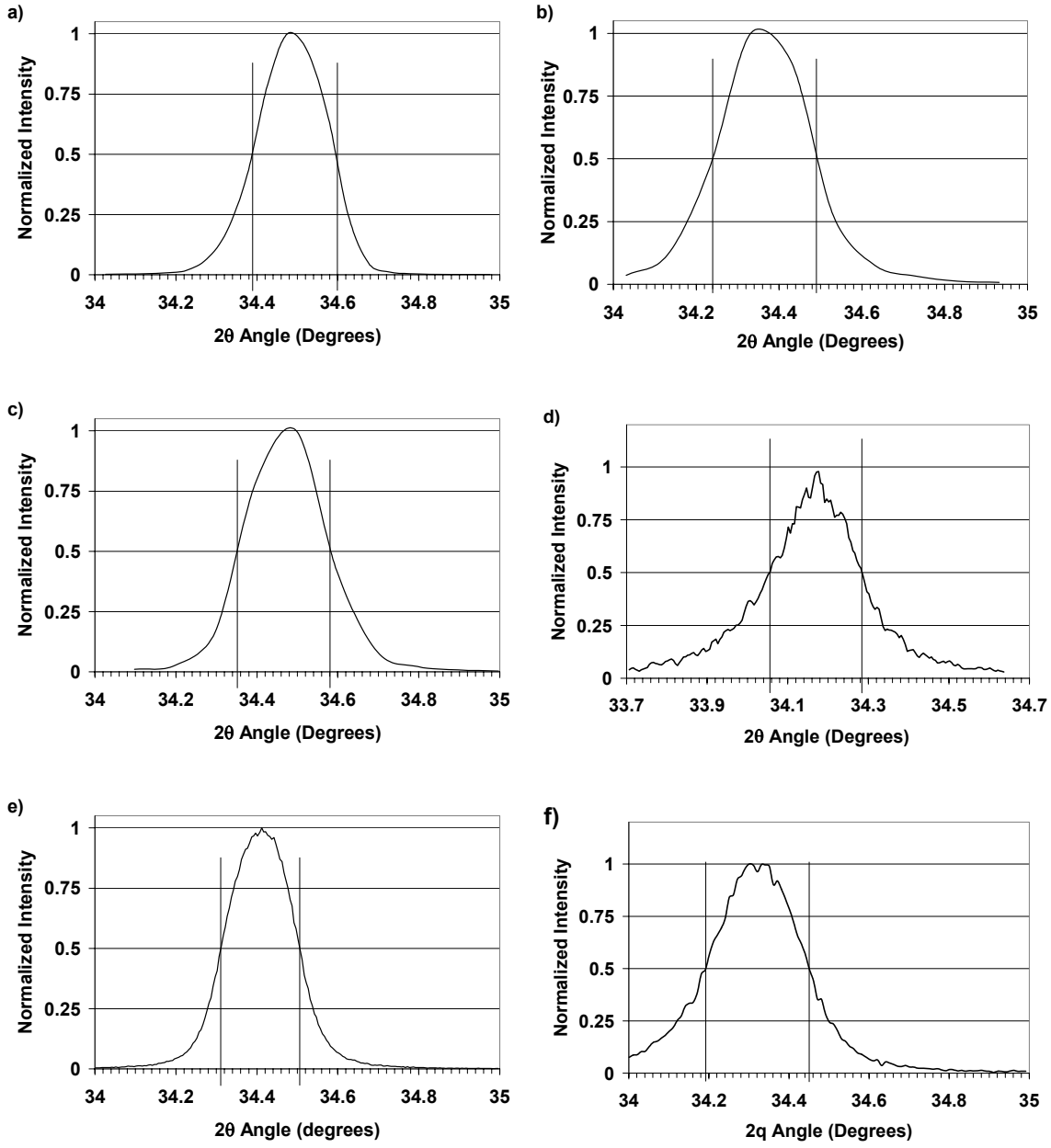

Figure 3.6. *θ–2θ* XRD scans of ZnO RF sputtered onto a) Sapphire, b) GaAs, c) Silicon, d) W, e) Ta_2O_5 and f) fused silica.

that results indicate that there was little variation in the quality of the ZnO film due to the substrate crystal. This gave me confidence that ZnO deposited using the protocol described in Table 3.2, would yield high crystallinity regardless of the substrate material. That is to say, the mirror surface material would not impact the ability of the ZnO film to support the desired TSM. The 2θ FWHM measurements for all substrate materials are summarized in Table 3.3. Incidentally, these results indicate *c*-axis oriented crystallinity on par with that reported by others referenced in this document [89, 90, 92-97].

Table 3.3. 2θ FWHM from XRD scan results of ZnO RF sputtered onto various surfaces.

Base Layer	2θ FWHM
Sapphire	0.20º
GaAs	0.25º
Si (1 0 0)	0.23º
W	0.24º
Ta_2O_5	0.20º
Fused Silica (SiO_2)	0.26º

From ZnO to Ta_2O_5

Figure B.1 demonstrates the initial SMR design for achieving the base transducer for my biosensor application. Many wafers were fabricated with multiple electrode configurations and mirror thicknesses attempted over a period of nearly 2 years before I finally discovered a resonance response using the parameters shown in Table 3.4. The majority of this time was spent on alternate electrode configurations and broad approaches to achieving the LFE design. The electrode configurations attempted over this time period are demonstrated in Appendix B. Note that the configuration that finally

worked utilized an 8-layer mirror, consisting of SiO_2 as the low acoustic impedance material and Ta_2O_5 as the high acoustic impedance material, and ZnO as the piezoelectric crystal. Each layer was deposited via RF sputtering using the parameters described in Table 3.4. The electrodes were deposited by electron beam evaporation at a thickness of 1200 Å of Al with a 300 Å adhesion layer of Cr. Layer thicknesses were chosen to yield the 8-layer mirror response reflected in Figure 3.7. A SEM image of the profile of the fabricated device is shown in Figure 3.8, confirming the fabrication result was as intended.

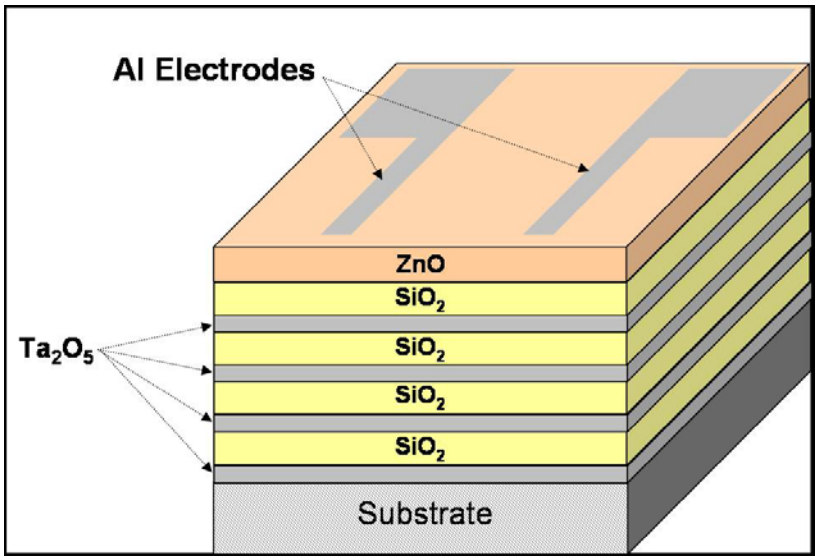

Figure 3.7. Initial ZnO SMR design.

Table 3.4. Deposition parameters for original device design.

Parameter	**ZnO**	**Ta_2O_5**	**Fused Silica (SiO_2)**
Layer Thickness	750 nm	450 nm	850 nm
Temperature	325ºC	Ambient	Ambient
Deposition Pressure	5.03 x 10^{-3} Torr	5.02 x 10^{-3} Torr	5.02 x 10^{-3} Torr
Argon:Oxygen ratio	97.5 : 2.5	97.5 : 2.5	98 : 2
Power	135 W @ 98 V	115 W @ 121 V	281 W @ ~58 V
Deposition Rate	400 Å/min	600 Å/min	300 Å/min
Distance from target to substrate	6.9”	6”	6”

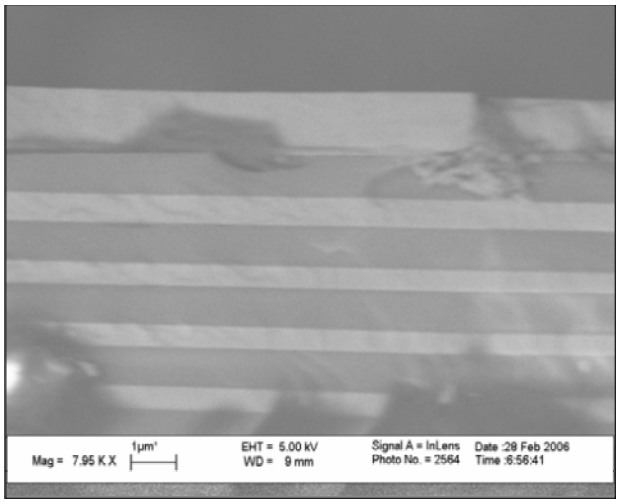

Figure 3.8. SEM image of profile of fabricated device, confirming output of fabrication to meet the design specifications.

Resonator performance was assessed using a Cascade Microtech 9000 probe station and Cascade Microtech ACP40/GSG-150 probes. Results were recorded with a HP8753C Network Analyzer equipped with an 85047A S-Parameter Test Set. The resonator is a one port device, so the measurements made are referred to as the reflection scattering parameters, or S_{11} response. The S_{11} response is a ratio of the reflected signal over the incident signal over a given frequency range. From the S_{11} data, it is in turn possible to obtain the impedance response of the resonator through the following transformation:

$$Z_{in}(f) = Z_o \frac{1 + S_{11}(f)}{1 - S_{11}(f)} \tag{3.15}$$

where Z_o is the load impedance (generally 50Ω). One-port S_{11} responses of each device are the first tests I perform on any fabricated resonator and give the best information regarding the resonance quality. Due to the parallel electrode configuration required for LFE and the semiconductor nature of ZnO, the scattering response should look like a simple capacitor, in which a relatively constant reflection of the incident signal is observed. As the frequency range is swept, there is a range in which the physical

parameters of the thin film and the transduction properties of the piezoelectric crystal absorb the incident signal, transforming it into a mechano-acoustic wave that propagates through the bulk. At the resonance condition, a standing wave is achieved and a maximum transduction of electrical into mechanical energy is established. The narrower the frequency range, or band, of that transduction and the greater the overall absorption of the incident electromagnetic energy, the stronger the performance of the resonator. This is reflected in higher resonance quality factor, Q.

A typical S_{11} response for these initial resonators is shown in Figure 3.9.A below. As can be seen, the device exhibits a characteristic resonator reflection scattering response, albeit a relatively poor one, at around 1 GHz. These resonance conditions are deemed weak as the response band is very wide and the overall energy absorbance is relatively small. Figure 3.9.B and 3.9.C shows the conversion of the S_{11} response into the corresponding magnitude of the input impedance response, accomplished through the relationship described in Equation (3.15), and the Smith Chart of the complex reactance, respectively. It must be noted, however, that as this was the first resonance observed after nearly 2 years of experimentation with various configurations, I was still relatively excited about the breakthrough. I was surprised by the response, however, as the resonance observed would have meant the TSM wave launched in ZnO was resonating with an acoustic velocity of 1,980 m/s, much lower than the expected 2,840 m/s (see Chapter 2). I hypothesized that several possibilities existed at this point. These included the possibility that the dopants in the ZnO target material used for sputtering were substantially affecting either the density or stiffness of the sputtered film or that the physical properties of the mirror itself was not focused properly on the resulting acoustic

A) B)

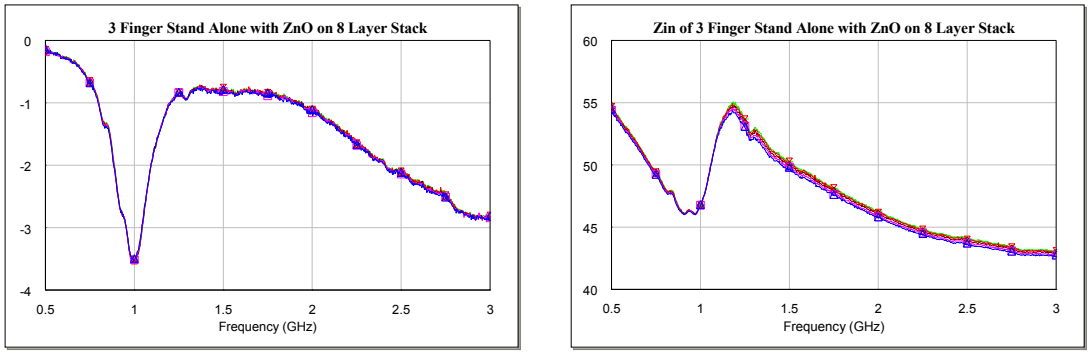

C)

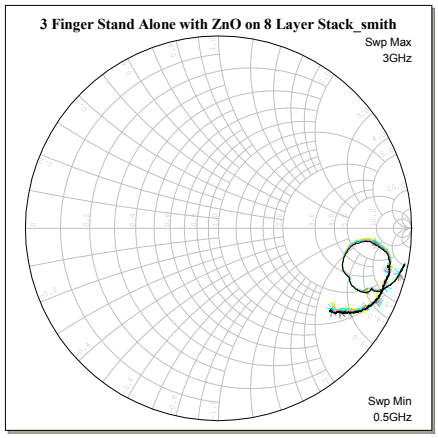

Figure 3.9. A) S_{11} response, B) $|Z_{in}|$ response, and C) Smith Chart showing typical responses for 8-layer mirror resonators with ZnO on top.

wave and may be scattering the energy.

My initial excitement at finding a resonance was substantially diminished when I fabricated a subsequent wafer with a substantially thinner layer of ZnO. Upon probing this next series of resonators with the probe station, I observed the exact same response as with the previous fabrication. Recall from Equation (3.14) that the resonance frequency of a bulk acoustic wave resonator device is determined directly by the thickness of the piezoelectric film. This led to yet another fabrication in which I fabricated electrodes directly onto the 8-layer mirror, in which fused silica was the top layer, and no ZnO was present. This wafer yielded the results shown in Figure 3.10 below. As can be seen, these

A) B)

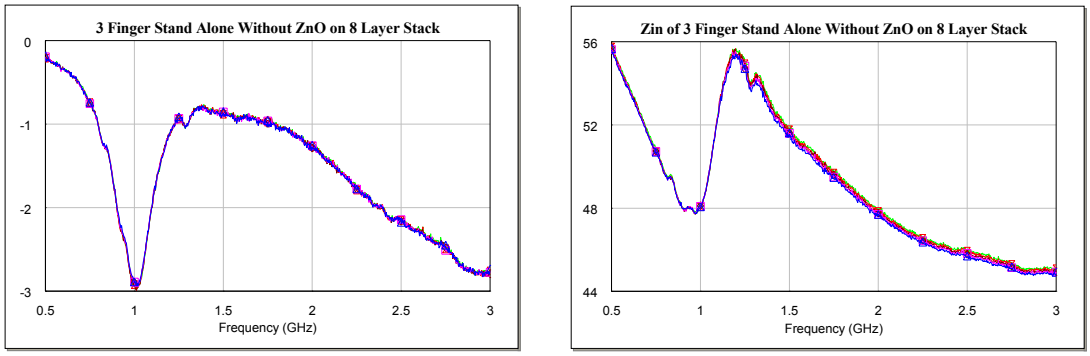

C)

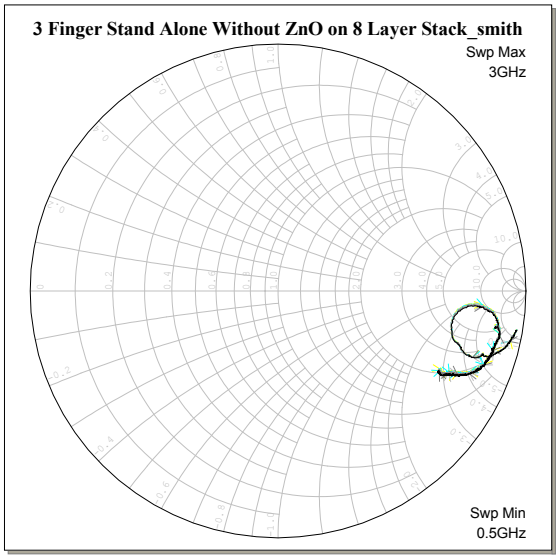

Figure 3.10. A) S_{11} response, B) $|Z_{in}|$ response, and C) Smith Chart showing typical responses for 8-layer mirror resonators ***without*** ZnO on top.

responses are remarkably similar to those shown in Figure 3.9, meaning the resonance had nothing to do with ZnO. At this point, it was thought that perhaps Ta_2O_5 could be piezoelectric and led to the investigation described in the following section.

The Case for Piezoelectric Ta_2O_5

Piezoelectric Ta_2O_5 have been employed for SAW devices [99-103]. Thin *x*-axis oriented monoclinic crystalline Ta_2O_5 films deposited by DC diode sputtering on fused

quartz with *y*-directed SAW propagation has been successfully demonstrated [104, 105]. In another application, Ta_2O_5 films have been deposited as a loading layer on top of ST-cut quartz in an effort to optimize SH-SAW performance. At an optimal thickness, this layer was shown to improve K^2 and reduce insertion loss over devices without the film [106].

Despite the characterization of Ta_2O_5 for SAW applications, there has not been much investigation into bulk acoustic modes for piezoelectric Ta_2O_5 to date. I therefore decided to investigate the bulk acoustic properties of Ta_2O_5 in a thin film Ta_2O_5/SiO_2 stack deposited by RF magnetron sputtering. The motivation for this was to generate a resonator which exhibits the TSM of operation through LFE. For a surface-only mounted electrode configuration, the separation of the Ta_2O_5 layers by a SiO_2 layer might help to focus the electric field in a horizontal orientation through the Ta_2O_5 layer. For lateral field excitation applications, it was believed that this would help to improve the electrical coupling to a TSM mode.

A thin film 3-layer stack of alternating SiO_2 and Ta_2O_5 was deposited by RF magnetron sputtering using the Unifilm PVD-300 sputtering system. The layers were alternating fused silica (SiO_2) and Ta_2O_5, in which Ta_2O_5 was the first layer deposited onto a mechanical-grade Si (1 0 0) wafer. Electrodes were fabricated on top of the stack in the configuration shown in Figure 3.11. The sputtering parameters for the 3-layer alternating stack are provided in Table 3.4. The SiO_2 layer was determined to be approximately 750 nm thick while the Ta_2O_5 layers were approximately 450 nm thick. The final thicknesses of each layer were verified using SEM imaging, and can be seen in Figure 3.12 from a cross-sectional view. The SEM images were taken using a LEO 1530

Thermally-Assisted Field Emission Scanning Electron Microscope system. The electrodes were 150 nm of aluminum deposited on top of a seeding layer of 30 nm chromium using a CVC E-beam evaporator and standard photolithography process, outlined in Appendix C.

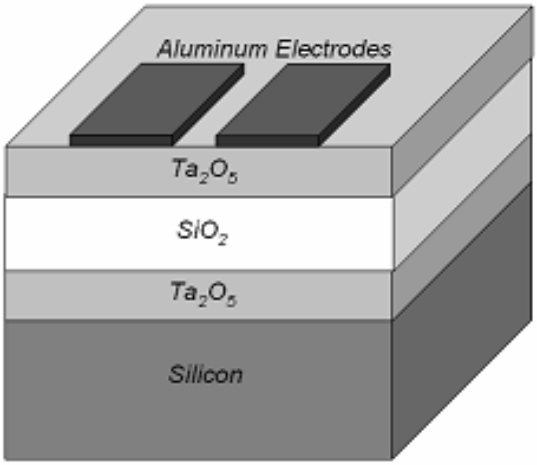

Figure 3.11. Device design for LFE of a piezoelectric Ta_2O_5 TSM resonator**.**

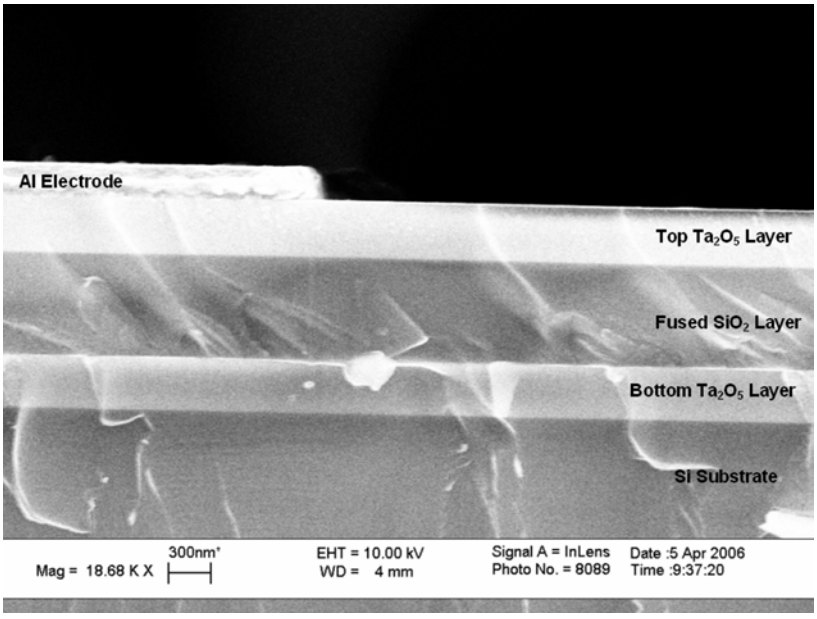

Figure 3.12. SEM image of profile of fabricated resonator.

The electrodes were designed such that the electric field created upon excitation would be perpendicular to the wafer surface normal. This laterally-oriented electric field was already found to excite the resonance shown in Figures 3.9 and 3.10. It was further believed at this point that this electrode configuration was exciting the TSM acoustic wave in the Ta_2O_5 (i.e. through LFE). It was therefore required to demonstrate that this was even theoretically possible.

X-ray Diffraction Characterization of Ta_2O_5

XRD data were taken on a Philips X'Pert Materials Research Diffractometer using a hybrid mirror/monochromator incident optics and a ¼-degree receiving slit in the diffracted optics beam path. Previous investigations with DC diode sputtering have found a significant variety in the growth of Ta_2O_5 crystals by altering the deposition parameters. A 2θ-ω scan of the film indicated a weak polycrystalline peak at ~26.4°, indicating an (11 0 1) orthorhombic *2mm* crystal orientation shown in Figure 3.13. The peak was found only after applying a 10º offset on ω to the wafer upon running the 2θ-ω scan, however, indicating the crystal must have grown offset from the normal of the substrate by that angle. The pole plot depicted in Figure 3.14 is a 2.5-D plot of the 4-pole symmetry about the φ axis with a 90º rotation on ψ for the radial axis. Three of the peaks in the pole plot are readily apparent. The fourth, however, while well above the noise floor, is a much smaller peak than the three other peaks. Other samples sputtered under the same condition required a tilt of ~12.3º for the [11 0 1] peak to be observed. This was found to be repeatable under the sputtering conditions given in Table 3.4. Using a reciprocal space diagram and powder diffraction X-ray tables, it was determined that if one assumes that

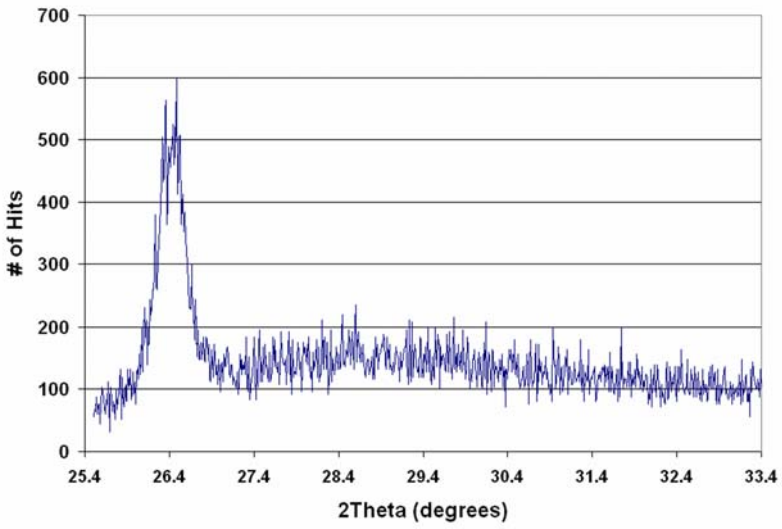

Figure 3.13. 2θ-ω scan of 10º tilted Ta_2O_5

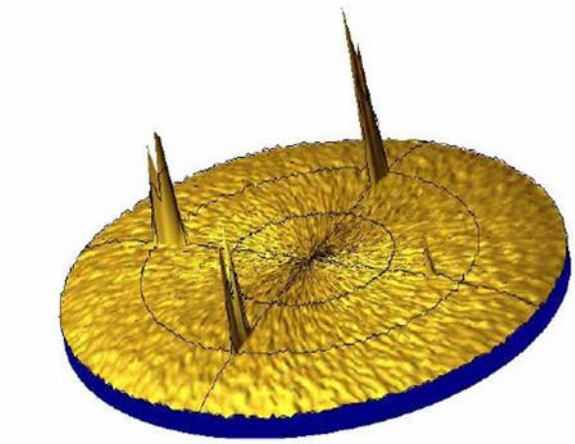

Figure 3.14. 2.5-D pole plot, or φ scan, of 4-pole symmetry**.** [Prepared by Dr. Walter Henderson, Georgia Institute of Technology]

the [17 0 1] axis is aligned parallel to the Si [1 0 0] axis, then the [11 01] axis is tilted approximately 10 degrees to the low angle side as was observed. If one assumes that the [19 0 1] is aligned to the Si, the tilt is ~12.3 degrees, which is the offset that was seen in some of the samples. Initially, these alignments do not seem to make much sense from an epitaxial alignment point of view, but after examining at the lattice constants, there may be a viable explanation. The orientation with the [17 0 1] ([19 0 1]) axis parallel to

the Si [1 0 0] axis has an in-plane periodicity of 6.728 (6.628) Å. The ratio of this distance for the [17 0 1] ([19 0 1]) orientation to the Si [1 0 0] lattice constant, 5.43095 Å at room temp, is thus 5:4 (11:9 close to 6:5) within about 1%.

Compared to the values in the cases where the [1 0 0], [0 1 0], and [0 0 1] Ta_2O_5 directions are parallel to the Si [1 0 0] – 81:10, 7:5 and 7:8, respectively – it is likely that the proposed orientations are the most energetically favorable way for the Ta_2O_5 to achieve a harmonic or periodic lattice match on Si. In particular the elevation of the Ta_2O_5 [1 0 0] axis out of the interface plane seems to be strongly preferred. That axis with its large lattice constant is a difficult match to the underlying silicon, and the substrate therefore is a poor template for that potential orientation. The scans show that there is clearly an amorphous component as evidenced by the broad slowly, trailing hump at lower 2Θ angles, shown in Figure 3.13. However, the φ scans strongly suggests the presence of oriented, crystalline (likely polycrystalline) Ta_2O_5.

Thickness Shear Mode in Piezoelectric Ta_2O_5

Once the crystal orientation is known, it is possible to solve the Christoffel equation described in Equation (3.1) to find the modes of propagation in the bulk given a defined electrical excitation direction. We begin by considering the non-piezoelectric Christoffel equation, as provided in Equation (3.1) and (3.2). It is estimated that the oriented Ta_2O_5 films belong to a class of *2mm*. The orthorhombic system class *2mm* tensors are used in the calculations here because of the XRD results discussed above. All solutions to the Christoffel equation were implemented in MATLAB, using the code presented in Appendix E.

If the direction of propagation is chosen to be in the z direction, then l_x and l_y go to zero, and l_z becomes 1. The Euler angles are chosen such that the rotated system corresponds to the z-axis in the direction normal to the (17 0 1) plane and the x-axis can be chosen to be oriented in the plane parallel to (17 0 1) and in line with the electric field. Since there are different manners of describing Euler angles, I have chosen the one most familiar to us. In that system, ϕ corresponds to a counterclockwise rotation about the z-axis, θ corresponds to a counterclockwise rotation about the new y'-axis, and φ corresponds to a counterclockwise rotation about the new z''-axis. Under this convention, the Euler angles to describe a system in which the z-axis is normal to the (17 0 1) plane are $\phi = 0$, $\theta = 86.633^{\circ}$ and $\varphi =$ X where X is the angle corresponding to the direction of the electric field. Since our electrodes are fabricated on top of sputtered Ta_2O_5, X is arbitrary because the exact orientation of the electrodes in the x-y plane with respect to the crystal lattice is unknown. For simplicity, I will set $\varphi = 0$.

For the Ta_2O_5 stack structure described in Figure 3.11, the electric excitation is orthogonal to the wave propagation direction. Therefore, if the wave propagation is in the direction of the z-axis, the electric field is in the x-y plane. From the general solutions, it is possible to determine that the exact orientation of the electric field with respect to the crystal lattice is not as important here because it yields similar results.

Here I will describe the coupling and acoustic wave propagation for the purely x-axis oriented case since symbolically the solutions are much simpler than those for the odd-angle rotated case and will then attempt to explain how the (17 0 1) normal relates to this. First, the orthorhombic *2mm* tensors, obtained from Nakagawa, *et al* [20], were transformed such that the z-axis is normal to the (1 0 0) surface of Ta_2O_5. Then, the wave

propagation is specified to be in the z direction of the transformed axes and the electric field in the direction of the x-axis. The symbolically solved Christoffel matrix comes out to be:

$$\begin{bmatrix} c_{55} & 0 & 0 \\ 0 & c_{66}+\dfrac{e_{36}^2}{\varepsilon_{33}} & 0 \\ 0 & 0 & c_{11} \end{bmatrix}$$

The eigenvalues of this matrix correspond to terms that can be used to solve for the acoustic velocity for each of the three wave propagation modes. Upon inspection, it is possible to see that only the y-directed particle displacement is piezoelectrically stiffened. This means that for an electric field in the horizontal plane, parallel to the surface, a shear wave will be generated with a propagation direction normal to the surface. No other component of the Christoffel matrix contains a stiffened term. Similarly, if I solve for the Christoffel matrix with an electric field designated along the y-axis of the crystal, the Christoffel matrix becomes

$$\begin{bmatrix} c_{55}+\dfrac{e_{25}^2}{\varepsilon_{22}} & 0 & 0 \\ 0 & c_{66} & 0 \\ 0 & 0 & c_{11} \end{bmatrix}$$

which shows that this time, the particle displacement is parallel to the surface, but normal to the electric field. The coefficients involved in the stiffness have changed, but this is as expected for an orthorhombic crystal. Therefore, one can imagine that an electric field oriented at some angle between the x and y axes of the transformed system would provide a particle displacement normal to the field in the x-y plane with a wave propagation

direction oriented toward that of the *z*-axis. Indeed it does, but the symbolic eigenvectors of the solved Christoffel matrix are too complicated to show here, even in the simplest case of a 45° offset.

The above situation has been solved assuming strong crystal orientation toward (1 0 0). It has already been shown, however, that the deposited film exhibits a highly *poly*crystalline mix with a predominant orientation along (17 0 1). To accurately predict any resulting piezoelectric activity, one must rotate the tensors according to the appropriate Euler angles described above and then solve and interpret the resulting Christoffel matrix. For the case of an *x*-directed electric field, it can be demonstrated that the particle displacement for the longitudinal case and for the shear cases are not directly aligned with the *z* and *x* axes respectively. They also show no piezoelectric stiffening just as in the (1 0 0) case discussed above. Coupling is reflected, however, in the *y*-direction and the particle displacement is directly aligned with the *y*-axis, as expected. For the case of a *y*-directed electric field, on the other hand, no coupling for the *y*-directed particle displacement shear mode is seen because of the angle difference between the (17 0 1) and (1 0 0) faces. Piezoelectric coupling due to the *y*-directed field does occur, however, for the longitudinal and *x*-directed shear modes. Therefore, we can conjecture that most likely, the lateral excitation of the Ta_2O_5 consists of multiple directions of particle displacement and will depend upon the exact angle of the electric field with respect to the crystal orientation. I have shown, however, that a thickness directed shear wave theoretically can be excited in both (17 0 1) and (1 0 0) oriented Ta_2O_5 thin films.

Finite Element Modeling of Ta_2O_5 LFE SMR

In addition to the Christoffel matrix calculations, electrostatics finite element modeling of the system was carried out using the software package Comsol Multiphysics™. The motivation behind this was two-fold. First, it helped to clarify the orientation of the electric field in the Ta_2O_5 stack as generated from the electrodes. It must be confirmed that an electric field parallel to the surface does emerge in the regions of interest in order to verify the lateral excitation of the device. Secondly, by modeling the system, it is possible to look at the relative levels of electrical energy density within the stack layers. Figure 3.15, prepared by Dr. Corso, shows the electric field through the layered stack. The first and third layers are Ta_2O_5 sandwiching a layer of SiO_2. Below the stack is the (1 0 0) mechanical-grade silicon substrate wafer that the entire structure was fabricated upon.

The resulting simulation shows that the electric field is *much* denser in the Ta_2O_5 layers than in the SiO_2 and is fairly horizontal in the active area of interest in between the electrodes (indicated by the box). It appears that the electric field in the top Ta_2O_5 layer is

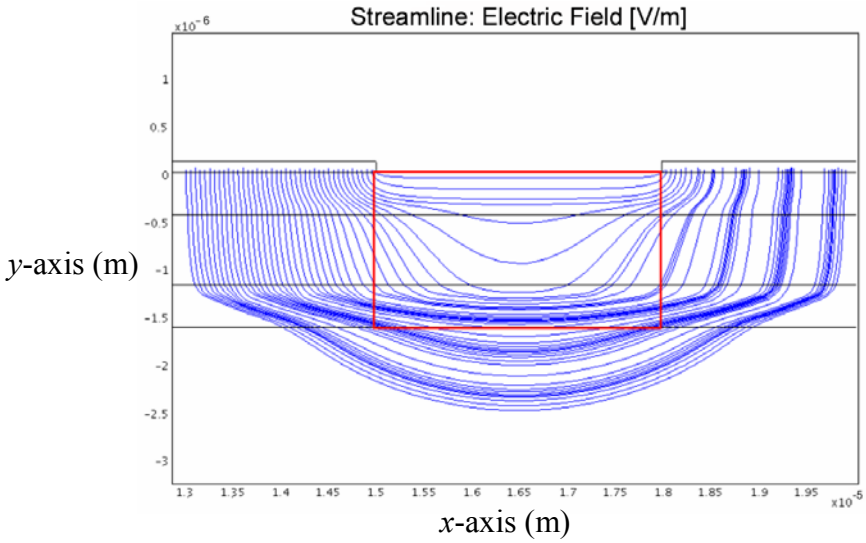

Figure 3.15. FEM plot of the electric field line orientation in active area (indicated by box). [Prepared by Dr. Christopher Corso, Georgia Institute of Technology]

relatively parallel to the surface. The permittivity of the SiO_2 is such that it draws the E-field more directly through to the subsequent layer. The permittivity of Ta_2O_5 then redirects the E-field in a manner parallel to the surface, which provides lateral excitation of the film. Figure 3.16 is an arrow plot where the size and direction of the arrow demonstrates the relative strength and orientation of the field in the stack. In the top Ta_2O_5 layer, the arrows within the active region are very well aligned. The electric field in the SiO_2 layer appears to have a more vertical component, especially towards the edge of the active area. The results from these simulations offer an independent confirmation that a lateral electrical excitation field exists in the Ta_2O_5 which substantiates the calculations made in the previous section. The finite element results also demonstrate the usefulness of the thin-film stack structure for electric field manipulation with regards to the piezoelectric films.

In order to calculate the energy density in the stack layers, finite element modeling was again utilized. The finite element simulation results in 2-D were extracted with each

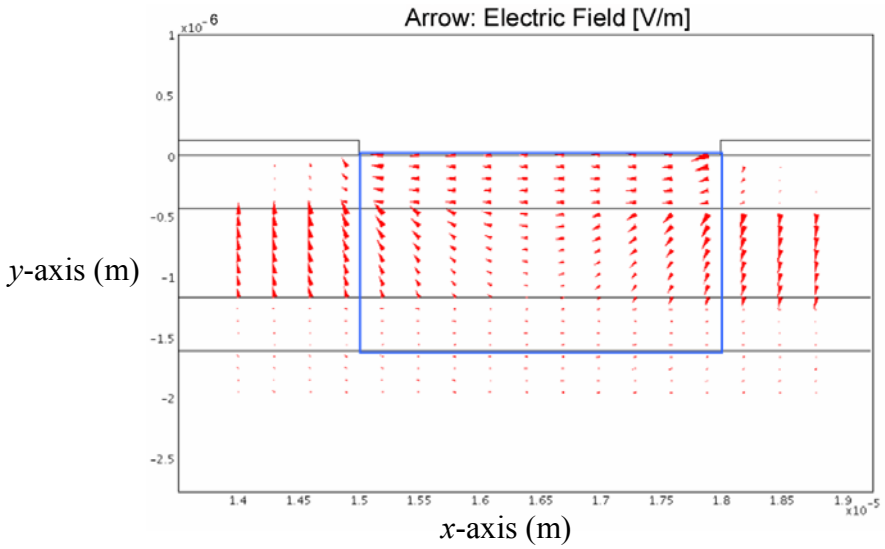

Figure 3.16. FEM arrow visualization of electric field orientation and relative strength. [Prepared by Dr. Christopher Corso]

point paired with a finite energy density. For each layer, the energy density values of all the points falling within the active area of interest of the layer were summed and divided by the total number of points to give the average energy density at a location within the active area. The totals were found and the ratio of the average energy density in the layer to the lowest average energy density in the stack was computed for each layer. The results are summarized in Table 3.5. From the data, it is apparent that the average energy density each Ta_2O_5 layer is greater than the corresponding average energy density of the SiO_2 layer directly above it. Clearly, there is some propensity for the electrical energy to migrate towards the Ta_2O_5 layers. This can be explained by the large relative dielectric permittivity of Ta_2O_5 which is approximately 19.5 in the *y*-axis direction [107] as compared to 3.8 for fused quartz [108]. Figure 3.17 shows a visualization of the energy density for the active area of the stack in between the electrodes. The lighter color corresponds to a higher energy density whereas the darker color corresponds to a lower energy density. It is clear from the image that the greatest energy density exists just at the edges of the electrodes in the top Ta_2O_5 layer. The layer contains a large amount of electrical energy density within the active region. This is important because the larger energy density allows for a better opportunity for coupling electrical energy into a mechanical wave. In the following layers a greater amount of energy density is contained in the Ta_2O_5 layer than in the SiO_2 layer which is desirable for the excitation of an acoustic wave in the Ta_2O_5.

Table 3.5. Average energy density for each layer. [Prepared by Dr. Christopher Corso]

Layer	Average Energy Density Ratio
Ta_2O_5 Layer 3	81.27:1
SiO_2 Layer 2	1.00:1
Ta_2O_5 Layer 1	1.82:1

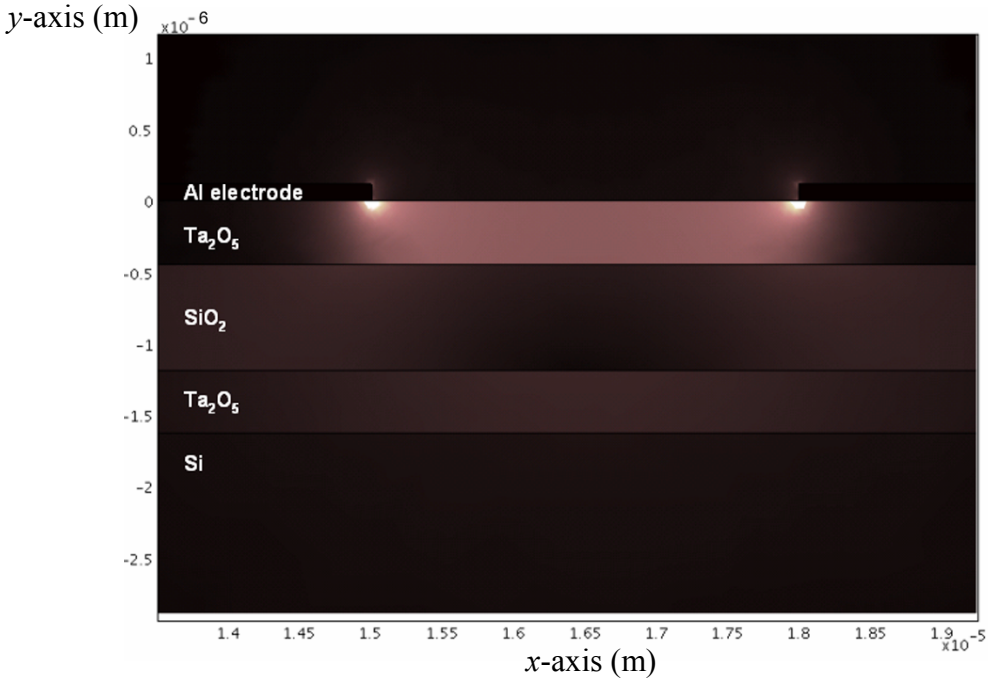

Figure 3.17. Visualization of electric energy density. [Prepared by Dr. Christopher Corso]

Ta_2O_5 Resonator Results

It was determined that the strongest resonance responses came from device arrays with the electrode configuration shown in Figure 3.18. RF probing of individual devices (i.e. those not fabricated as part of an array) yielded weaker resonance. Several regions of resonance regions were observed for each device around 450 MHz with the sharpest peak generally in the area of 525 MHz. As can be seen from a representative Smith Chart shown in Figure 3.19, multiple clear loop patterns emerge, indicative of resonance, are present. This response is typical of the response observed in a vast majority of the devices tested. The multiple peaks may be attributed to either the multiple layers of or the polycrystalline nature of the Ta_2O_5. From a sampling of 10 "good" devices, an average unloaded *Q* of these resonators is approximately 1,500, which is quite high

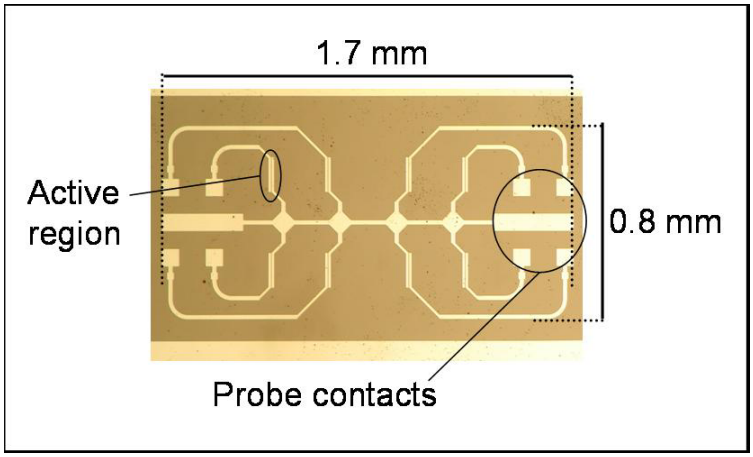

Figure 3.18. Electrode configuration used for results of Ta_2O_5 resonator tests.

Without the appropriate stiffness tensor quantities for the bulk material, it is difficult to derive the phase velocity value and thus the resonant frequency of a thickness shear wave for comparison with our results. However, in an attempt to further establish the existence of a thickness shear mode, a simple water test could be applied since water cannot support a shear wave but can support a longitudinal wave. If the acoustic activity

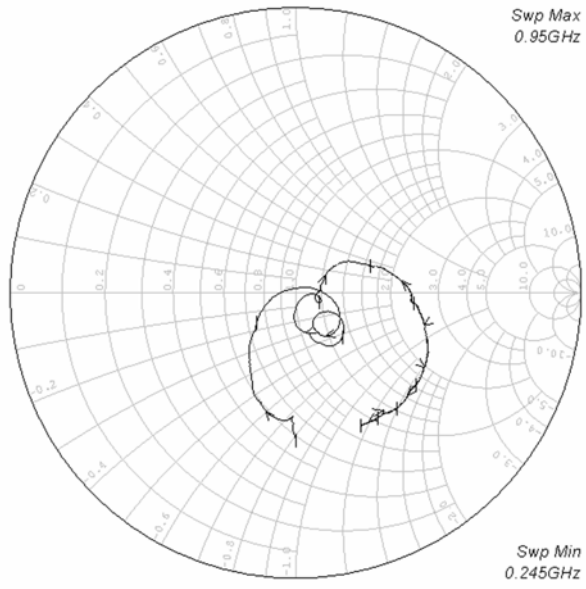

Figure 3.19. Smith Chart of Ta_2O_5 resonator array.

were longitudinal, application of de-ionized water at the surface would devastate the acoustic resonance observed in the device. Figure 3.20 below shows the response before (squares) and after (triangles) application of water to the surface. As can be seen, the water had no deleterious affects on the S_{11} suppression and a negative frequency shift occurred after water was observed of approximately 167 MHz. According to Sauerbrey [109], this response is to be expected from a TSM device, roughly described by Equation (2.5). It is reasonable to assume that the observed frequency shift could indicate a mass loading effect of the surface of the device by the de-ionized water. This further confirms the prediction made by analysis of the Christoffel solution that the resonance is a TSM wave. The response to the water test was shown to be repeatable across different device configurations in various locations about the wafer.

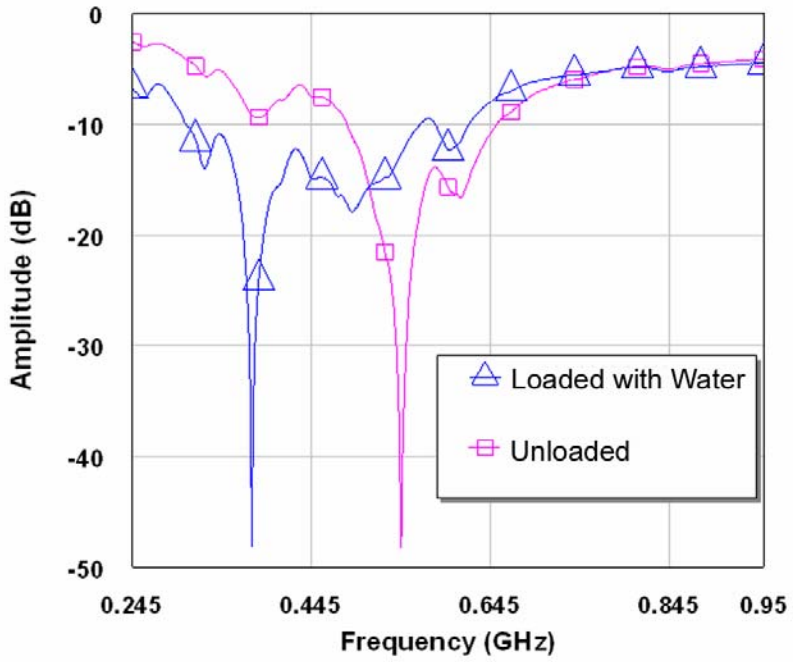

Figure 3.20. Frequency response representation of the S_{11} resonator response before and after water loading.

Not All Resonances are Acoustic

The next step, which should have been attempted before launching into the investigation described in the last section, involved an experiment in which the devices described in the previous section were repeated, but with films deposited at half the thickness. The results of these experiments again revealed results nearly identical to the previous results, in both quality and in frequency of response. As is described by Equation (3.14), acoustic resonance is directly determined by the film thickness. So this latest discovery confirms that not only does the resonance activity have nothing to do with piezoelectric ZnO, but that the resonance has nothing to do with piezoelectricity at all. In other words, the resonance observed through one-port S_{11} analysis was not acoustic in nature. Additional experiments in which the electrode traces were modified or cut in various locations revealed that the resonance was, in fact, purely electromagnetic in nature.

It was obvious at this point that these devices had limited, if any, usefulness as a biosensor. The lessons learned from this detour allowed for a more robust vetting of the resonators that were eventually developed for biosensor applications, however. These include a confirmation that the resonance observed from S_{11} responses are piezoelectric in nature and that the mode of propagation is assessed properly. It is not an entirely uncommon experience to review the published literature and come across reports in which thorough vetting of the observed phenomena were not performed.

From Ta_2O_5 back to ZnO

Given that piezoelectric Ta_2O_5 was not effective, it was decided that the original strategy of implementing a ZnO TSM SMR should be renewed. This time, however, the Ta_2O_5/SiO_2 mirror would not be used as it was thought to be insufficiently capable of reflecting the TSM wave. It was then determined that tungsten (W) and fused silica (SiO_2) might form an appropriate mirror for TSM acoustic waves resonating in a ZnO film, given the mirror predictions shown in Figure 3.2. W could also be deposited using the Unifilm PVD-300 Sputterer. A schematic of the new resonator design is shown in Figure 3.21.

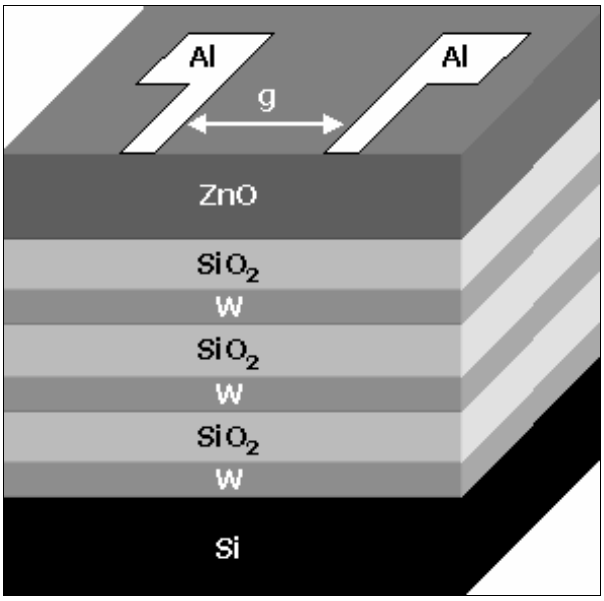

Figure 3.21. Design of ZnO SMR with alternating low acoustic impedance (SiO2) and high acoustic impedance (W) layers form a Bragg reflector.

Device Fabrication

As indicated above, all layers of the SMR were deposited using the Unifilm PVD-300 sputtering system. The deposition parameters for W and SiO_2 are outlined in Table 3.6. Recall that the deposition parameters for ZnO are described in Table 3.2. The thickness of each deposited layer was confirmed using a Leo 1530 thermally-assisted field emission (TFE) scanning electron microscope (SEM), shown in Figure 3.22. Layers understandably varied slightly across the 3" wafer, but were relatively uniform (<10% variation across the wafer). Layer thicknesses are described in Table 3.7, below. Given the material thicknesses measured, the acoustic mirror response was modeled using the model described in Figure 3.1. As can be seen from Figure 3.23, while not as smooth as I would prefer, the mirror should adequately reflect a TSM acoustic wave designed to resonate at 2.0 GHz.

Electrodes were deposited using a CVC E-beam evaporator onto the surface of the ZnO in various configurations consisting of a 30 nm layer of chromium (as a seeding/ adhesion layer) followed by 120 nm of aluminum. The electrodes were formed using a standard photolithography lift-off recipe, described in Appendix C. The various electrode configurations fabricated are shown in Figure 3.24, in which the 'straight-finger' geometries that yielded the best results are highlighted. Note that several dimensions of each electrode configuration were implemented in the mask design. Worth noting at this juncture is that very little difference was observed for operation of the TSM with respect to changes in the electrode width or gap spacing between electrodes. Some

Table 3.6. Unifilm PVD-300 sputtering parameters for the deposition of W and fused silica to form the acoustic mirror.

Parameter	Tungsten (W)	Fused Silica (SiO_2)
Temperature	Ambient	Ambient
Deposition Pressure	5.00 x 10^{-3} Torr	5.02 x 10^{-3} Torr
Argon:Oxygen ratio	100 : 0	98 : 2
Power	121 A @ 135V	270 W @ ~40V
Distance from target to substrate	6”	7.1”
Substrate material	<0 0 1> Si - lyr 1 fused silica - all others	Sputtered <1 1 0> W

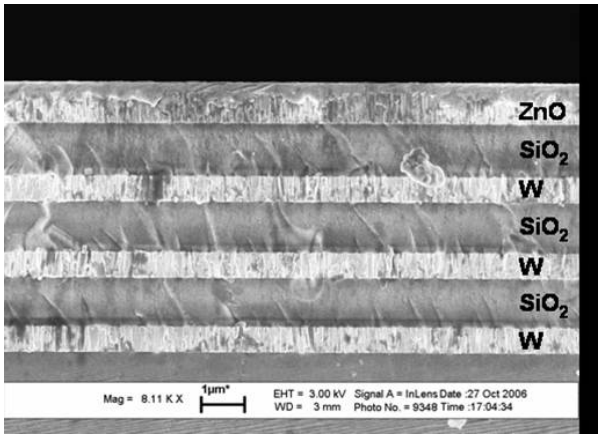

Table 3.7. Material layer thickness as assessed by SEM

Material	Measured Thickness (nm)
Cr/Al Electrode	220
ZnO	710
SiO_2 (L6)	1220
W (L5)	596
SiO_2 (L4)	1206
W (L3)	596
SiO_2 (L2)	1141
W (L1)	596

Figure 3.22. SEM image showing profile of fabricated SMR.

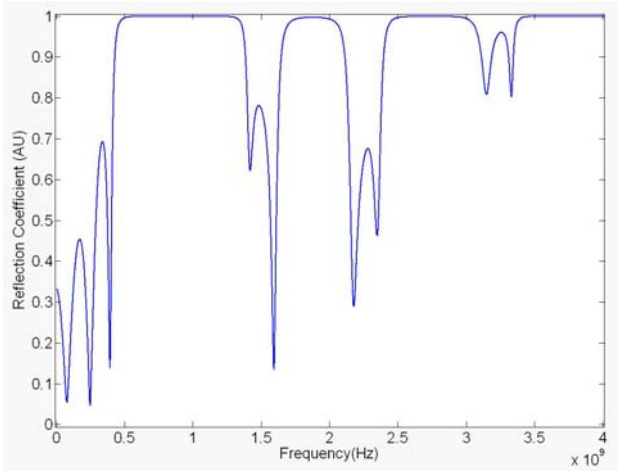

Figure 3.23. Model of mirror response given measured thickness values obtained by SEM for a 6 layer mirror consisting of W and SiO_2.

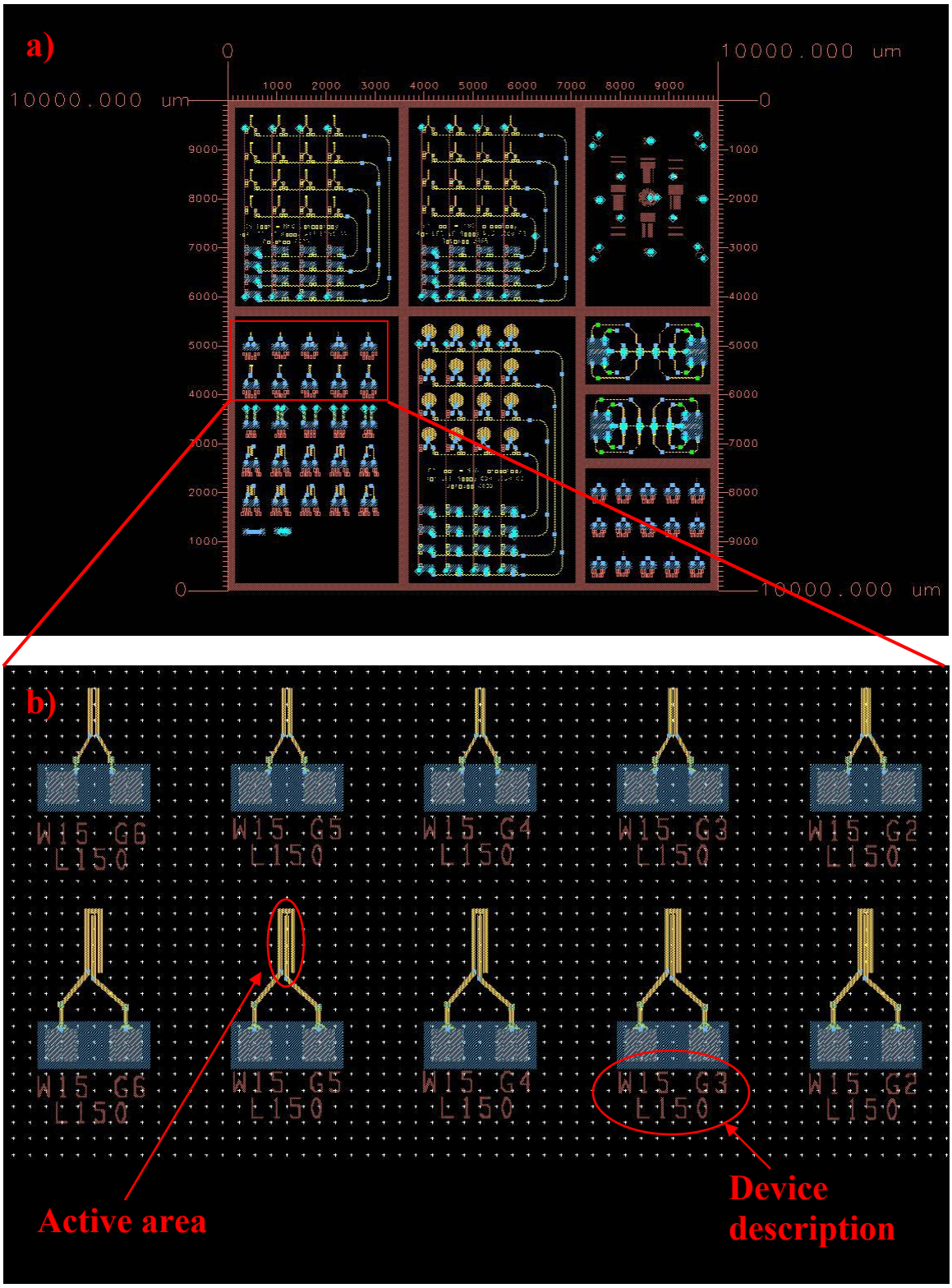

Figure 3.24. a) Electrode geometries fabricated in an effort to achieve LFE of TSM in ZnO with the enlarged image b) showing the 'straight-finger' geometries used to demonstrate high *Q* TSM devices. [Note: W15 – electrode width = 15μm, G3 – electrode gap 3μm, L150-electrode length=150μm]

differences were observed with later experiments with respect to the different geometries, a discussion of which is provided later in this chapter.

Figure 3.25 below demonstrates both a typical impedance response S_{11} response via a Smith chart and the corresponding magnitude of the impedance response converted using Equation (3.15). As described by Rosenbaum with regards to LFE devices, generally the admittance response, Y_{in}, rather than the impedance response, Z_{in}, is considered which takes the form [20]

$$Y_{in} = j\omega C_0 \cdot \left[1 - K^2 \frac{\tan\left(kd/2\right)}{kd/2} \right] \tag{3.15}$$

where C_0 is the clamped capacitance of the parallel electrode configuration, K^2 is the piezoelectric coupling coefficient, k is the wave number described in (3.1), and d is the thickness of the piezoelectric film. This relation led to the development of the Butterworth-Van Dyke (BVD) equivalent circuit model, which is often used to represent

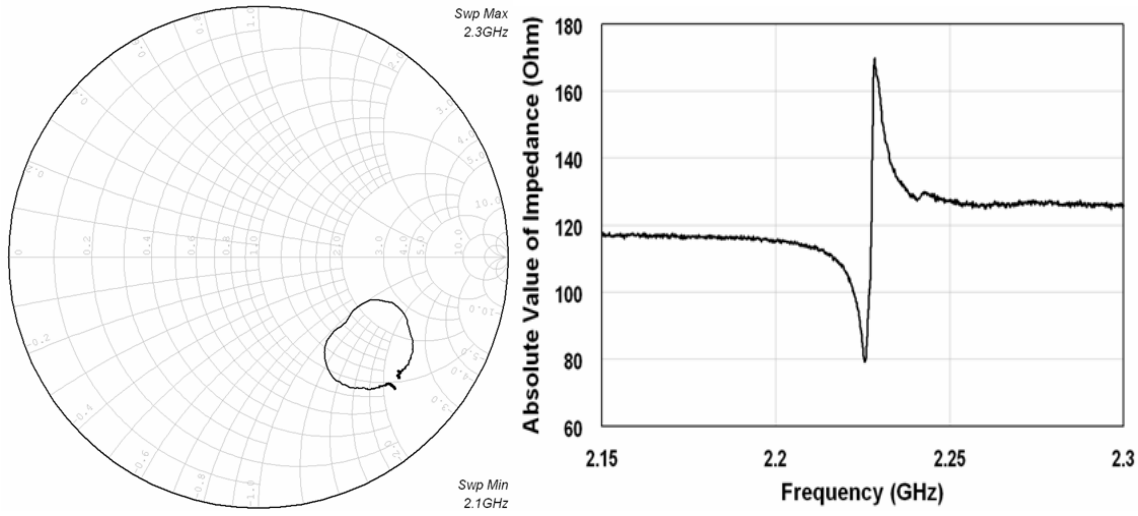

Figure 3.25. Typical magnitude of input impedance (left) and Smith chart of S_{11} response (right) of straight-finger LFE devices. Responses are typical of several thousand resonators fabricated and tested.

the resonance condition at and near resonance. The Ballato equivalent circuit model, briefly discussed earlier in this chapter, provides accuracy outside of the immediate region of resonance, but is a much more complicated circuit with analogs that are not as clearly drawn as with the BVD model. The BVD model, shown in Figure 3.26 [20], is slightly more useful for describing the physical phenomena of piezoelectric resonance and for simple modeling purposes.

From the impedance response described in Figure 3.25(right), note that there are two peaks of interest. The local maximum of the response represents the frequency at which the contributing capacitive and inductive impedances from the BVD model are maximally constructive, and is referred to as the parallel resonance, f_p. Alternatively, the local minimum of the impedance response represents the frequency at which the contributing capacitive and inductive impedances are maximally destructive, and the impedance approaches being purely resistive. This condition is called the series resonance, or f_s. Oscillator circuits can be designed to drive a crystal resonator at either of

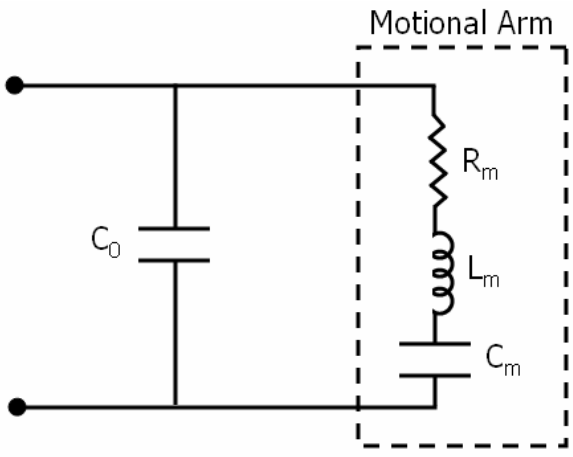

Figure 3.26. Butterworth-Van Dyke equivalent circuit model for piezoelectric resonance. The 'Motional Arm' represents the effective acoustic impedance near the resonance condition.

these conditions, but the parallel resonance is the most common, and is the one that I will focus on for this research.

It should be noted at this juncture that Q and K^2 are common metrics for assessing resonator performance. It is possible to estimate theoretical values for Q from material properties using the following formulae: [20]

$$Q = \frac{v_a^2 \rho}{\omega_r \eta} \tag{3.17}$$

where ω_r is the resonance frequency, and η is the relevant material viscosity, or sometimes as [55]

$$Q = \frac{c}{\omega_r \eta} \quad . \tag{3.18}$$

It is similarly possible to estimate K^2 by [20]

$$K^2 = \frac{e^2}{c^E \varepsilon^S} \tag{3.19}$$

Obtaining single-crystal bulk values for ZnO from Auld [55], it is thereby theoretically possible to obtain K^2 values as high as 7%. Due to the fact that the viscosity tensor for ZnO has not been determined, it is not possible to obtain a theoretical Q value for these resonators at this juncture.

A summary of the S_{11} results for the 'straight-finger' devices, depicted in Figure 3.24.b, are provided in Table 3.7. The average unloaded Q of the parallel resonance, Q_p, was approximately 340 with a K^2 of approximately 0.4% (n = 30). The calculations used to assess Q and K^2 empirically from the S_{11} response are as follows: [20]

$$Q_p = \left(\frac{f_p}{2} \right) \frac{d\angle Z}{df_p} \tag{3.20}$$

$$K^2 = \left(\frac{\pi}{2} \right)^2 \frac{f_p - f_s}{f_p} \tag{3.21}$$

where f_p is the parallel resonance frequency and $\angle Z$ is the phase of the impedance response of the resonator. Note that the Q_s of the series resonance can be similarly calculated replacing f_p with f_s in Equation (3.20). Note that Q is also commonly estimated by taking a FWHM measurement from the relevant peak from the magnitude of the impedance response, as is done by the HP8753C Network Analyzer.

Immediately noticeable from the results summarized in Table 3.7 is the relatively low K^2 value, given the potential of 7% calculated earlier. From Equation (3.21), we find that K^2 is approximated by the frequency separation of the series resonance and the parallel resonance peaks from the magnitude of the input impedance response. Given the relationship described, the greater the frequency separation between f_s and f_p, the greater K^2. Without a corresponding increase in the magnitude of the f_p peak, however, then there must be a decrease in resonator Q due to the expansion of the width of the peak at half-maximum caused by the wider frequency spread.

Table 3.8. Summary of LFE of TSM in ZnO SMR using first successful device design (Figure 3.10). [n=30]

Parameter	Average [Std Err]	Maximum
f_p	2.213 GHz [± 1.8 MHz]	2.227 GHz
Q_p	342 [± 19.9]	553
K^2	0.44 % [± 0.03 %]	0.88 %

As a comparison, the QCM is widely attributed with having extremely high resonator Q (>60,000 at 10 MHz [109]), yet only exhibits k_t^2 of 0.5%. Note that for TE devices the coupling coefficient is represented as k_t^2, whereas LFE devices are described using K^2, as discussed by Rosenbaum. The two are related by [20]

$$k_t^2 = \frac{K^2}{K^2 + 1}. \tag{3.21}$$

Given that the operation of an acoustic biosensor involves the ability to resolve shifts in the resonance condition in response to a perturbation of the boundary conditions at one surface, it is felt that particular focus must be concentrated on optimization of resonator Q at the expense of K^2 in order to develop the most effective device for biosensor applications. Anecdotal evidence of superiority of Q as a key parameter for sensor application is the extensive and successful use of the QCMs which, as stated, exhibits high Q and very low k_t^2.

Confirmation of TSM

Before optimization of the device design can be undertaken, two central points must be confirmed regarding the device operation. As demonstrated by the investigation of Ta_2O_5, it is easy to misinterpret the collected results and make erroneous conclusions about the observed phenomena. In order to confirm that the devices were in fact operating the TSM acoustic wave in the ZnO film, a series of experiments were performed.

The first issue to be resolved is that the device exhibits changes in frequency in response to changing piezoelectric film thickness, confirming the resonance as an acoustic phenomenon. Further that the extracted acoustic wave velocity corresponds with the predicted theoretical values derived for single-crystal bulk ZnO described previously. Films were deposited in three different thicknesses onto the same mirror, of 660 nm, 710 nm, and 790 nm. The thicknesses were confirmed using the Leo 1530 TFE-SEM and the results are summarized in Table 3.8. As the data confirms, the observed resonance is indeed an acoustic wave and the wave velocity is very close to the predicted value of 2,841 m/s. Furthermore, the acoustic velocities extracted agree closely with the results of comparable studies [19, 51-53].

The second issue that must be confirmed is that the wave demonstrates shear particle displacement to the surface. Without access to a tool for physically imaging this parameter, a simple water drop test was implemented to demonstrate this. If the acoustic wave consisted of any longitudinal component, this should readily be transferred into the liquid medium as a compression wave. While the shear wave does exhibit some penetration into the liquid medium, as described by Kanazawa and Gordon [27], the majority of the acoustic energy should reflect back into the piezoelectric crystal. Figure 3.27 represents a typical result of depositing 20 μL of deionized water (DI H_2O) onto the

Table 3.9. Summary of observations of TSM resonance due to different ZnO film thicknesses deposited onto the same acoustic mirror.

Measured ZnO Thickness (nm)	f_o **(GHz)**	**Extracted Acoustic Velocity (m/s)**
790	2.0	3,160
710	2.2	3,130
660	2.35	3,100

device surface, as observed through the S_{11} response. Some deterioration of the resonance was observed resulting in lowering of the Q factor, which is due to the slight energy absorption into the liquid described above. Worth noting is that a more dramatic effect is observed when DI H_2O is deposited onto the surface of a QCM. Figure 3.28 provides a demonstration of that effect for comparison purposes. Note that both resonators exhibit a negative frequency shift upon introduction of water in addition to the spreading and loss of some of the acoustic energy. The frequency shift represents a mass-loading event at the surface. With significantly larger surface area and more water deposited on the surface, the QCM (f_p = ~10 MHz) only reflected a 2.5 kHz frequency shift, while the ZnO SMR (f_p = ~2.0 GHz) shifted by 11.3 MHz. This is consistent with the argument made in Chapter 2 claiming the sensitivity of the sensor to be directly proportional to a power of the resonant frequency.

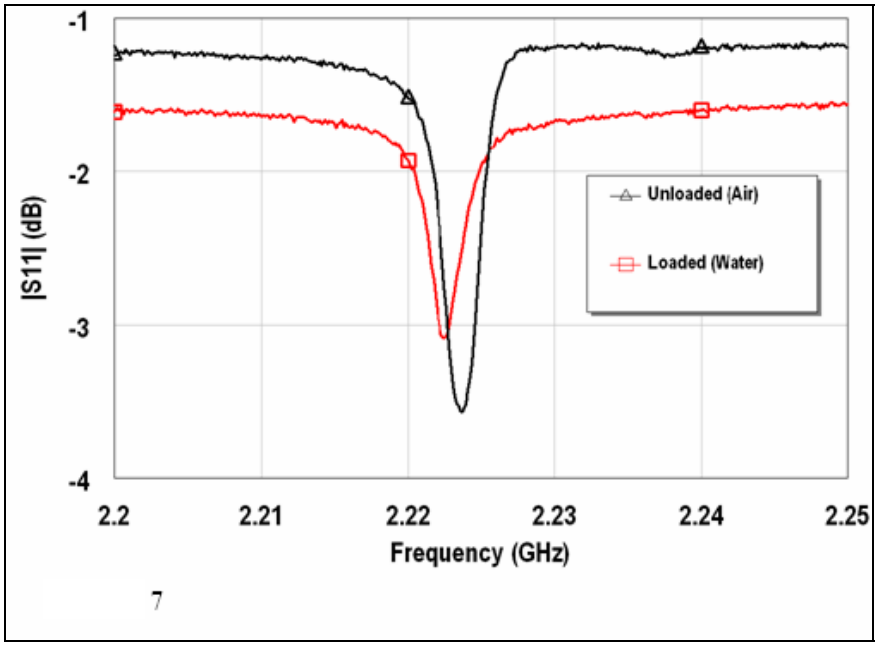

Figure 3.27. Frequency shift observed in S_{11} measurement in response to loading the ZnO SMR surface with deionized H_2O.

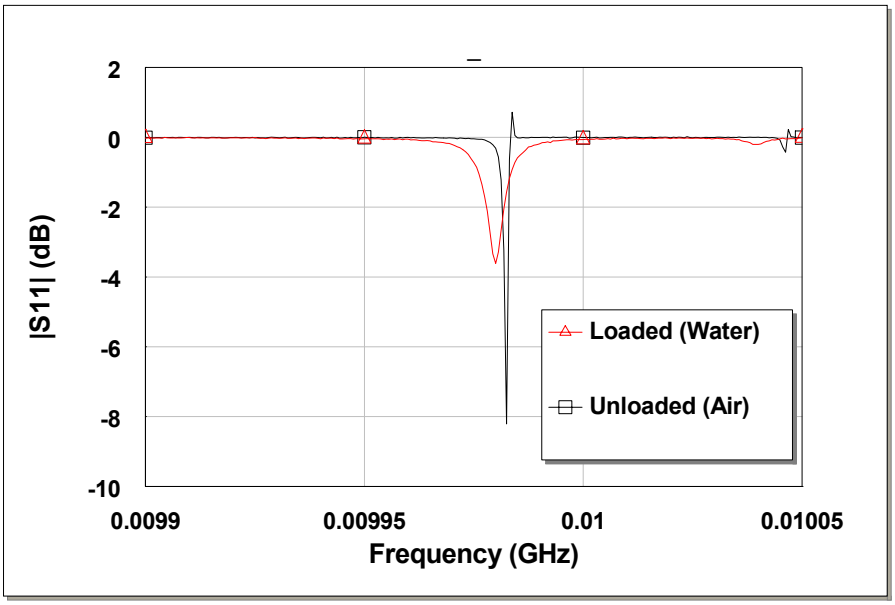

Figure 3.28. Frequency shift observed in S_{11} measurement in response to loading the QCM surface with deionized H_2O

It must be mentioned that several resonance peaks were observed from the broader band S_{11} responses. Two of the stronger resonance peaks were observed at~6,000 m/s and also at ~4,800 m/s. The 4,800 m/s peak was of particular interest as it dampened very little upon presentation of DI H_2O at the device surface. The peak was of significant interest because of its higher Q, yielding high potential for biosensor applications. It is strongly suggested that this resonance be further investigated for such an application. Table 3.7 summarizes the observations of this resonance activity.

Table 3.10. Summary of LFE of 4,800 m/s resonance in ZnO SMR using device design shown in Figure 3.10. [n=29]

Parameter	Average [Std Err]	Maximum
f_p	3.424 GHz [± 6.1 MHz]	3.467 GHz
Q_p	562[± 30.55]	744
K^2	0.23 % [± 0.05 %]	0.27 %

Resonator Testing

Due to the difficulty of fabrication and various issues regarding spurious resonance activity, it was decided that a new electrode configuration was required that balanced the electromagnetic field incident on the piezoelectric film. There was also reason to believe that a superior resonator could be achieved by fabricating a device in which the gap size between electrodes was significantly larger than the piezoelectric film thickness, as described by Rosenbaum as preferable for LFE [20]. The new design was accomplished by implementing a more symmetric electrode design that surrounded the signal electrode with ground electrodes, rather than establishing the ground on a single side as seen in Figure 3.24. The two electrode geometries were then implemented with various electrode widths and gap sizes for each configuration.

A total of eight different electrode configurations were tested using the two electrode shapes depicted in Figure 3.29. Devices were evaluated based on quality factor, Q, and coupling coefficient, K^2, as calculated from the S_{11} response of each device. Results obtained from ANOVA demonstrate that a statistically significant gap ($p < 0.01$) emerges between the performance of the circular shaped devices (Figure 3.28, left) and the straight electrode devices (Figure 3.28, right) when analyzing their K^2 and Q results. It is evident that the average Q is higher for the straight electrode configuration while the effective K^2 is lower. One possible explanation for this is that the circular electrode configuration has a larger surface area over which excitation of the crystal occurs.

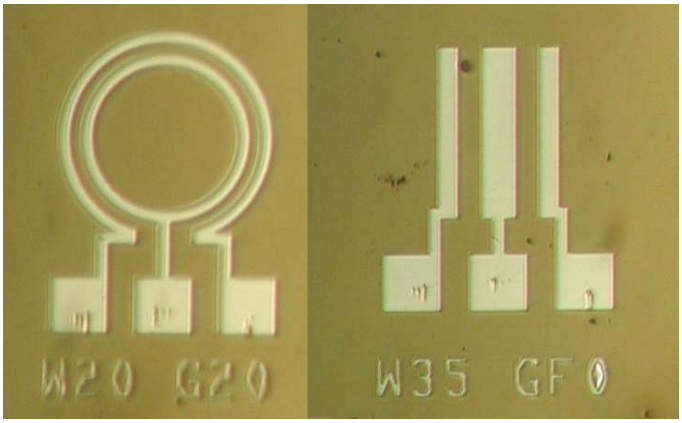

Figure 3.29. New electrode design exhibiting greater symmetry and larger electode gap widths. [Note: W20 - electrode width = 20mm; GF0 - electrode gap = 40 mm]

Therefore, the coupling of the electric field to the crystal over grain boundaries and crystal non-uniformities is more efficient overall while the added mass of the larger electrodes acts to reduce the *Q*. These results are summarized in Table 3.8 and Figure 3.30.

As indicated by the strong correlation between devices G & H, it is readily apparent from the data that the electrode widths fabricated had no statistically significant impact on the device performance as assessed by *Q* and K^2. One would hypothesize that greater distribution of the electric field from a *constant power* source to the piezoelectric crystal would result in a more distributed and efficient coupling of electrical energy into acoustic wave energy. Since *Q* is a ratio of energy conserved to energy dissipated per cycle, it would seem that the *Q* factor should improve as a reflection of this. It was surprising that the size of the gap between electrodes had no clear functional relationship with the device performance. Gap size does have some impact, however, as can be seen from device D in Table 3.8. Compared with the other straight electrode configurations, the 10 μm gap exhibits a significantly lower *Q* and higher K^2, on average. It appears that beyond a particular threshold between 10 μm and 20 μm between straight electrodes, there was a

Table 3.11. Assessment of device performance of tested resonators from analysis of collected S_{11} parameters.

Device	Shape	Electrode width (μm)	Electrode Gap (μm)	# Tested	Average *Q*	Average K^2
A	Circular	20	10	92	198	0.86%
B	Circular	20	20	72	195	0.87%
C	Circular	20	40	70	192	0.86%
D	Straight	20	10	69	198	0.84%
E	Straight	35	20	74	217	0.78%
F	Straight	35	40	98	206	0.77%
G	Straight	20	50	25	220	0.74%
H	Straight	35	50	44	221	0.73%

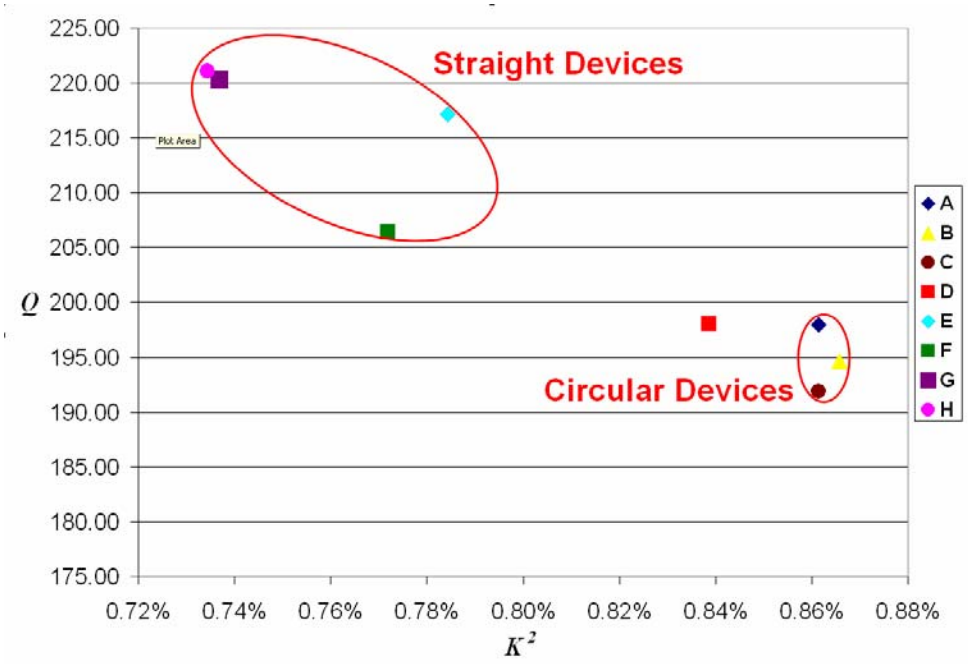

Figure 3.30. Comparison of various electrode configurations using *Q* and K^2. Note, results represent the assessment of over 500 devices fabricated and tested.

notable improvement in *Q*. No clear pattern emerges beyond this, however, for the ranges tested.

Having determined that the straight electrode configuration yielded higher *Q* devices, which has been identified as the desired parameter, 8-element arrays of these devices were fabricated in order to verify that the resonator design displayed in Figure 3.28 (left) performed as well in the array configuration as individual devices. That is to say, to

confirm that the array structure did not bear any beneficial nor detrimental effects on the resonator's performance. Sampling more than 150 arrayed devices similar to those seen in Figure 3.31 showed that there in fact was a statistically significant difference in device performance. Note that tests were performed on both arrayed circular electrodes as well as straight finger electrodes. As in the isolated individual devices, the Q of the straight finger devices outperformed the circular devices. There was a significant deterioration in performance, however, from incorporation into array configurations. All of these arrays are demonstrated in Appendix B, and are similar to the array demonstrated in Figure 3.31, below. Results are summarized in Table 3.9. A 30% decrease in Q and a 15% decrease in K^2 was observed for straight finger devices with a 20 μm gap fabricated in the array configuration versus the isolated configuration. For devices fabricated into 8-element arrays with a 50 μm gap, again a decrease of 28% was observed in Q but only a 8% decrease in K^2. Note that the trade-off between Q and K^2 is still evident in these devices. One explanation for the decrease in performance is the addition of a significant amount of metal surrounding the active devices for bonding pads and ground-bus connections. The added mass from the electrodes provide a lossy material at the surface boundary which can act to scatter the acoustic energy. In addition, the different electrode configuration itself is likely to have altered the electric field from the isolated configuration, contributing to a change in the resonator performance. I felt that the results

Table 3.12. Assessment of arrayed device performance of tested resonators from analysis of S_{11} response.

Array	Electrode Shape	Electrode width (μm)	Electrode Gap (μm)	# Tested	Average Q	Average K^2
1	Circular	20	10	46	133	0.83%
2	Circular	20	40	32	121	0.83%
3	Straight	35	20	63	150	0.66%
4	Straight	35	50	23	159	0.67%

were still good enough to proceed, however, with sensor testing.

Biosensor Compatibility

As this is a novel resonator design implementation, it is important to characterize the general stability of the TSM acoustic wave in the thin film ZnO SMR. First, it was important to confirm that the resonance itself is stable and does not vary over time. An experiment was conducted holding the resonator fixed at 25ºC while constantly driving the resonator at 1 mW using a HP 8753C Network Analyzer. Devices were probed using Cascade Microtech ACP40 GSG-150 probes. It was found that the resonator was more than suitably stable, exhibiting a 0.01% shift (32 kHz) after 3 hours of constant resonance. The results are depicted in Figure 3.32.

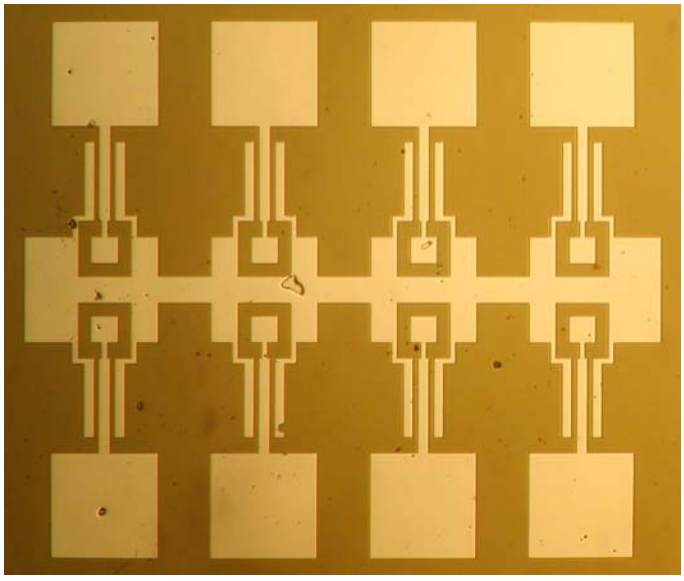

Figure 3.31. Digital image of fabricated 8-device array. Device is designed for probing with Cascade Microtech ACP40 probes and with pads large enough for subsequent wire bonding. (occupies 2.0 mm x 2.4 mm space)

A second parameter commonly investigated relates to the resonators susceptibility to varying temperatures. The parameter often investigated regarding this susceptibility is the temperature coefficient of resonant frequency (TCF), which is defined as

$$TC(f_x) = \frac{df_x}{dT} \cdot \frac{1}{f_{x,RT}} \tag{3.22}$$

where T is the temperature, f_x is the relevant resonant frequency and RT represents room temperature (25°C). The temperature was varied from 25°C up to 175°C in increments of 25°C and the resonant frequency was measured after the system was allowed to stabilize at each temperature point for at least 10 minutes. The results yielded an empirically derived TCF for the series and parallel resonance of +24.6 ppm/°C and +25.6 ppm/°C,

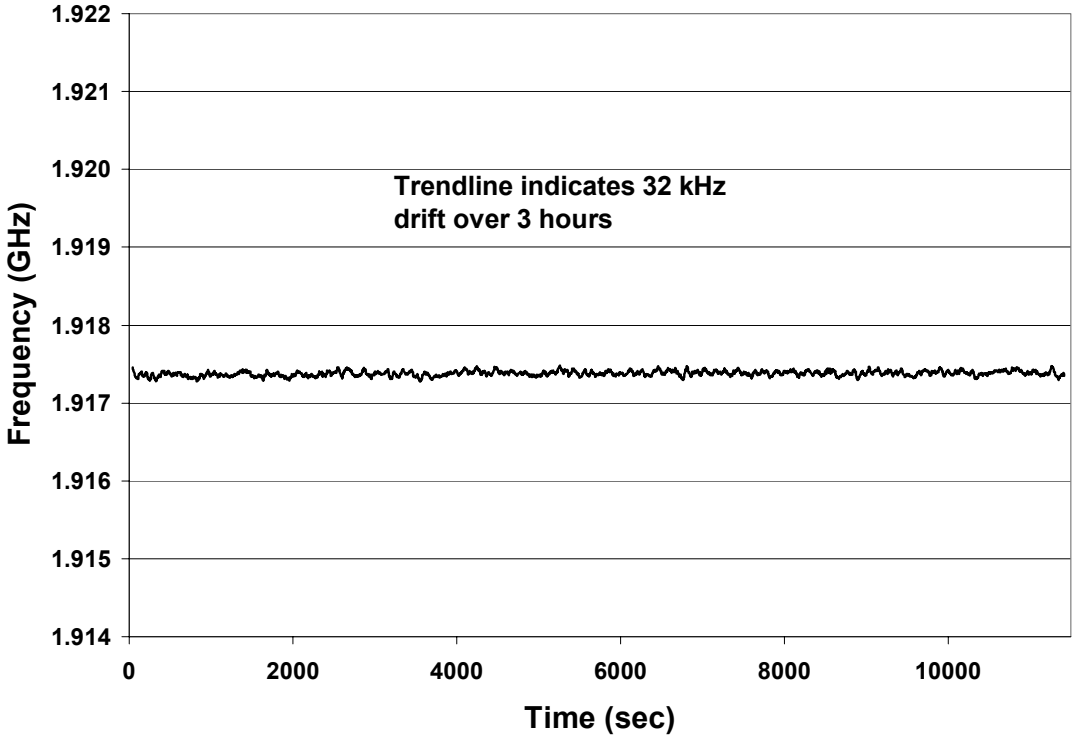

Figure 3.32. Parallel resonance frequency plotted against time demonstrating stability of resonance over a three hour time period, at a constant 25ºC.

respectively. Note that these are considered relatively low TCF values, suggesting these devices are appropriate for sensor applications. These results are demonstrated in Figure 3.33. This experiment was conducted 3 times with identical results.

The susceptibility of device Q and K^2 was also investigated to confirm no degradation in the quality of the resonance itself with increasing temperature. It was found that the K^2 remained very stable over the temperature range tested, varying by only 0.1% over the 155°C range. The Q drift of the resonator was slightly more significant, varying by roughly 42% over the 155°C temperature range. For application in a bench-top biosensor application in which testing is likely to occur at or near room temperature, the Q remained stable enough to consider negligible exhibiting an average shift of 0.28/°C

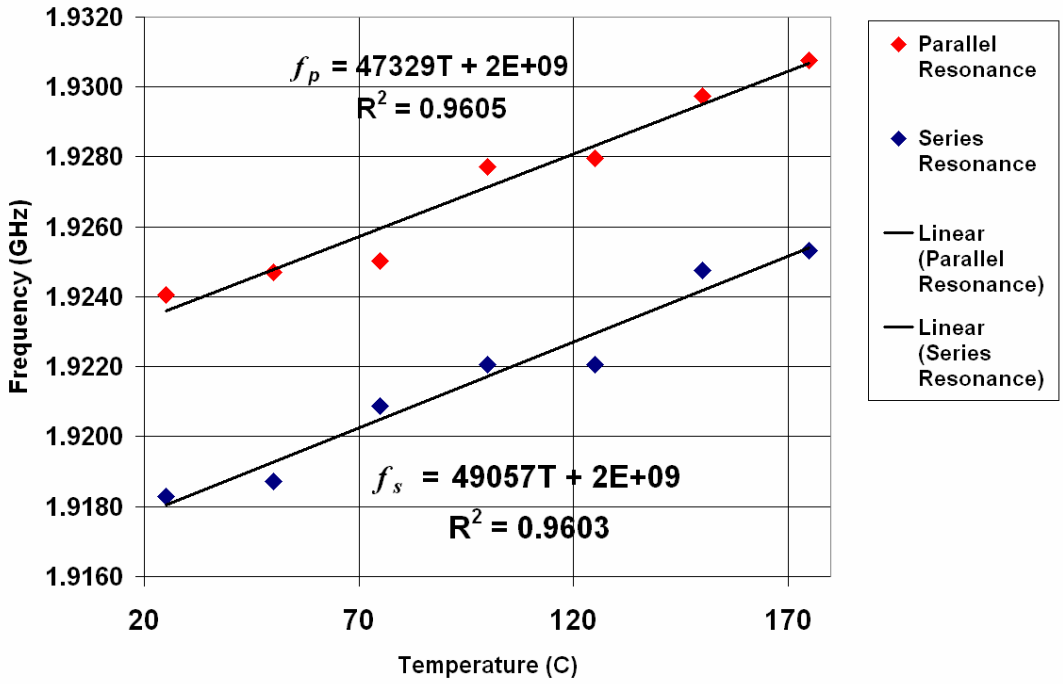

Figure 3.33. Frequency drift of parallel and series resonance frequencies with increasing temperature.

(<0.2% per degree). The results for the temperature stability of Q and K^2 are summarized in Figure 3.34 and 3.35, respectively.

When designing sensors for use with physiological samples, it is important to assess the sensor's performance under varying sample conductivity conditions. Hu *et al.* characterized the effects of sample conductivity on QCMs employing LFE rather than the typical TE for biosensor applications [110]. I determined that a similar investigation of the characteristics of the TSM in ZnO was sufficient to investigate this.

Considering the goal of employing these resonators in biosensor applications with biological fluid samples, the resonators were tested over a range of sample conductivities. Biological fluids are filled with electrolytes, which imbue the fluid they are in with conductive properties. It is common in the literature to see 0.9% NaCl in DI H_2O described as an equivalent salinity to blood. Therefore, I loaded the surface with 0.0% to 0.9% wt/vol of NaCl in DI H_2O. Saline solutions were prepared using 99.5% NaCl (Sigma) and HPLC-grade deionized H_2O (Burdick & Jackson) and mixed for at least 30 seconds on a mini vortexer (VWR Scientific Products). The devices were tested using the equipment described earlier in this chapter. In addition, a laptop computer running a custom LABVIEW program for tracking the resonance frequency of the device under test was employed [111]. The device arrays were exposed to the saline solutions by hand pipetting ~1 μl directly onto the resonator array surface while being probed.

Results indicate that the magnitude of resonator frequency shift varied little in relation to loading with pure water alone, as indicated in Figure 3.36. As can be seen, the percentage of frequency shift with increasing sample conductivity was less significant than the increasing noise level. These devices are not ultra high Q, as QCM devices are,

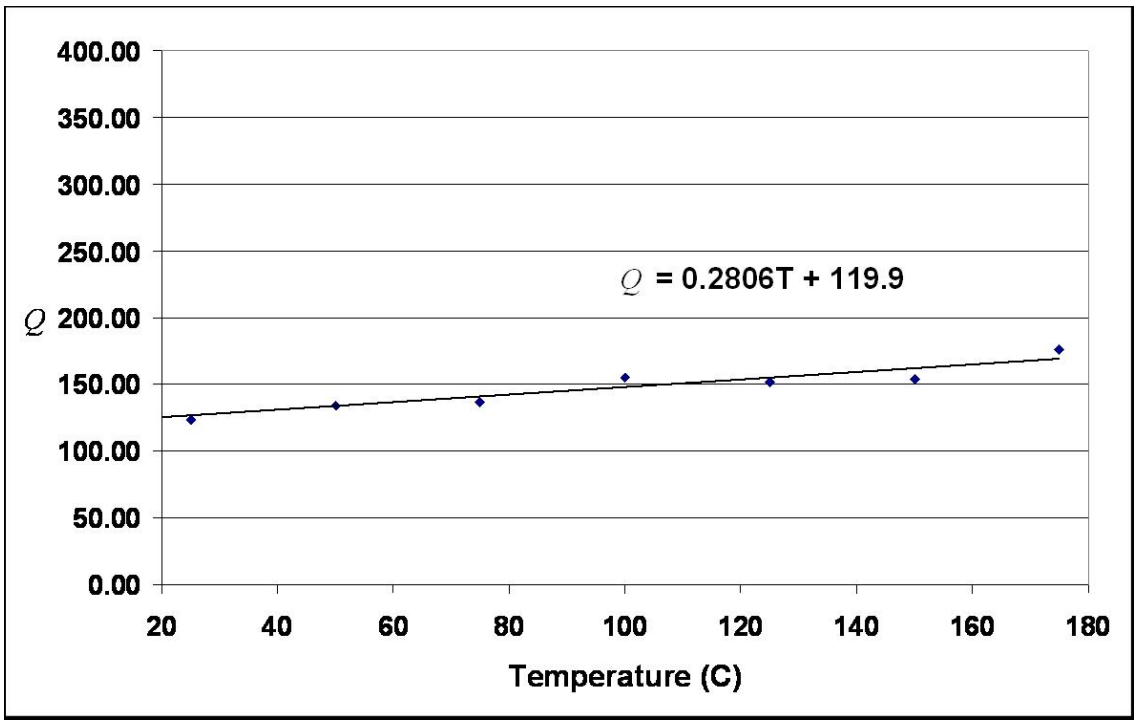

Figure 3.34. Susceptibility of resonator Q to changes in operating temperature from 25°C to 175°C.

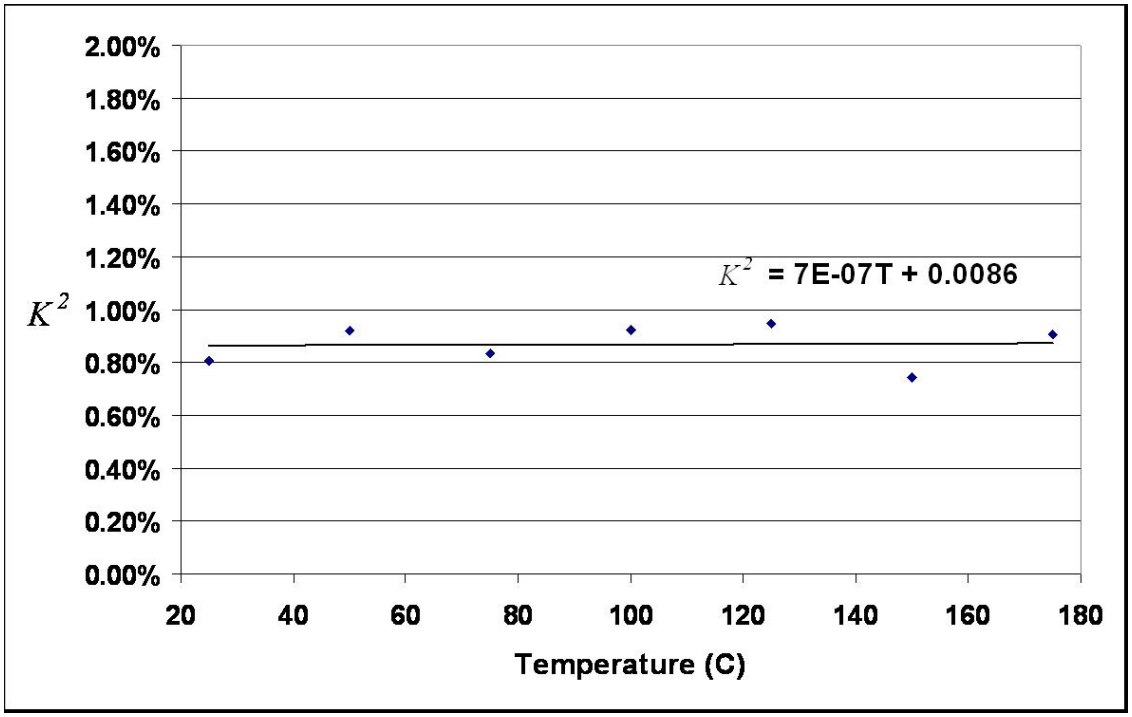

Figure 3.35. Susceptibility of resonator K^2 to changes in operating temperature from 25°C to 175°C

so the resonance peak is still slightly broad. Incidental high-frequency fluctuations in the reflection parameters will cause the parallel resonance monitor to register a shift if frequency, though the broad peak does not actually shift. The error bars in Figure 3.36 indicate the measured variance due to these incidental fluctuations. A further indicator of this can be seen in Figure 3.37, which demonstrates the results of a typical experiment when a 0.9% saline sample is deposited on the device surface then subsequently washed with DI H_2O. Figure 3.38 is provided as a comparison of the relatively lower levels of noise observed with DI H_2O alone.

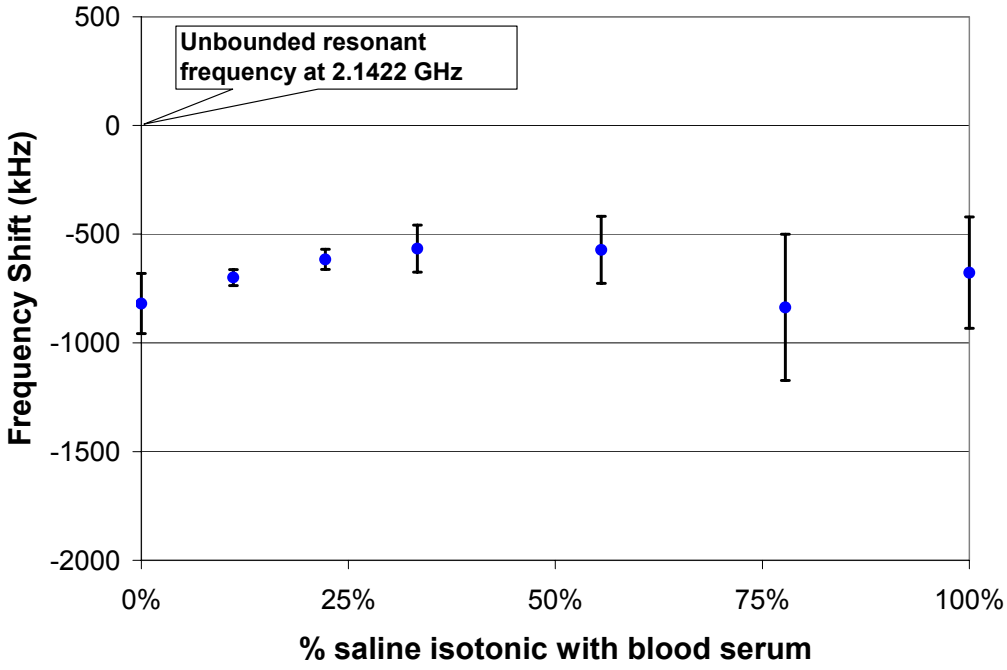

Figure 3.36. Typical experiment demonstrating change in parallel resonance frequency with increasing saline concentration on the surface of the resonator.

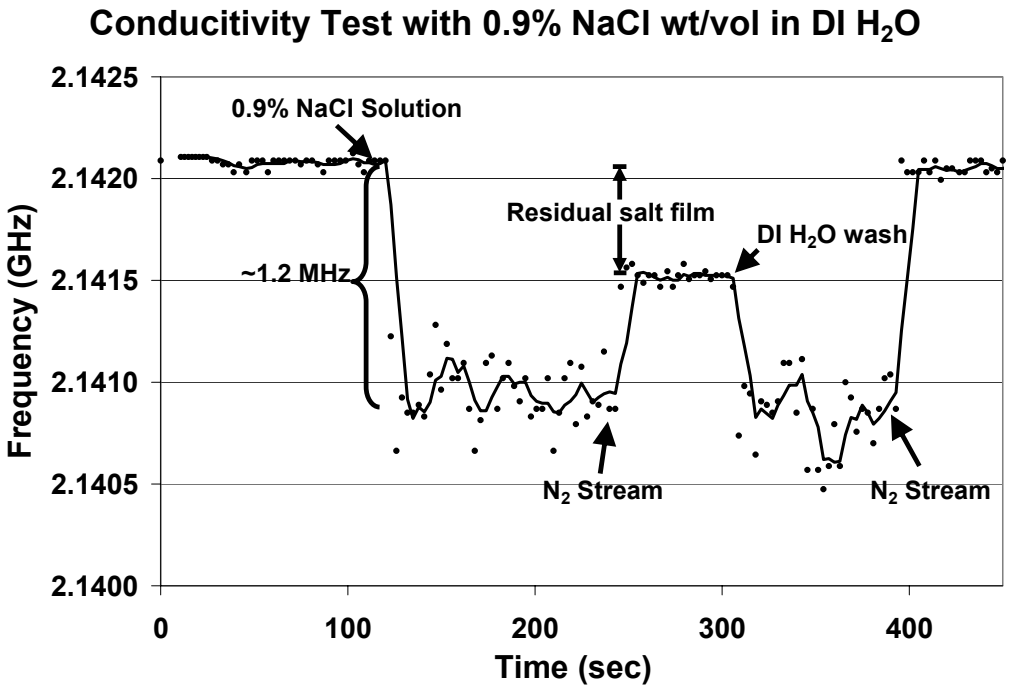

Figure 3.37. Demonstration of a typical conductivity experiment with 0.9% NaCl in DI H_2O.

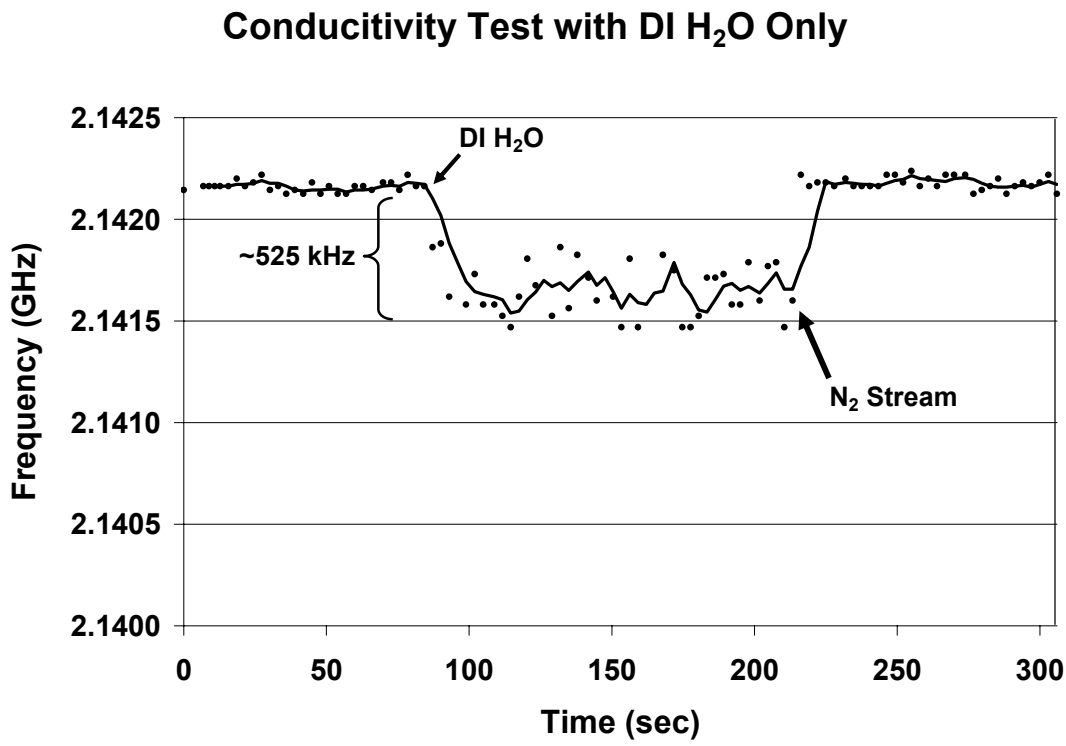

Figure 3.38. Demonstration of a typical conductivity experiment with 0.0% NaCl in DI H_2O.

CHAPTER 4

SENSOR FUNCTIONALIZATION

In order to functionalize the resonators developed through Chapter 3 for biosensor applications, it is necessary to create conditions at the surface of the piezoelectric layer that execute a molecular recognition capability for a specific target. This often requires a surface chemistry protocol involving the immobilization of an appropriate capture agent at the surface of the device that in turn has a high degree of specificity for a single target molecule. In this chapter I will discuss the selection of appropriate capture agents and the development of an appropriate protocol for immobilization of those capture molecules on the surface of my resonators. The use of a reference sensor as a control is absolutely critical for this protocol. Reference sensors functionalized with capture molecules specific to a target absent from the test media help guarantee that any frequency shift of the test sensor is due to binding of the intended target and not to non-specific binding or other changes in the surface. This argument can be made because both the test sensor and the reference sensor have received identical functionalization treatments with similar capture molecules and exposed to the same test medium. Any difference in behavior observed in the two sensors can be attributed to binding of the test sensor to target molecules in the liquid sample under test.

Recall that acoustic wave biosensors function by detecting changes in the path over which the propagating wave travels (see Chapter 3). As with most types of biosensors, the ability to obtain repeatable results from an acoustic sensor, especially one with potential for extremely high sensitivity, is related to the repeatability of the prepared

surface layer, or biolayer, which executes the function of molecular recognition. A requirement for any high precision biosensor is that the output signal, or device response, be repeatable given multiple identical samples and on different sensor elements prepared in the same manner. Therefore controlled, reproducible immobilization of appropriate capture molecules to functionalize the device is necessary to preclude device to device signal variations. In assessing the quality of the various biolayer protocols attempted in this research, therefore, it is critical to qualify both the uniformity and repeatability of the biolayer.

Capture Molecule Selection

There are a myriad of capture agents that have been employed to functionalize transducers of various types into biosensors since the first biosensor was developed by Updike and Hicks in 1967 [112]. These include oligonucleotides, receptor proteins, enzymes, antibodies, synthesized polypeptides and lectins [113]. For the purposes of our specific applications, recall that we desire keeping interactions close to the surface so as to maximize the device sensitivity. For that reason, there is no need to consider capture agents larger than these. With the exception of glucose sensors, the most commonly employed capture agents are antibodies (Ab) [113]. To an increasing degree, however, biosensor developers are looking more towards oligonucleotide structures for a number of reasons, which are discussed later in this chapter. Recalling the goals of this biosensor research, it is a high priority to establish a biosensor with high specificity and selectivity. Of the capture agents reviewed for this research, antibodies and aptamers top the list for

high affinity for their target analytes. A secondary priority is the ease of fabrication and potentially low cost of production. Given these criteria, I will consider both options and how well they would work for our application.

Antibodies

As mentioned, antibodies are one of the most commonly employed capture agents for biosensor applications. Ab's, or immunoglobulins (Ig's), are produced by all vertebrates as an essential component of their immune system. These molecules exhibit specific molecular recognition capability, determined through a complex evolutionary refinement process [12]. They are produced by the B cells of all placental animals in five isoforms, including the pentamer IgM, the dimer IgA, and the monomers IgD, IgE, and IgG. Among these, the IgG molecule is most widely used because it is by far the most abundantly produced and exhibits the greatest stability (generally lives 4 to 10 times longer than the other isoforms in plasma) [12].

The IgG molecule is a 150 kDa protein made up of two "heavy chain" segments (446 amino acids in length) and two "light chain" segments (214 amino acids in length) and comes in four subclasses. The four subclasses are categorized based on minor structural differences of the heavy chain, mostly accounting for the location of Cystine residues. The general monomer structure is demonstrated in Figure 4.1 below. The binding domain is located at the two amino-terminals of the structure and exhibit excellent specificity and affinity for their targets. The binding mechanism is controlled by both the variable amino acid residues that make up the binding pocket and the 'hinging' action of the di-sulfide bonds holding the heavy and light chains together. Taken together, IgG_1 molecules (the most abundant IgG subclass) have reported extraordinary affinity ($K_a > 10^{10}$ M^{-1}) [114].

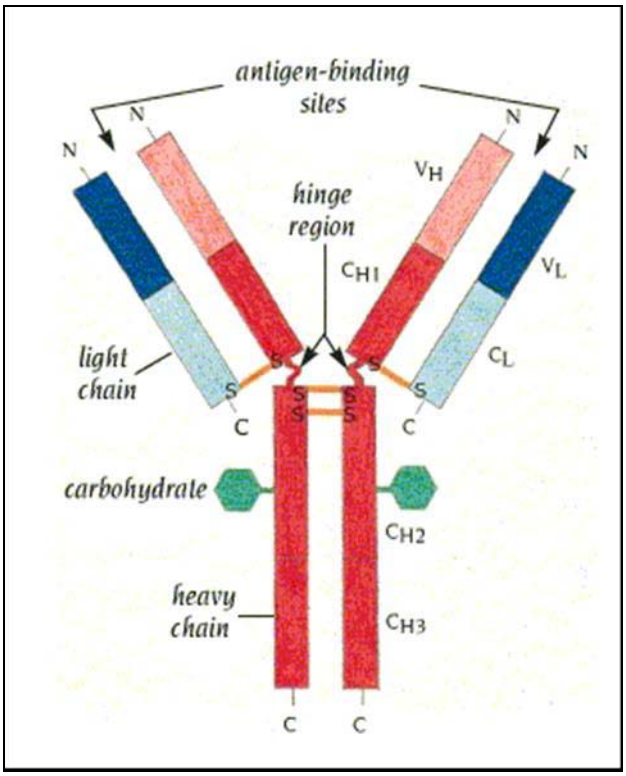

Figure 4.1. Secondary structure of the IgG monomer with individual regions identified [115].

Another attractive component of using IgG antibodies is the wide array of surface chemistry protocols for immobilizing the molecules in a functional manner on various surfaces. Recall the binding domain is located at the amino-terminals of the protein as indicated in Figure 4.1. For use as a capture agent attached to the surface of a transducer, the molecule must therefore be immobilized nearer the carboxyl-terminal (the region described as the F_c portion of the Ab, or crystallizable fragment) in order to maintain functionality as a capture agent. It is further desirable to achieve a covalent (or stronger) bond between the antibody and the device surface, so as to achieve a more generally stable sensor configuration. All protocols that I have encountered to date achieve this with the IgG molecule by covalent binding of an acid head group to an available amine terminated residue on the antibody. The F_c portion of the antibody exhibits a relatively

rich population of available lysine residues, as indicated by the highlighted regions in Figure 4.2 below [116]. There are 18 Lysine residues and 5 Arginine residues in each of the two 220 amino acid length segments of the heavy chain within the F_c portion of the antibody.

Most of the work regarding covalently binding IgG molecules to *oxide* surfaces in an effort to functionalize them has focused on the use of quartz (SiO_2). Hydroxyl groups at the surface of an oxide provide sites for reaction with cross-linking molecules to form covalent bonds [117]. One of the more common methods for functionalizing SiO_2 surfaces involves the use of organosilanes. Success with immobilizing antibodies on SiO_2

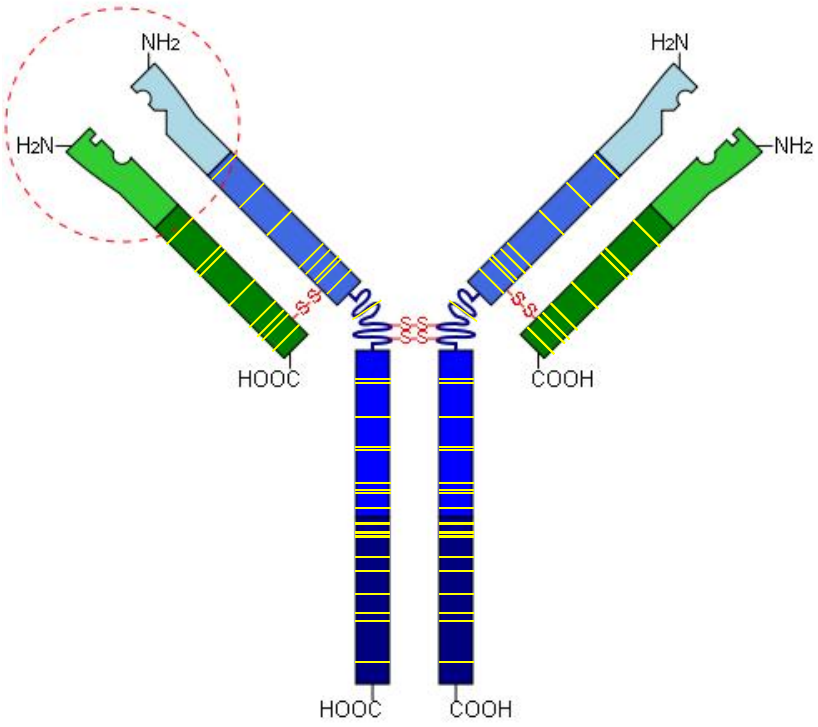

Figure 4.2. IgG molecule with approximate location of Lysine residue highlighted.

surfaces has been shown using amine- and thiol-terminal silanes such as 3-mercaptopropyl-trimethoxy-silane (MTS) with a variety of heterobifunctional crosslinkers, such as N-γ- maleimido-butyryloxy succinimide ester (GMBS) [117, 118]. Other work in modifying SiO_2 surfaces has focused on forming self-assembled monolayers (SAMs) using epoxysilanes [119, 120]. The great advantage of using an epoxysilane such as (3-glycidoxypropyl) trimethoxy-silane (GPS) for forming SAMs on oxide surfaces is that it eliminates the need for a secondary crosslinker between the silane molecule and target antibodies. The exposed epoxy groups react readily with amine groups. Given that hydroxyl groups are also available at the surface of planar ZnO, it is thought that some of these techniques may be employed.

Despite the amount of research that has been performed on various oxides, including SiO_2, there have actually been relatively few studies involving the functionalization of planar ZnO surfaces. One study reports the use of 3-aminopropyl-triethoxy-silane (APS), which is an amine-terminated silane, to covalently bind Interleukin-6 to the surface of device-quality ZnO films [121]. APS is used as the primary crosslinker, followed by glutaraldehyde as a secondary homobifunctional crosslinker to bind the protein, Interleukin-6. A major drawback with the use of glutaraldehyde, however, is that it binds to other gluteraldehyde and is known to form large polymer conglomerates which may bind many residues and form large multiprotein complexes [117]. My own early attempts at functionalizing planar ZnO using APS and glutaraldehyde yielded surfaces that indicated this was in fact occurring in my own preliminary trials. This study does demonstrate, however, that silane chemistries can be applied to the surface of ZnO.

There are many disadvantages to using antibodies for capture agent applications, of course. For one, the production of monoclonal antibodies for sensor and immunoassay applications is generally achieved through the Hybridoma Technique. This protocol involves the generation of lymphocytes due to the immune response of an infected vertebrate and isolation and extraction of these cells. The cells are then fused with myeloma cells, thereby forming hybridoma cells, that are then allowed to produce monoclonal antibodies (mAb's) indefinitely in cell culture. The protocol is demonstrated in Figure 4.3 below. Hybridomas are both laborious and expensive to produce and can

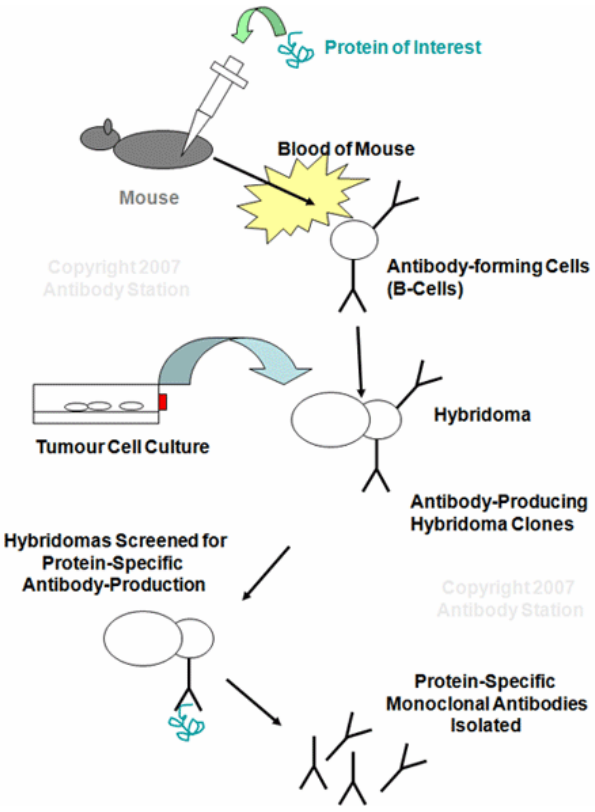

Figure 4.3. The *Hybridoma Technique* is the predominant method for generating monoclonal antibodies for commercial and laboratory applications. [Taken 10/28/2008 from **http://www.antibodystation.com**]

often prove restrictive. It is obviously difficult to create Ab's using this process for toxins or for targets which do not elicit an immune response. Additionally, mAb's tend to vary from batch to batch [122]. It is also impossible to generate mAb's for targets under non-physiological conditions. These proteins are also sensitive to temperature and pH changes, and denaturation of the molecule is irreversible. Finally, Ab's are relatively large (150 kDa) and difficult to immobilize on various surfaces in such a way that ensures its binding capacity for its target.

Aptamers

As previously mentioned, aptamers are oligonucleotide sequences that can selectively, and with high affinity, bind a target ligand. Both RNA and DNA strands can fold into a plethora of well-defined secondary and tertiary conformations for a given sequence, which is the basis for using them as binding agents for a wide variety of molecular targets. Aptamer have been found to undergo significant conformational changes upon binding with its target ligand, generally yielding a new complex in which the aptamer becomes imbedded in the tertiary structure of the target ligand [123]. Selection of the appropriate oligonucleotide sequence represents the crux of determining appropriate aptamers for different target ligand.

The first *in vitro* selection of RNA was accomplished in 1974 by Sol Spiegelman [124]. It was only after the development of polymerase chain reaction (PCR), however, that it became reasonable to more generally search for appropriate aptamer species for known target ligands [125]. So ripe was the field for such a breakthrough, that three separate groups (two within the same month) developed a similar process, exclusive of one another, for aptamer selection [126-128]. The process developed for aptamer

selection is now referred to as the Systematic Evolution of Ligands by EXponential enrichment (SELEX) process. This process is described in Figure 4.4 below. The SELEX process is essentially a technique for reviewing extraordinarily large combinatorial libraries (most systems start with a DNA library containing 10^{14} to 10^{15} individual and distinct molecules) through an iterative process allowing for *in vitro* selection and subsequent amplification of selected oligonucleotides. The process is repeated as many times as necessary to determine the best oligonucleotide for a given target, for degree of specificity (rejecting candidates that bind structural analogs), and for maintained activity in desired environmental conditions. Early implementation of the SELEX process would take as long as two days to accomplish a single round. Given that between 8 to 15 rounds are necessary to yield an acceptable aptamer candidate, the overall process would take the better part of 2-3 months of constant refinement [122]. Vast improvements in instrumentation automation and understanding of individual step sensitivities has shortened the time of each round to less than 2 hours, yielding final candidates in less than 2 days [129].

The use of aptamers as capture agents in biosensor applications has the following advantages [122]:

- Large number of thermodynamically stable structural variants vs. peptides of equal length
- No known structure for which aptamers cannot be made to bind to
- Specificity and affinity to match and, in some cases, surpass antibodies
- Can use DNA microarray spotting technology to immobilize defined densities in precise locations on a large scale

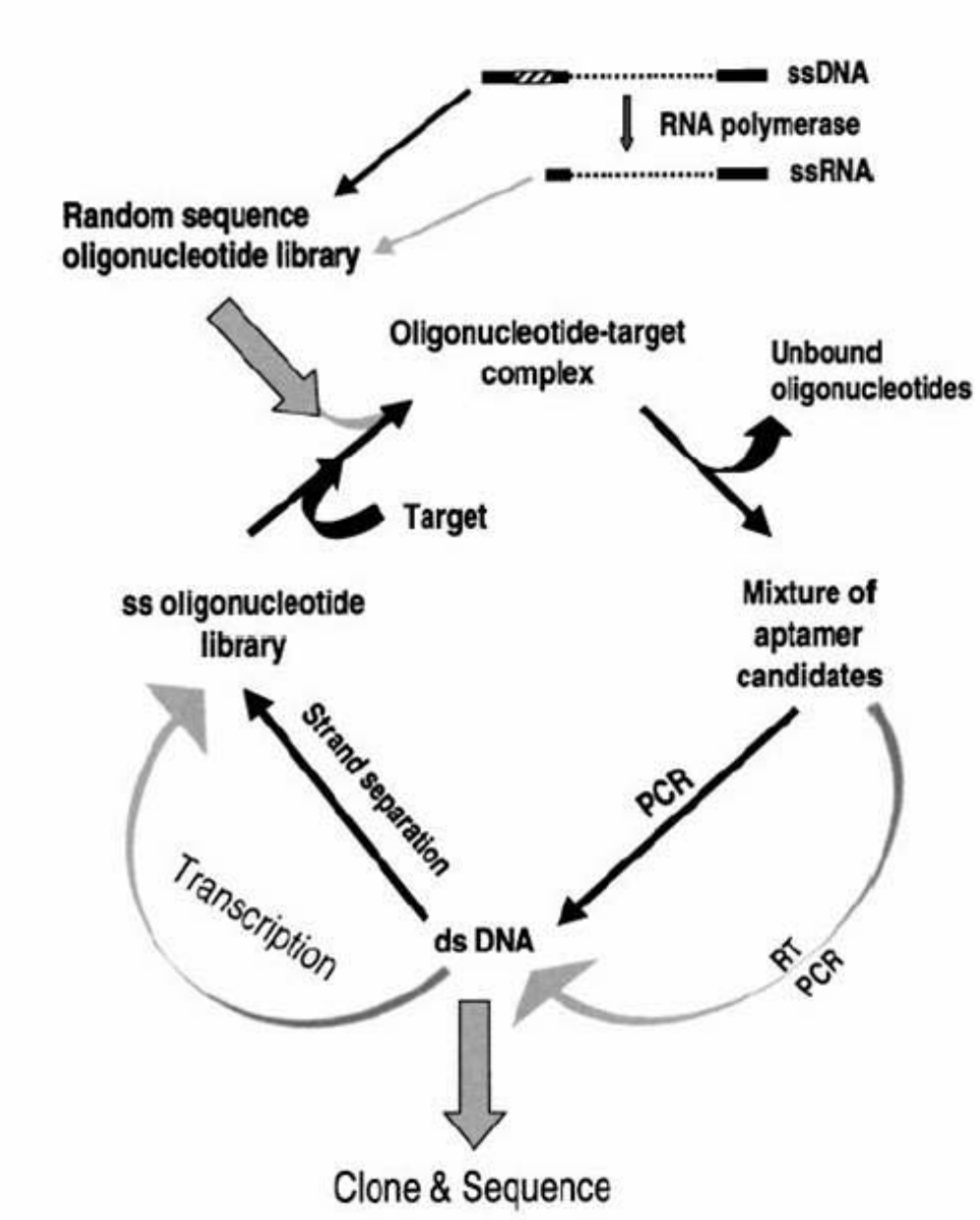

Figure 4.4. Systematic evolution of ligands by exponential enrichment (SELEX) process.

- Selected species can easily be modified to improve affinity and specificity (unlike Ab's) as well as to improve robustness in various environments
- Aptamers are much lighter and smaller, thereby capable of forming denser layers and being closer to the "sensing" surface

- Generation and selection is performed *in vitro*
  - Can function in non-physiological conditions
  - Selection conditions can be manipulated, allowing kinetic parameters to likewise change on demand
- Can be used for toxins or other targets that do not elicit an immune response
- Little to no batch-to-batch variation
- Reporter molecules (eg. radio-labeling) and other modifications can be arbitrarily bound at precise locations, increasing capability and variability
- Denaturation is reversible
- Long shelf-life under adverse conditions
- Can bind target proteins irreversibly, if desired
- Rapid automated selection process for aptamer isolation
- Oligonucleotide clones are cheap and easy to mass produce

The Decision to Use Antibodies

With regards to applications specific to this research, there are two attributes in particular that make aptamers especially attractive. First, it becomes possible to fabricate sensors with re-usable surfaces. Aptamers can be made to release their target upon exposure to extreme heat, salt, or chelating agents [130-132]. Second, aptamers are easily immobilized on nearly any surface with controllable densities [132]. Given the limited investigation of covalently binding capture molecules to the surface of planar ZnO, this becomes an obvious advantage.

There are disadvantages, as well, to using aptamers. First of all, they are generally not commercially available for many targets. In order to obtain aptamers for any particular target, one would most likely have to partner with a laboratory that has the time and inclination to collaborate. Georgia Tech does not have such a laboratory, so any collaboration would likely need to be conducted remotely. Secondly, nucleic acids are notoriously difficult to deal with and would likely require significant expertise in biochemistry in order to manipulate for a novel application. While I have a confident grasp of the fundamentals of biochemistry, a parallel doctoral-level pursuit in the field would be neither feasible nor appropriate. Finally, the application itself of a new aptamer species to a previously un-investigated planar surface is entirely novel, and would require a greater investment in time and resources than pursuit of a more conventional approach.

Given the already significant challenges of the goals of this thesis research, it is unlikely that this would be the more expeditious solution to the dilemma of functionalizing the surface of my biosensor. Suffice it to say that there is extraordinary potential in the use of aptamer technology as the capture mechanism for biosensor applications. It is strongly felt by this researcher that due to advantages such as size, overall stability, and the potential for reuse of each sensor, that aptamers will likely play a significant role in the ultimate development of this and other biosensor technologies.

I have therefore determined that because of the prevalence of existing immobilization techniques and relative ease of procurement, Ab's should be used as the appropriate capture agent for functionalization of these biosensors. It must be repeated that this approach still has drawbacks, such as being relatively costly for mass production, slow development times, and the relatively large size of each molecule, to name a few. This

approach still accomplishes the proof of concept for this sensor technology. In the future, it will likely be more interesting to pursue aptamers and other molecules that offer means of skirting these drawbacks. Given our capture agent selection and device function, we can therefore identify the biosensor being developed as a label-free immunosensor array.

Surface Preparation Protocol

As mentioned above, a critical aspect for the development of label-free immunosensors is the employment of *highly uniform* and *repeatable* antibody immobilization techniques. As previously discussed, silane chemistries offer a strong possibility for successfully immobilizing Ab's on the surface of our ZnO in a covalent manner. A review of the literature identifies two different molecules appropriate for such a purpose. They are (3-glycidyloxypropyl) trimethoxysilane (GPS), and (3-mercaptopropyl) trimethoxysilane (MTS) for the immobilization of IgG Ab's. In order to assess the chemical modification of the ZnO surface, I employed water contact angle measurements, atomic force microscopy (AFM), and fluorescence microscopy.

To provide visual confirmation of the density and uniformity of antibody immobilization, fluorescently labeled IgG antibodies are employed for each protocol. Over the course of the investigation, I found fluorescence microscopy to yield the most relevant information for assessing the surface coating uniformity and repeatability. The ultimate test of functionality is assessed by using the prepared devices in a basic sensor experiment. Publication of these findings can be found in [133].

ZnO Preparation

ZnO samples were prepared by depositing 500 nm of ZnO onto 3" (1 0 0) silicon wafers (University Wafer) by RF magnetron sputtering using the Unifilm PVD-300 sputtering system. The wafers were diced into 1 cm × 1 cm squares for the surface functionalization experiments. Prior to surface functionalization, the ZnO samples were sonicated in acetone for 5 minutes in an ultrasonic bath before being cleaned using an ion beam mill. The samples were milled in a 20% oxygen / 80% argon atmosphere for 5 minutes with a beam current of 9 mA at 50 VDC. This was done to remove any adsorbed chemical species from the surface and to provide a reactive surface for the silane to bind. It is important to note that the milling procedure was found to be absolutely critical to preparing highly repeatable and highly uniform surfaces. Without this step, all protocols attempted yielded relatively poor results.

Surface Modification

The silane solutions for treating the ZnO samples were prepared under a nitrogen atmosphere. The solutions prepared were a 4% solution by volume of MTS (Fluka) in dry toluene (Sigma) and a 4% solution of GPS (Sigma) in dry toluene. Immediately following the ion milling procedure to clean the ZnO surface, samples were placed in vials containing 2 mL of the silane, sealed in a centrifuge tube (VWR), and placed in a nitrogen environment for 24 hours. The samples were then removed from the vials and rinsed with ethanol followed by sonication for 5 minutes in ethanol (95%, Sigma). The samples were then dried with a stream of N_2 gas. Samples treated with the 4% MTS were then placed in vials containing 2 mL of 2 mM GMBS (Fluka) in ethanol and sealed for 24 hours. Following sonication in ethanol, GPS coated samples were immediately treated

with the protocol described in the next section. The MTS+GMBS coated samples were removed from the GMBS solution and sonicated in ethanol for 5 minutes. With the crosslinkers attached, the surfaces are now considered activated.

Covalent Antibody Attachment

The activated surfaces were treated with 548 nm Alexa-Fluor labeled Goat anti-rabbit IgG antibodies (Invitrogen). 25 μL of a 200 μg/mL solution of the fluorescently labeled antibodies in PBS buffer (pH 7.4) was pipetted onto the surface of the samples. The antibody solution was incubated for 2 hours in an opaque GelPak™ container (Fisher) in a nitrogen environment at room temperature. After incubation with the Ab solution, each substrate was rinsed with aliquots of PBS buffer followed by rinsing with a light stream of ultra-pure water (Burdick & Jackson) to remove any unbound antibodies from the surface. Control samples for testing simple antibody adsorption directly to the ZnO surface were also prepared by incubating ion etched ZnO samples with the antibody solution for 2 hours.

Based on previously described mechanisms [117, 121, 134], a summary of the reactions for covalently attaching antibodies to the ZnO surface is shown in Figure 4.5. Deposition of the silanes is achieved through reaction of the head groups with hydroxyl groups at the ZnO surface. The thiol group on the MTS molecules react with the maleimide region of the secondary crosslinker GMBS in organic solvent. This reaction leaves the succinimide residue of the GMBS available for antibody attachment. The succinimide residue then binds to an available amino group of the antibody to form a covalent bond between the antibody and the ZnO surface. It has been shown that antibodies immobilized using this approach still maintain a significant amount of activity,

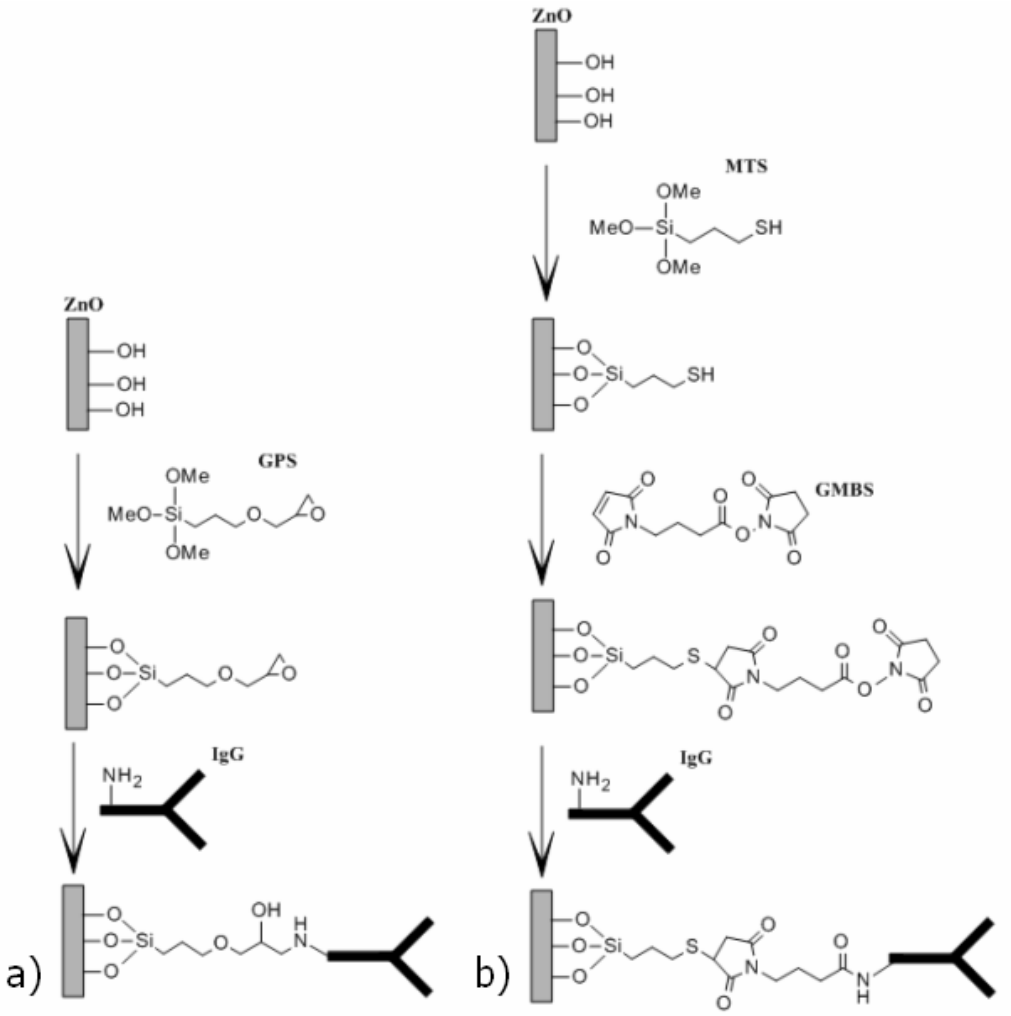

Figure 4.5. The proposed immobilization scheme for covalent attachment of IgG antibodies to the surface of sputtered ZnO using a) GPS and b) MTS + GMBS as silane-based crosslinkers.

albeit less than with oriented immobilization techniques such as those that target the carbohydrate group on the F_c region of the IgG antibody [118]. However, the ease and simplicity of the immobilization protocols studied here make them more suitable for biosensor applications than oriented immobilization techniques which often require numerous steps, harsh experimental conditions, and high antibody losses prior to immobilization.

Surface Protocol Results

Water Contact Angle Measurements

Water contact angle measurements were performed using an SEO Phoenix 150 Contact Angle Analyzer. The contact angles for each of the surface treatments were evaluated by averaging the contact angles from at least five separate measurements for each surface treatment, in which at least two surfaces for each protocol, following reaction with the silane. The silanized samples were measured and compared to a control sample consisting of ZnO with no surface treatments other than ion etching to clean the surface of any adsorbed species and sonication in ethanol to simulate the rinse process.

The results from the water contact angle (WCA) measurements after the samples were coated with the silanes indicate that the average WCA for each of the crosslinkers were greater than the WCA of the control, indicating an increase in surface hydrophobicity. The results are summarized in Table 4.1 below. Samples coated with MTS had an average water contact angle of 77° which were statistically different than the untreated ZnO (control) case which exhibited a water contact angle of 72°. The contact angle results for surfaces coated with MTS seem to agree well with previous WCA investigations of dithiol self-assembled monolayers on gold which were reported to be approximately 83.5° on average [135]. The WCA measurements performed with the 4% GPS solutions also suggest that the surface is being chemically modified. These samples yielded a significant increase in average WCA to 80º. An interesting phenomenon was observed for samples coated with GPS, however. Immediately after the water droplet is placed onto the sample surface, it was observed that the WCA is much higher than the control case indicating that the surface is hydrophobic. However, the WCA changes as a

function of time in a manner that seems to be unrelated to evaporation phenomena. The WCA value of 80º was averaged from measurements taken immediately after the drop was placed on the surface. After a period of 20 to 30 seconds, the WCA drops by about 5-7 degrees and then stabilizes. One possible explanation for this phenomenon is that the water droplets react with the exposed epoxy groups, hydrolyzing the ring to form surface hydroxyl groups which would result in increased hydrophillicity.

Table 4.1. Water contact angle measurements for surface treatments applied. (n = 10 for each case)

Surface Treatment	Avg. WCA (degrees)
Untreated ZnO	**72 ± 2**
GPS	**80 ± 5**
MTS	**77 ± 1**

Atomic Force Microscopy Measurements

AFM was used for monitoring the morphological changes at the surface that result from coating the surface with the crosslinkers and subsequent immobilization of antibodies. AFM was considered an appropriate instrument for assessing morphological changes at the surface as it is capable of measuring features with extremely high resolution (on the order or a few nanometers) and can do so at atmospheric pressure. This is important as the surface will contain antibodies, which would denature at the pressure and temperature required for vacuum systems such as SEM. Further, the measurement mechanism is roughly passive, when operated in tapping mode, as opposed to the significantly invasive (and potentially destructive) mechanisms that employ X-ray or electron beam modalities. Figure 4.6 shows typical stepwise AFM scans for each surface

after treatment with the crosslinkers and antibody solution, with surface roughness measurements summarized in Table 4.2.

A Digital Instruments (DI) 3000 AFM was used in tapping mode to measure the following: bare ZnO samples; samples after treatment with MTS+GMBS and GPS, respectively; and finally, samples after treatment with the crosslinkers + antibody solution. AFM probe tips were obtained from Veeco Instruments (FESP). Multiple scans

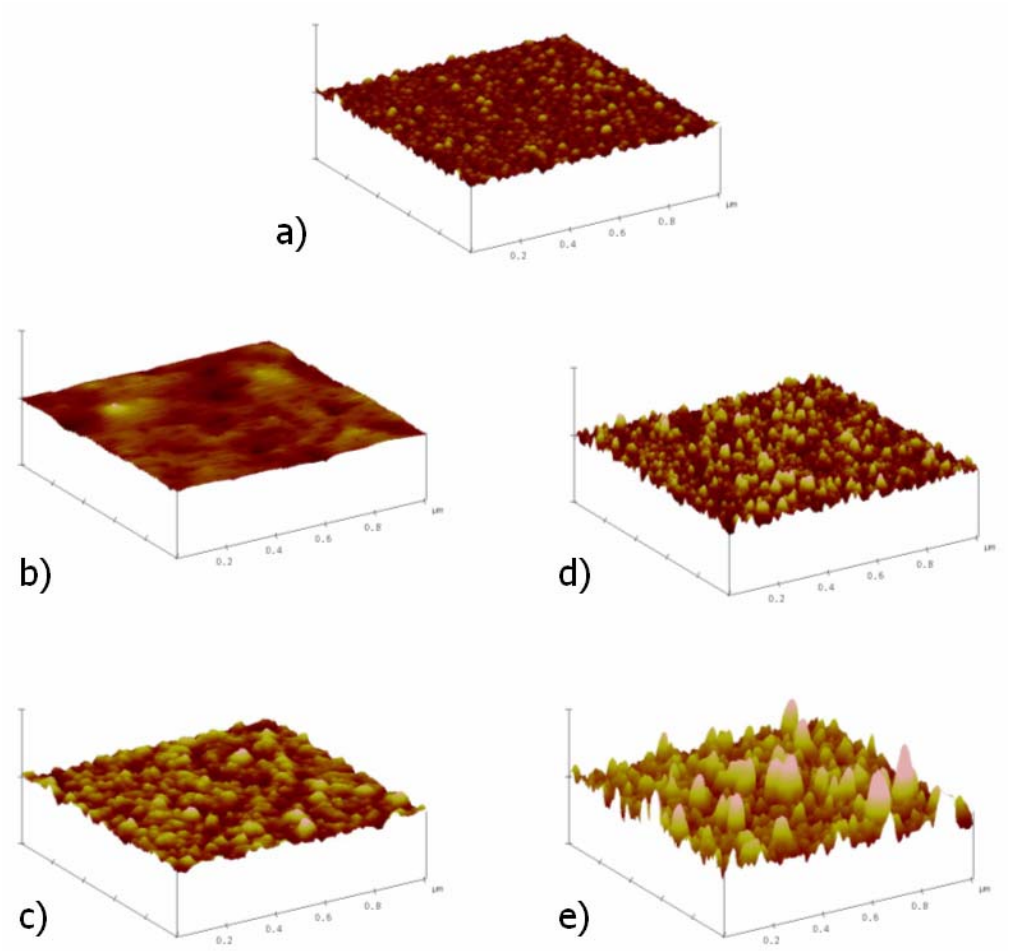

Figure 4.6. AFM topographical scans of a) the untreated ZnO surface and samples treated with b) GPS, c) GPS + Ab, d) MTS + GMBS, and e) MTS + GMBS + Ab. Scans are 1 μm x 1 μm with a vertical scale maximum of 65.0 nm.

Table 4.2. AFM surface analysis for each stage of both surface treatments [bounds are standard deviation].

Surface Treatment	Roughness (nm)	Avg. Particle Height (nm)	Avg. Particle Diameter (nm)
Untreated ZnO	2.8 ± 0.4	3.0 ± 0.5	24.7 ± 7.8
GPS	1.2 ± 0.3	2.3 ± 0.6	20.5 ± 11.3
GPS + Ab	2.0 ± 0.1	3.3 ± 0.8	24.1 ± 10.4
MTS	2.4 ± 0.1	3.4 ± 0.4	22.9 ± 5.8
MTS + GMBS	3.7 ± 0.8	6.8 ± 0.7	26.9 ± 8.4
MTS + GMBS + Ab	7.0 ± 1.5	13.7 ± 0.3	33.2 ± 6.9

of each sample were taken to across each 1 cm × 1 cm sample and scans were taken on multiple samples. The scans were evaluated for surface roughness and overall average particle height and diameter using the DI Nanoscope software.

Note Figure 4.6.a demonstrates the characteristic cobblestone appearance of the surface of the untreated control ZnO sample, with round grains that have fairly well defined boundaries. For the bare ZnO case, the mean surface roughness is approximately 2.8 (± 0.4) nm while the particle height is 3.05 (± 0.5) nm. The characteristic AFM scan of the surface after silanization with GPS in Figure 4.6.b shows a surface that is morphologically different from that of the controlled case. The average surface roughness decreases on average by 42% to 1.2 (± 0.3) nm. This implies an overall smoothening of the surface which is similarly suggested by the appearance of the scan. One possible explanation is that the GPS molecules have been deposited into the gaps in-between the grains to fill some of the grain boundaries. The results were observed at many locations across any single chip, and from chip to chip. After incubation with the antibody solution, the GPS+Ab treated surface has an increased surface roughness on average to 2.0 (± 0.1) nm with an average particle height of 3.3 (± 0.8) nm which indicates that the surface is being modified, statistically after treatment with the antibody solution. A typical scan is

shown in Figure 4.6.c. These results offer strong evidence that either antibodies were successfully immobilized on the surface due to this protocol or that the exposure of the GPS coated surface was morphologically altered upon exposure to the antibody solution.

The AFM scans of the samples treated with MTS+GMBS in Figure 4.6.d show significant differences in the surface morphology as compared to the GPS. Rather than a decrease in surface roughness, we see an increase in surface roughness to 3.7 (± 0.7) after treatment with MTS+GMBS. The average particle height for the MTS+GMBS treated samples was increased to 6.8 (± 0.4) nm indicating an increase in particle size due to deposition of the MTS+GMBS. Figure 3.2.e clearly shows the subsequent treatment with the antibody solution yields particles on the surface that have a significantly larger average height 13.7 (± 0.3) nm which is indicative of the immobilization of the antibodies to the surface. The data from these scans along with the WCA measurements provide confidence that the surface is being chemically modified and that the surfaces are morphologically modified after treatment with the antibody solution.

Confocal Microscopy

While the AFM scans offered significant evidence suggesting that the surfaces were being altered morphologically, they did not offer conclusive evidence that antibodies were immobilized on the surface. These scans were also unable to demonstrate uniform distribution of immobilized antibodies. I decided that an additional analysis was required in order to confirm the presence of antibodies and assess the degree of density and uniformity of any antibody immobilization. The antibody conjugation reaction was executed using both GPS and MTS+GMBS onto ZnO samples similar to those prepared for the AFM scans. The devices were then dried with a stream of N_2 gas and fixed to a

glass slide in preparation for confocal microscopy analysis. A Zeiss Laser Scanning Microscope 510 equipped with a HeNe laser (543 nm excitation) was used to visualize the distribution and intensity of the fluorescently labeled antibodies. Each sample was viewed at 10× and 40× magnification and images were taken at random locations throughout the area of antibody deposition. Control samples were prepared and analyzed for comparison between fluorescence due to antibody coverage and fluorescence to due background noise. Rather than incubation with the 200 μg/mL antibody in PBS, the control samples were treated with the full crosslinking protocol then incubated with 25 uL of 5 mM azide in PBS to replicate the solution containing the Alexa-Fluor labeled antibodies. Therefore, the only difference between the control and target samples is the presence of antibodies. To quantify the fluorescence for each surface treatment, the detector gain was fixed at a constant value and images were taken for all of the samples. The RGB luminance intensity signal was collected for each pixel in 0.03 mm^2 areas across the samples. The average fluorescence intensity was calculated by taking the mean pixel luminance intensity for each 0.03 mm^2 area and averaging the values over at least 25 measurements.

While the AFM scans clearly indicate that the surfaces are being modified with the surface treatment, fluorescence microscopy was employed to provide more information about antibody surface coverage density and uniformity. Prior studies characterizing antibody immobilization techniques have generated a variety of methods for analyzing the amount of antibodies bound to the surface of a material [117, 118, 134]. As acoustic biosensors become increasingly more compact, the antibody immobilization surface coverage becomes increasingly more important. It is necessary to compare the surface

treatments quantitatively, which is most effectively demonstrated in this study through an analysis of the fluorescence images due to fluorophor-labeled IgG molecules. Example images of typical responses for each surface treatment are demonstrated in Figure 4.7.

Figure 4.8 shows a comparison of the average fluorescence intensity (luminescence) for the two silane immobilization methods versus the untreated bare ZnO sample. Each scan includes the average fluorescent intensities accounted for by the control samples, which serve as an estimation of the combined background fluorescence from the ZnO, the crosslinker molecules (for the GPS and MTS+GMBS treated chips), and the PBS buffer. The average intensity was found to be highest overall for the MTS+GMBS+Ab samples as compared to the GPS+Ab and the bare ZnO. The fluorescence evident from the bare

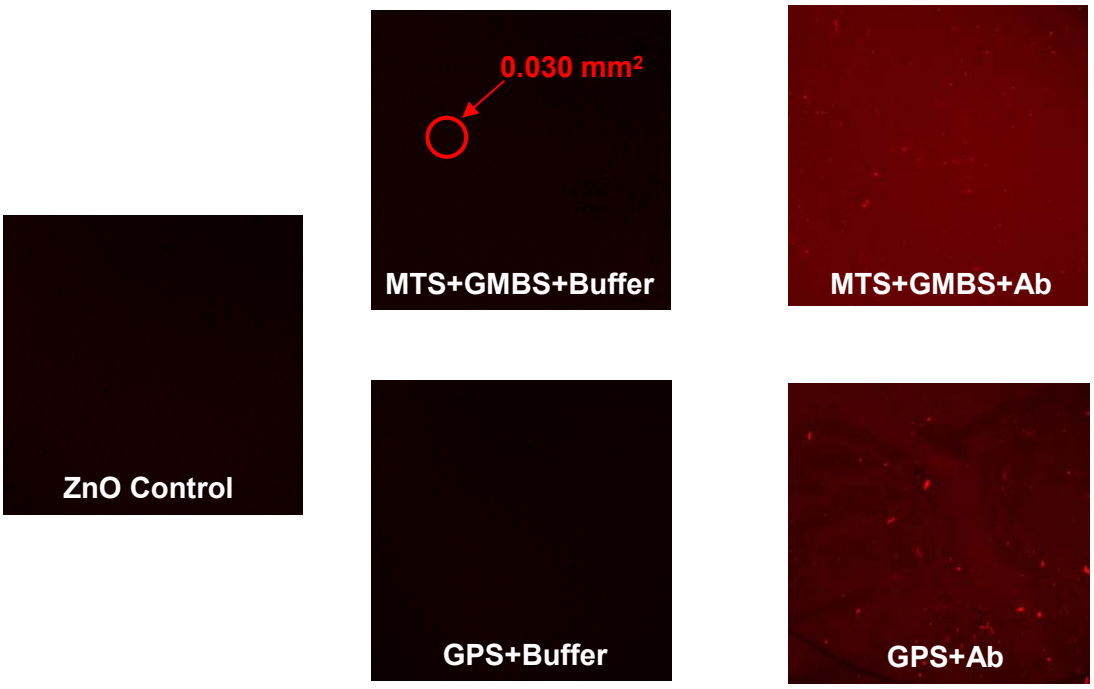

Figure 4.7. Typical confocal laser scanning microscope images upon HeNe excitation for different surface chemistry protocols.

ZnO sample treated with antibodies above the control can be attributed to a small amount of antibody adsorption to the surface of the ZnO in the absence of crosslinking molecules.

Statistically, the fluorescence of the samples treated with the MTS+GMBS+Ab were on average about 21% higher than the samples treated with GPS+Ab. Since variation of the fluorescence within a region of constant size can be attributed to the amount of fluorophor present, these results indicate a highly repeatable increased antibody surface coverage with the MTS over the GPS. The MTS fluorescence as compared to the untreated ZnO case indicates roughly a three-fold increase of average fluorescent intensity. The uniformity of the fluorescence is quite high as is illustrated by a relatively low standard deviation over 25 separate measurements across the sample. I also found

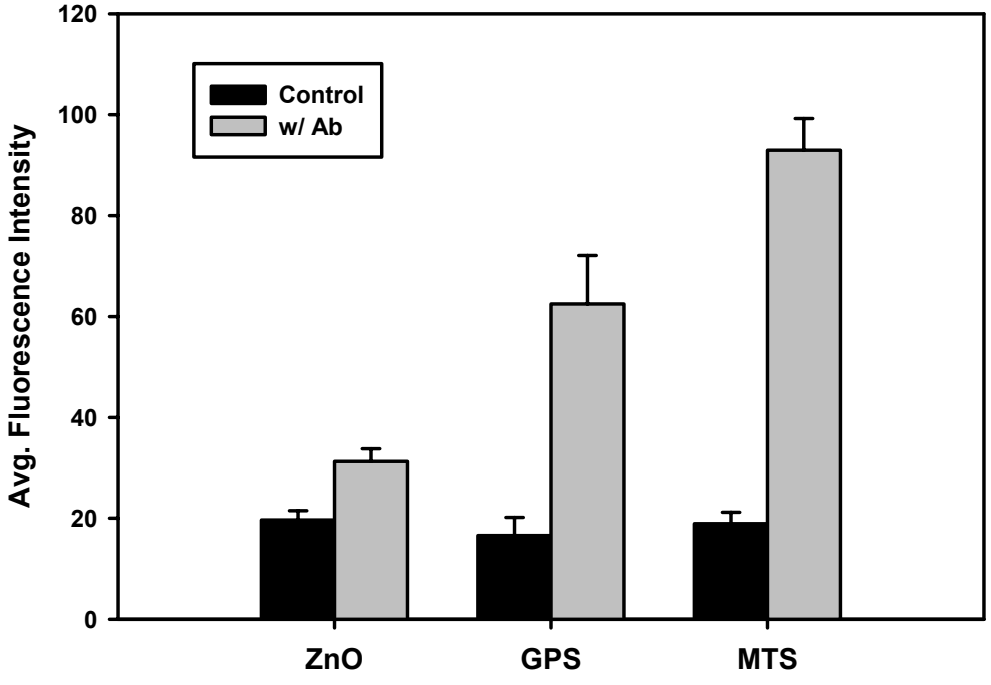

Figure 4.8. Average fluorescence intensity for each surface treatment after incubation with antibodies versus incubation with buffer [Error bars = Std. Error]. [n = 25 for each of the 6 cases shown]

the results to be repeatable from sample to sample which also indicates robustness in the protocol with each of these surface treatments.

CHAPTER 5

BIOSENSOR IMPLEMENTATION AND TESTING

The foundational components of my novel acoustic wave, label-free, immunosensor microarray have now been developed. It is therefore appropriate to apply these sensors towards cancer-relevant biomarker detection. The testing was broken up into two approaches. First, in assessing the potential sensitivity of the sensors, a dose response curve was generated for increasing concentrations of recombinant mesothelin-Fc protein in buffer. Positive indications from these experiments allowed me to pursue the application of these devices towards targets in more physiologically relevant media. The immunosensor microarrays were therefore prepared for detection of PSA in conditioned medium from a LNCaP prostate cancer cell line. The eight-device sensor arrays described in Chapter 3, designed to operate at ~2 GHz, were used for these experiments. In this chapter, I will describe specific needs for cancer detection in general and the relevancy of the two markers chosen. I will then describe the outcomes of both experimental goals.

Designing a Sensor for Early Cancer Detection

Advances in the understanding of carcinogenesis and tumor development are moving slowly towards developing a *complete* understanding of the etiology of various carcinogenic mechanisms. One extraordinary byproduct of this broad investigation is the discovery of new potential molecular targets, or biomarkers, for identifying malignancies at the earliest stages of development. It is often remarked that what is required to

accelerate this discovery process is a tool for high content screening of complex tissue samples [48, 123]. An ideal biomarker would obviously be a target that could be measured at detectable levels in peripheral blood, can clearly separate benign conditions from malignant disease, and whose levels would provide information for disease proliferation, or staging. Since it is very unlikely that such a marker exists for any condition, it is further necessary to develop a system that can efficiently screen for multiple targets. As discussed in Chapter 2 of this manuscript, a biosensor array is an appropriate way to approach high content screening capability and make use of these discoveries.

As indicated in Chapter 2, it is entirely unlikely that quantification of a single marker from patient tissue will satisfy the criteria for making diagnostic decisions with high-confidence. Some of the difficulties with using PSA for such a decision making tool has already been discussed, and will be covered further later in this chapter. It is already common therapeutic practice, however, to employ tools such as nomograms for making decisions regarding the treatment of cancer patients. Nomograms provide risk assessments for patients considering various therapeutic options based on a number of critical measurements specific to that individual compared with the outcomes of hundreds (if not thousands) of past patients that presented with similar conditions. The Body Mass Index (BMI) is one of the most commonly known nomograms. For prostate cancer patients, two nomograms in particular are widely used for assessing treatment options: the Partin Tables (developed at Johns Hopkins Hospital) and the Kattan Tables (developed at the Memorial Sloan-Kettering Cancer Center) [124-127]. Both nomograms require information such as Gleason score, PSA-related activity, and tumor staging.

Any tool developed for achieving HCS is likely to be applicable for post-therapeutic monitoring as well as clinical diagnosis and early detection. Since clinicians are already familiar and comfortable with the use of nomograms, information resulting from HCS tests can quickly be incorporated into the nomogram's algorithm. It is conceivable that extensive use of HCS biosensors coupled with significant elucidation of the proteome of various cancer proliferations could be entirely sufficient for early detection, tumor staging, treatment selection and appropriate continuous monitoring.

As mentioned in Chapter 2, a broad effort to develop biosensors that provide label-free detection of clinically relevant biomarkers is underway. Recent approaches in the development of biosensor array systems have made use of various optical [136-138], electrical [139, 140], and piezoelectric [57, 141, 142] transduction mechanisms, to name a few. Some of the efforts regarding the challenges associated with an acoustics-based tool for such a sensor array have been discussed in Chapter 2.

This research presents an acoustic-based solution that meets all of the requirements proposed by Erickson, *et al* [57], which includes significant sensitivity and specificity, multiplexing capacity, and reduced complexity and cost of fabrication. Here, I engage in a preliminary investigation of the potential of these devices as biosensors towards the following clinically relevant cancer biomarkers: human recombinant mesothelin-Fc fusion protein and prostate specific antigen (PSA).

Selected Cancer Biomarkers

Mesothelin

Mesothelin is a 40 kDa cell-bound surface glycoprotein found abundantly on normal mesothelial cells of the pleura, pericardium and peritoneum [143]. Mesothelial cells are flat in shape and are responsible for regulating the transport of cells and molecules into and out of the peritoneal cavity. Translation of the gene encoding mesothelin first yields a 71 kDa pre-cursor protein, which is subsequently split into a 31 kDa protein called megakaryocyte potentiating factor (MPF) and the 40 kDa mesothelin protein. Early investigations suggested that mesothelin played a role in cell adhesion[144], though subsequent work has called that into question [145]. Over-expression of mesothelin has been associated with several cancers including ovarian, lung, pancreatic, mesotheliomas, and squamous cell carcinomas [143, 144, 146-149]. The function of mesothelin remains largely unknown, but with regards to carcinogenesis, mesothelin is credited as playing a tumor differentiation function [150]. It has been shown that mesothelin should remain below 9 ng/mL in serum for healthy individuals and above 25 ng/mL for patients with advanced stage mesothelioma [151].

Prostate Specific Antigen

PSA is a 31 kDa glycoprotein, initially thought to be exclusively produced by the prostate gland [152]. Ironically, prostate specific antigen has since been found not to be specific to the prostate and has been discovered in low concentrations in the endometrium, normal breast tissue, breast tumors, breast milk, female serum, adrenal neoplasms and renal cell carcinomas [153]. PSA is a kallikrein-related serine protease responsible for the liquefaction of the seminal coagulum during ejaculation to aid in

semen motility [152]. The protein proved to be an appropriate forensic semen marker for rape cases and other criminal investigations in the late 1970's [152].

PSA has been employed as a key biomarker for prostate cancer diagnosis since the mid 1980's and is one of the only U.S. Food and Drug Administration (USFDA) approved markers for the diagnosis of cancer [154]. PSA testing coupled with the digital rectal exam (DRE) has an extensive history as the standard practice for diagnosis of prostate cancer in the U.S. [155]. PSA replaced prostatic acid phosphatase (PAP) as a marker for PCa diagnosis because of improved sensitivity [154]. 90% of apparently healthy men maintain a serum PSA level below 2.0 ng/mL and the generally accepted lower cut-off for a positive diagnosis is 4.0 ng/mL. That being said, malignant cases of PCa are certainly found among a small population of men with PSA levels below 2.0 ng/mL and there are also men with benign conditions with PSA levels above 4.0 ng/mL [154].

As indicated in Chapter 2, diagnosis of PCa from serum concentration of PSA has generated a significant amount of controversy that has persisted for more than a decade [58-60]. For men with PSA levels between 2.5 to 4.0 ng/mL, it is difficult to discern PCa from benign prostatic hyperplasia (BPH), and often leads to many unnecessary biopsies [156]. BPH is a relatively common condition experienced by roughly half of all men over 50 years of age [157], which similarly results in increased concentrations of serum-level PSA. As a result of this range of low specificity, a significant amount of work has been done to investigate alternate means of interpreting the results of PSA screening. Several practices have developed including measuring PSA velocity [158-160], the ratio of free to complexed PSA [152, 153], age-adjusted PSA [161], PSA density [162, 163] and

several others. The use of PSA velocity has emerged as more commonly used in clinical practice and refers to the time it takes to double ones serum concentration of PSA. PSA velocity is described as offering reasonably improved sensitivity for patients whose PSA levels fall below 4.0 ng/mL [147, 149].

Suffice it to say that PSA falls short of exhibiting the traits of an ideal cancer marker. More recent investigations have revealed alternative serum-level biomarkers that could offer greater specificity for PCa detection beyond PSA. These include early prostate cancer antigen (EPCA-2) [164], prostate stem-cell antigen (PSCA) [165, 166], α-methylacl coenzyme-A racemase (AMACR) [167], methylated glutathione *S*-transferase π gene (GSTP-1) [168-170], prostate cancer antigen 3 (PCA3) [171, 172], human kallikrein 2 (HK2) [173, 174] and Hepsin [175, 176]. EPCA-2 has emerged as one of the more promising candidates [177], discovered by a proteomic screening of 385 serum samples at the Brady Urological Institute at Johns Hopkins Hospital by Leman, *et al.*

The strength of any given biomarker is commonly assessed through receiver operator characteristic (ROC) curves. This measurement plots sensitivity vs (1 – specificity) in regards to the strength of the marker in diagnosing the condition in question. Sensitivity, in this case, describes the probability that the marker is a positive identifier of the pathology in question, or true positive. (1-specificity) refers to the probability that presence of the marker is not an identifier of an alternate condition, or a false positive. Another common metric used for comparing the strength of different markers is the calculation of the area under the curve (AUC) of the ROC curve. The ideal ROC curve would appear as a step function, indicating perfect specificity per level of detection

regardless of the acceptable false positive rate that comes with that concentration. The ideal ROC curve would yield an AUC of 1.0.

Leman *et al* generated ROC curves for both EPCA-2 and total PSA in distinguishing individuals with either PCa or BPH (Figure 5.1.A) and in distinguishing individuals with organ-confined (OC) and non-organ-confined (NOC) disease (Figure 5.1.B). As can be seen, for nearly all levels of acceptable false positive rates, EPCA-2 offers greater sensitivity for PCa. Figure 2 further demonstrates the ability of this marker in distinguishing PCa from various alternative conditions. Overall, using the cut-off

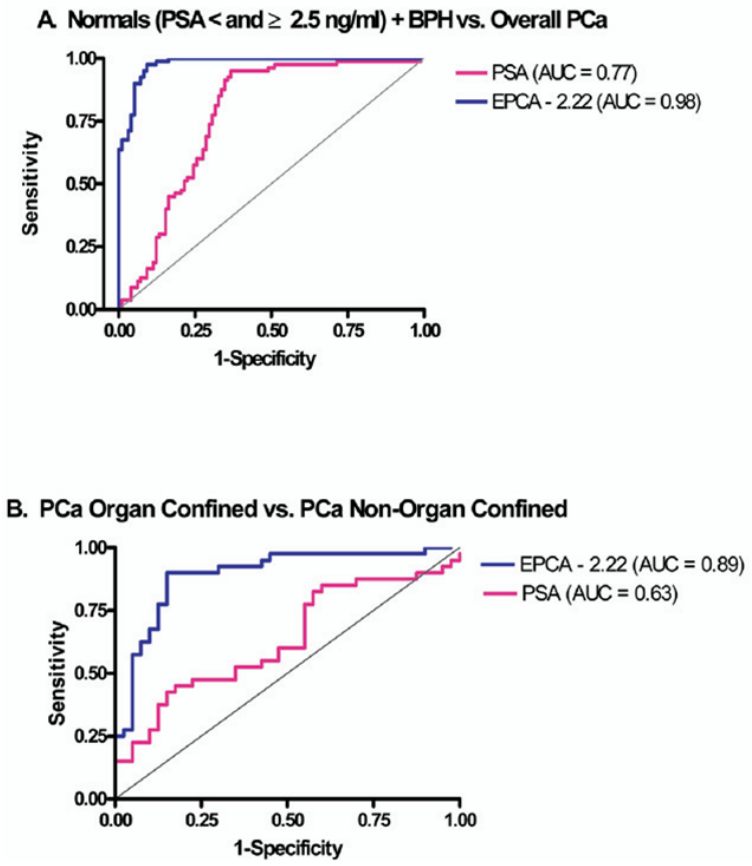

Figure 5.1. ROC curves for EPCA-2 and PSA in separating (A) healthy men with BPH from those with PCa and (B) distinguishing those with OC from those with NOC disease (80 patients with prostate cancer selected according to their OC or NOC disease status) [164].

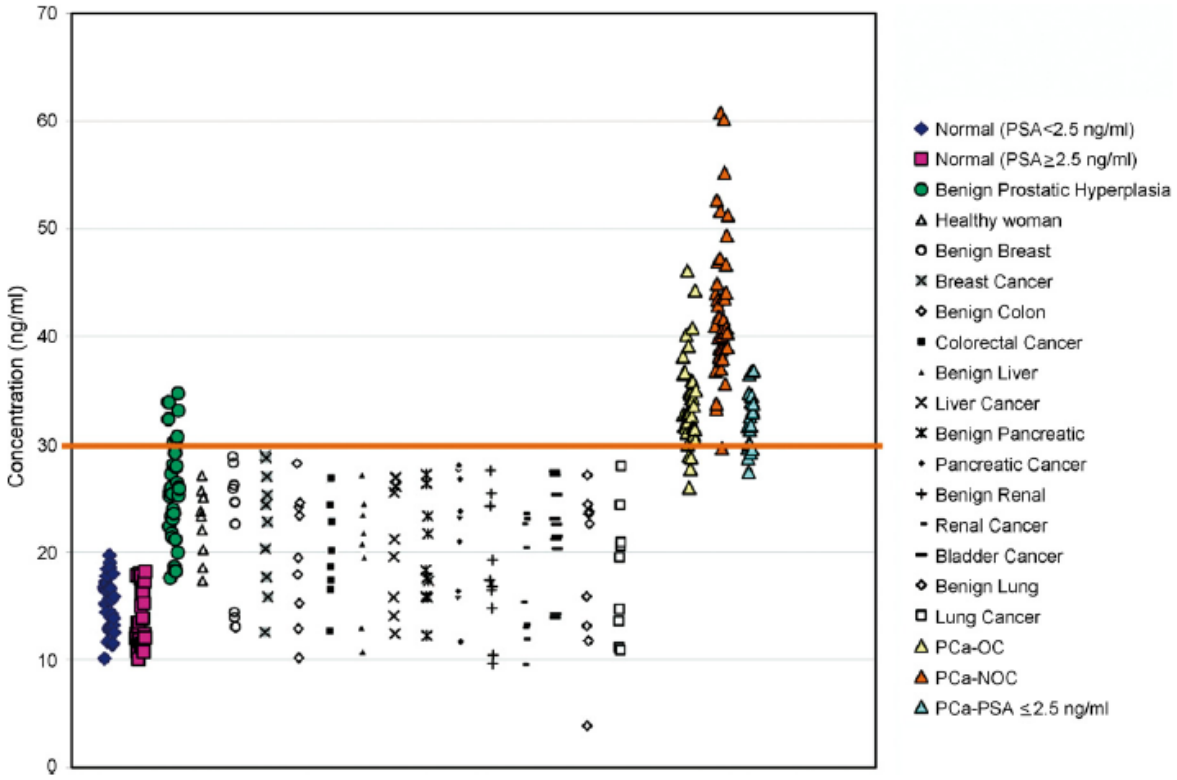

Figure 5.2. Serum analysis of EPCA-2 in study populations. Total of 330 serum samples screened for EPCA-2. Indirect ELISA's showed that EPCA-2 has a cutoff of 30 ng/mL or greater at estimated concentration. Cutoff represented by red line across graph [164].

concentration of 30 ng/mL, EPCA-2 assays were found to demonstrate 92% specificity and 94% sensitivity for individuals with PCa (AUC = 0.89). PSA demonstrated an overall specificity among the same population of only 65% (AUC = 0.62) [164].

Sensor Preparation

As mentioned in the introduction to this chapter, the goal is to assess both the sensitivity and specificity of the sensor design. A dose response curve is generated to assess the sensitivity of the sensor using varying concentrations of purified recombinant

mesothelin-F_c in buffer. To test device specificity, sensor testing was performed to identify the presence of PSA in LNCaP, a prostate cancer cell line, conditioned medium. Recognition elements for fluoroscein isothiocyanate (FITC) were used as the negative control, as no FITC is present in LNCaP conditioned medium (CM). As a secondary validation of the PSA results, a commercially available immunoassay kit was also employed to quantify the level of PSA in the LNCaP CM.

Resonator arrays were fabricated as described in Chapter 3. Device operation and subsequent sensor testing was accomplished using a HP 8753 C Network Analyzer, equipped with a S-parameter test set and a Cascade Microtech 9000 Probe Station with a temperature control chuck. Devices were probed using Cascade Microtech ACP40 GSG-150 probes.

IgG antibodies were covalently attached to the surface of the ZnO piezoelectric film using the functionalization protocol described in Chapter 4 and summarized in Appendix D. In short, the protocol employs mercaptopropyl-trimethoxy silane (MTS) as a primary crosslinker to the ZnO surface, followed by N-γ-maleimido butyryloxy-succinimide ester (GMBS) as a secondary crosslinker to covalently bind IgG molecules at the F_c fragment to the device surface. The protocol is described by Figure 8. MB Anti-mesothelin mAb were obtained from Dr. Ira Pastan at the NCI and are described in [178]. All other mAb were obtained from Santa Cruz Biotechnology, Inc [anti-FITC (sc-69871) and anti-tPSA (sc-52170)]. Anti-tPSA, or total PSA, refers to an antibody specific to both complexed and free PSA.

Sensitivity Assessment

Sensitivity testing was executed by preparing sensors to target mesothelin and applying them to varying concentrations of recombinant mesothelin-Fc protein in PBS. Purified recombinant mesothelin-Fc protein in buffer was obtained from Dr. Ira Pastan at the NCI. Serial dilutions were prepared using PBS (pH 7.38) to create concentrations of 1 ng/mL, 10 ng/mL, 100 ng/mL, 10 μg/mL, and 50 μg/mL. The functionalization protocol was performed with anti-mesothelin "MB" polyclonal IgG antibodies also supplied by Dr. Pastan on five separate 8-device arrays. 30 μL of each concentration of the purified protein solution was then deposited on the surface of each sensor array and allowed to incubate at room temperature for 20 minutes. After the incubation period, devices were rinsed with PBS buffer then DI water then dried with a N_2 stream prior to measurement. S_{11} scattering responses for each device of each array were collected both prior to exposure to mesothelin solutions and again after the 20 minute incubation time.

Individual devices are measured both before and after exposure to the liquid sample under test. Scattering responses are converted to impedance values using equation (3.15). The peak of the magnitude of the impedance response represents the condition of parallel resonance, as described in Chapter 3, which is an easily monitored condition. An example of the frequency shift observed after exposure to the sample is depicted in Figure 5.3.

Figure 5.4 shows the device detection with increasing frequency shifts in response to increasing sample concentrations, returning a 195 kHz shift for the 50 mg/mL concentration and 29 kHz shift for the 1 ng/mL concentration. It is important to put the magnitude of these shifts in context. Prior investigations using QCMs (see Figure 5.5) as

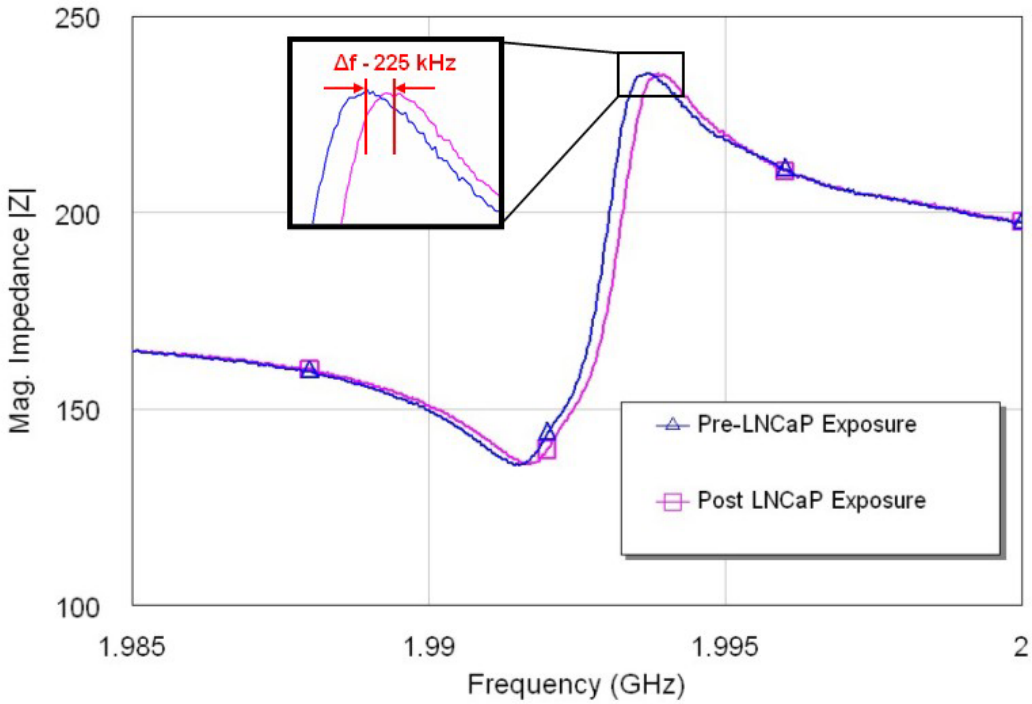

Figure 5.3. Typical impedance response of single sensor device showing response before (Δ) and after (□) exposure to the liquid sample under test. The peak of each curve represents the condition of parallel resonance.

the sensor for detection of a known target (sonic hedgehog, SHH) in the same LNCaP CM yielded only an 80 Hz frequency shift due to ~3 ng/mL concentration [179].

The actual concentration of SHH was determined by ELISA to be 0.2 ng for 70 µL of sample, or ~3 ng/mL [179]. At the lower concentrations, I observed frequency shifts almost 400 times greater in magnitude. This demonstrates an exceptional capability regarding *potential* limit of detection but cannot be directly compared due to the difference in targets and antibody affinities etc. Further device optimization will no doubt improve the sensitivity. Currently, however, the devices were clearly capable of broadly distinguishing increasing concentrations. Obviously the device response slows below 100 ng/mL, which indicates that more work must be done to reconcile overall mass resolution.

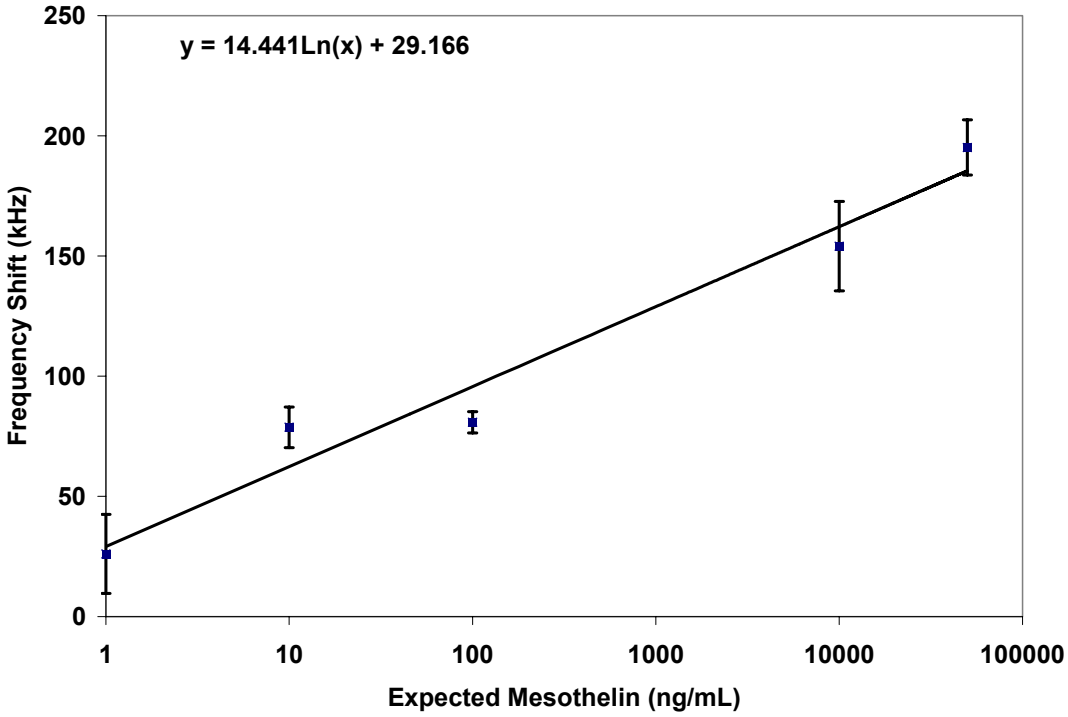

Figure 5.4. Dose response curve due to varying concentrations of purified recombinant mesothelin-F_c in PBS buffer (pH = 7.38). n = 8 for each case above. [Error bars represent standard error ($\sigma/\sqrt{n}$)]

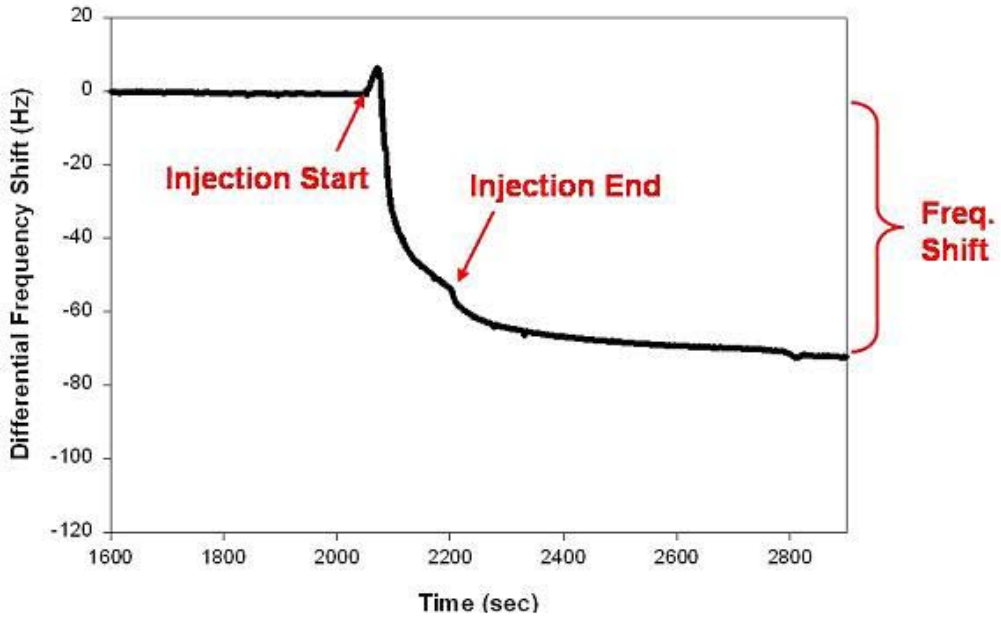

Figure 5.5. QCM sensor detection yields 80 Hz shift due to 3 ng/mL concentration of mesothelin in sample. While non-specific binding could compound the results, a control FITC antibody was used to subtract background binding [179].

A control experiment was performed using buffer solution of 10 μg/mL of recombinant mesothelin-F_c with a sensor array coated with anti-mesothelin and a separate sensor array coated with anti-FITC. The results are summarized in Figure 5.6. While the anti-mesothelin coated devices clearly indicate positive detection of the target protein over the anti-FITC coated devices, using analysis of variance I found that there was statistically little difference between the frequency shift associated with exposure of the anti-mesothelin devices to the 1.0 ng/mL solution and the anti-FITC control sensor ($p = 0.409$). As a result, no further testing was performed below 1 ng/mL because I determined this to be below the limit of detection for statistically significant differentiation from the reference.

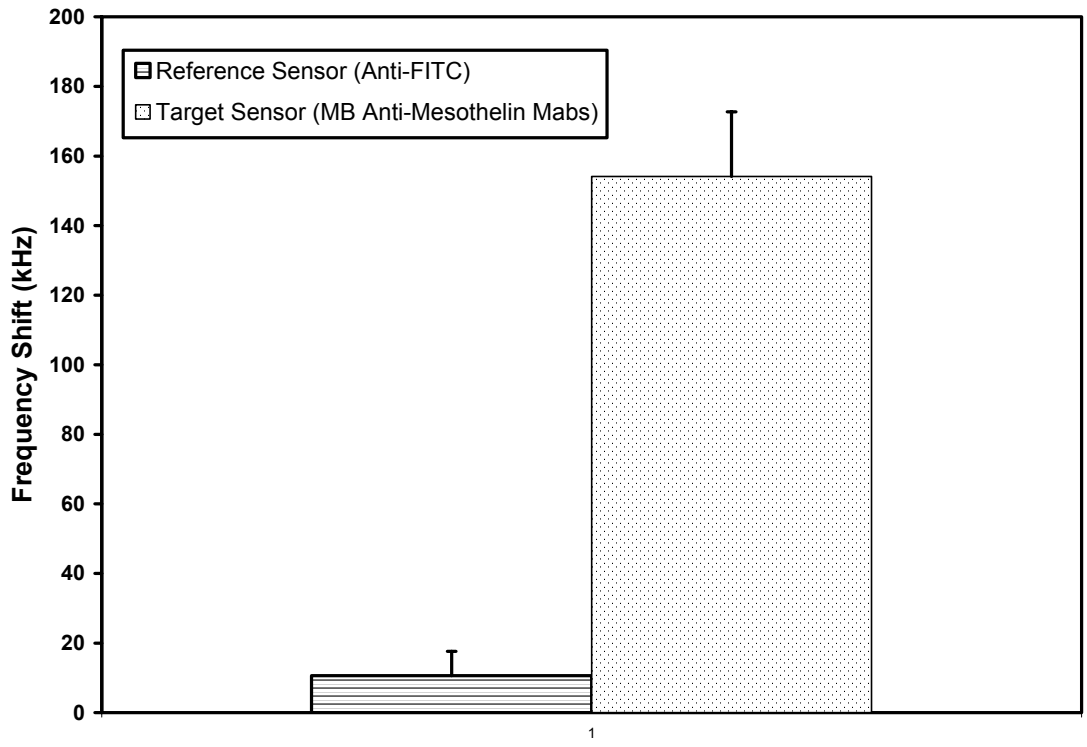

Figure 5.6. Control experiment depicting average frequency shift observed by a reference sensor (coated with anti-FITC, n = 4) and a target sensor (coated with anti-mesothelin, n = 6) after exposure to a purified solution of 10 μg/mL of recombinant mesothelin-Fc in PBS buffer. [Error bars represent standard error ($\sigma/\sqrt{n}$)]

It must be noted that sensor sensitivity is often defined as the slope of the sensor response curve to varying loads [180]. A traditional approach to determining this with gravimetric sensors is to deposit a known amount of mass on the sensor surface and measure the frequency shift. This is not plausible with biological samples, however, so a more useful method is to describe the overall sensitivity trends displayed under the given test conditions. As can be seen from Figure 1, the active region makes up only a very small portion of the total area of the array, all of which is exposed to the LSUT. Note that the vast majority of the device footprint is inactive, which includes the electrodes themselves. Deposition of the 30 μL sample more than covers the entire array. Future investigations should involve the development of an appropriate micro-fluidic flow cell which can limit the exposure to only the active resonance area of the sensor array to the LSUT, thereby making a sensitivity determination more reasonable. For this reason, I made an attempt to describe the overall sensitivity trends displayed under the given test conditions.

Specificity Assessment

LNCaP CM was obtained from Dr. Milton Datta at the Winship Cancer Institute at Emory University. LNCaP CM was obtained from exponentially growing LNCaP cells in RPMI-1640 medium, which was supplemented with 10% fetal calf serum, 4500 mg/L glucose, 1mM sodium pyruvate, 10 mM HEPES, 2 mM glutamine, and 15 mg/L sodium bicarbonate. The CM is therefore considered a sufficiently “noisy” environment for preliminary testing of device selectivity because it contains many proteins and other

molecules from the cells. The functionalization protocol was performed with anti-FITC and anti-tPSA each on a separate 8-device array. Anti-FITC is employed as a negative control, targeting a molecule not to be found in CM. As a secondary control (marked 'Control' during the experiment), the functionalization protocol was performed on a set of devices but the final step of incubation with some antibody solution was replaced with incubation with plain PBS. 30 μL of LNCaP CM was then deposited on the surface of each functionalized sensor array and allowed to incubate at room temperature for 20 minutes. After the incubation period, devices were rinsed with aliquots of PBS buffer then a light stream of DI H_2O then dried with a N_2 stream for measurement. S_{11} scattering responses of each device of each array were collected both prior to exposure to LNCaP CM and again after the 20 minute incubation period.

The results of testing multiple sensor arrays for our two targets are summarized in Figure 5.7. It is clear that the devices could distinguish the presence of PSA, though not as clearly as would be desired ($p = 0.139$). It is expected that due to the extensive molecular diversity of the LSUT, a significant degree of non-specific binding is likely occurring. This is demonstrated by the 70 kHz (on average) shift from the Control sensors, having the crosslinking molecules but no antibodies attached to the surface, as compared with the 49 kHz shift (on average) from the FITC-targeted negative control sensors exposed to CM.

A commercially-obtained enzyme-linked immunoassay (EIA) kit for PSA (Biocheck, Inc: BS-1019) was used to independently determine the concentration of PSA in the LNCaP CM. The protocol was followed as described by the manufacturer using n=3 for control standards and blank wells and n=6 for the LNCaP CM wells. LNCaP CM was

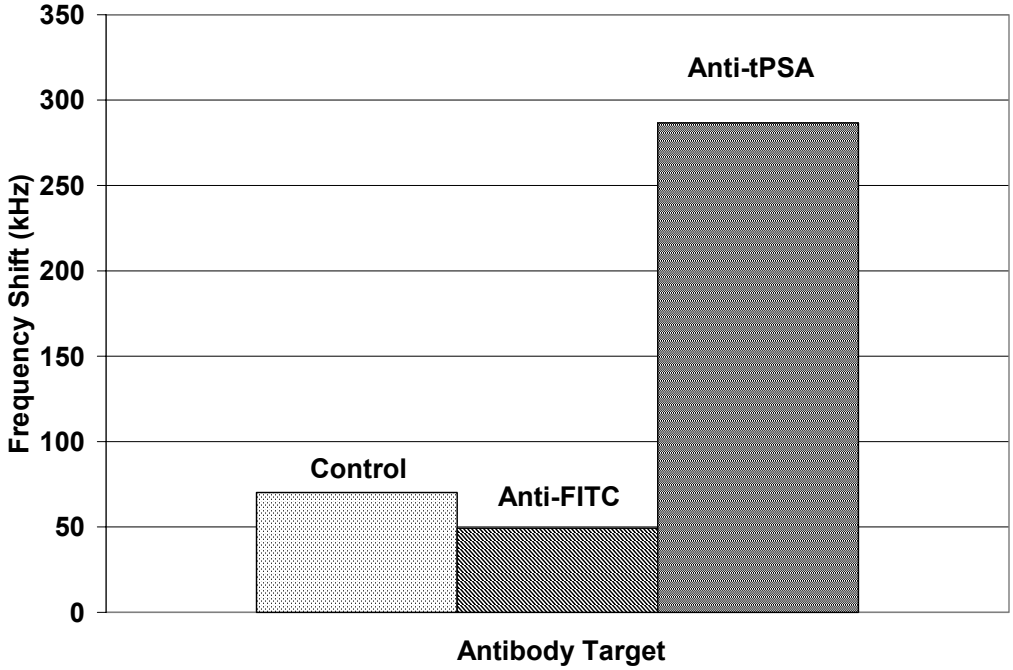

Figure 5.7. Comparison of the average frequency shift observed by sensors coated without antibodies (Control) [n=48], with anti-FITC (negative control) [n=44], and anti-tPSA [n=45] after 20 minute incubation with LNCaP CM.

diluted to 1:7 and 1:15 in PBS buffer. The results of the EIA are demonstrated in Figure 5.8 below. A commercially available EIA kit for PSA (total) was used to determine the actual concentration of PSA in the LNCaP conditioned medium. The results indicated the concentration of PSA to be roughly 950 ng/mL.

Given this very high concentration of our target, it is obvious that the sensor behaves differently given the "noise" of this testing environment. As stated at the beginning of this chapter, it was my goal to obtain preliminary results regarding the application of this sensor in a physiologically relevant medium. While the sensors are capable of distinguishing activity due to the appropriate target from control cases, they provide very little information regarding relative concentration. The testing protocol as it exists allows for many variables that must be controlled for, much of which can be solved with the development of an appropriate flow cell. Some of the variables I am referring to include

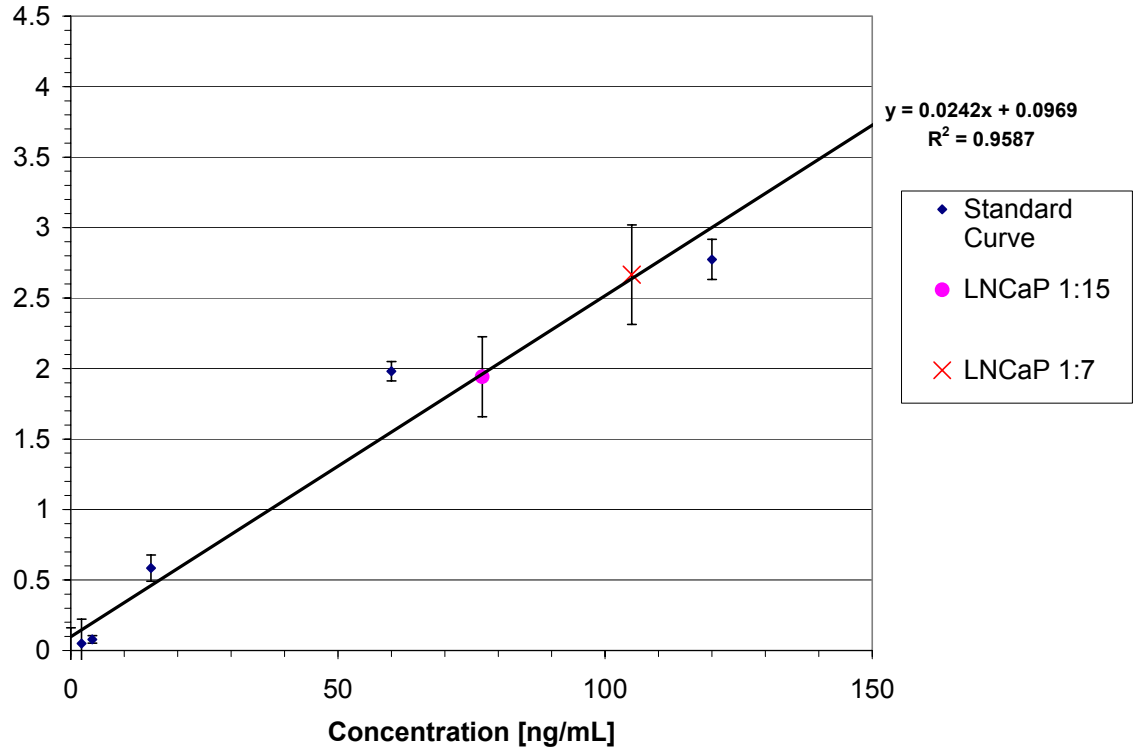

Figure 5.8. ELISA results for total PSA found in LNCaP conditioned medium using Biocheck, Inc BS-1019. (n = 3 for all standards, n = 6 for test samples)

varying distributed stress due to the application of the testing probes, drying of the surface environment, and uncontrolled exposure volumes are the most obvious.

Preliminary Packaging

I have taken steps towards developing a packaging system we are calling the AcμRay™ (Acoustic Micro-Array, pronounced – ak′ ū rā) that introduces controls for the variables I have listed above. The AcuRay™ system involves the development of two printed circuit boards (PCB), fabricated by Express PCB, which includes fixed electrical connections to each device, a fixed volume flow cell, and connectivity to an appropriate

network analyzer for monitoring. The package is shown in Figure 5.9 and is made up of a disposable array sensor board and a RF switch board. In order to achieve the fixed electrical connections, the electrode array needed to be redesigned in order to make connections with the disposable array sensor PCB board. Connections for each device were established by fusing electrodes from the fabricated sensor chip to the electrodes of the test board using conductive epoxy. A jig was developed (see Figure 5.10) to properly align the chip with the disposable PCB board and press the two pieces together while the conductive epoxy was allowed to set. Note that the test board also housed the liquid sample space that would expose the sensor surface to the liquid sample (Figure 5.9). It was envisioned that a flow cell could be attached to the sensor board here. Once set, the

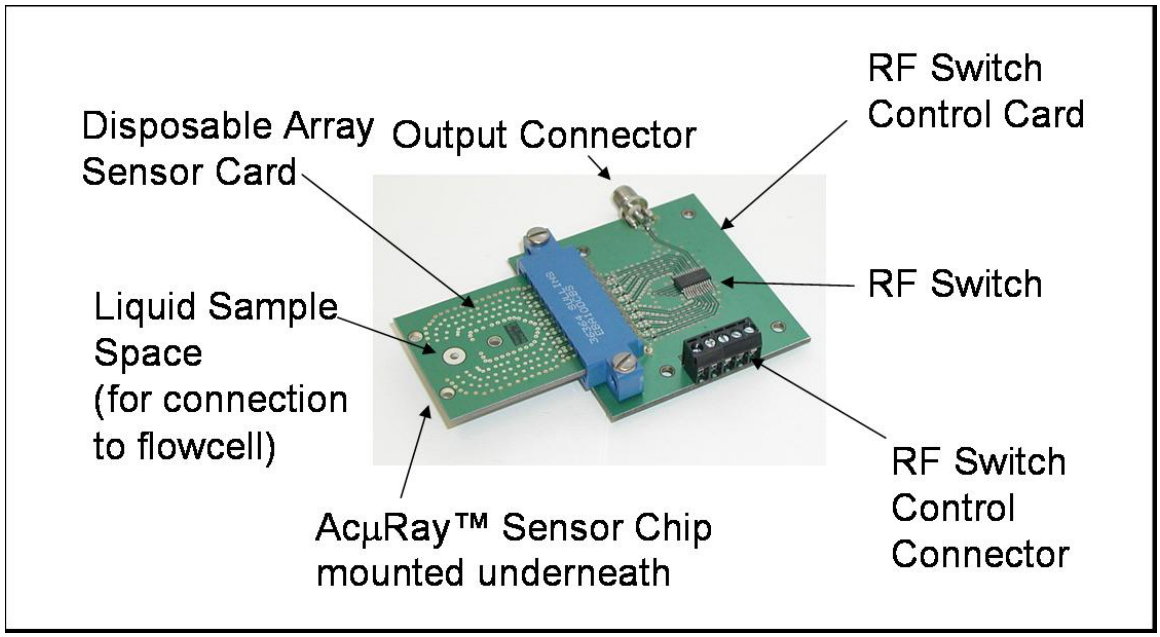

Figure 5.9. AcμRay™ System consisting of disposable array sensor card and RF switch card with appropriate connections.

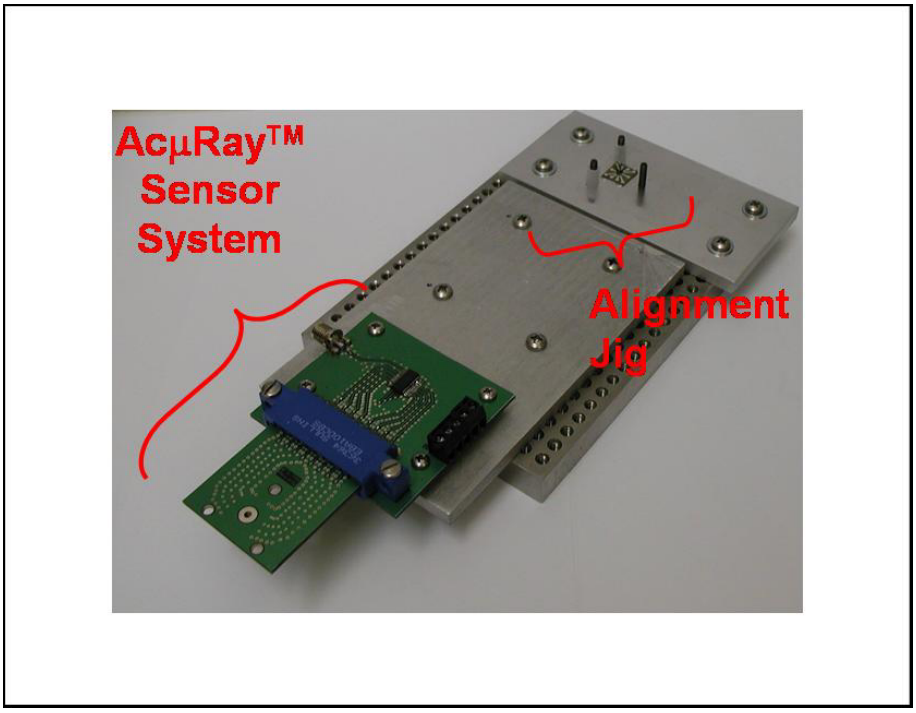

Figure 5.10. AcμRay™ sensor system, including alignment jig for loading sensor chips onto disposable sensor array board.

sensor board was connected via a PC card connector to the RF switch board. The RF switch board includes a SP8T RF rapid switching integrated circuit (IC) from Hittite Microwave Corporation (HMC253QS24). The switching IC was set up to be controlled by a computer via a National Instruments test controller (NI USB-6008). Once the network analyzer was connected the to the output of the sensor array via the SMA connector shown in Figure 5.9, the responses of each device could be obtained periodically as controlled by the RF switch.

CHAPTER 6

CONCLUSION

Over the course of this research, I have developed the fundamental components of a biosensor designed to meet the following specific aims:

1. A bulk acoustic resonator device appropriate for application as a highly sensitive biosensor.
2. An appropriate biosensor preparation procedure by immobilization of appropriate capture agents.
3. Demonstration of the functionality of these biosensors towards known cancer biomarkers.

The sensor was comprised of two fundamental components outlined in aims 1 and 2. The first is a transducer element capable of monitoring its environment for extremely small perturbations. The second is the functionalization of the transducer as a biosensor by preparing its surface for high specificity for a particular target.

To implement the transducer, a solidly mounted resonator consisting of alternating layers of W and SiO_2 were grown on a p-doped <1 0 0> Si substrates with ZnO as the active piezoelectric layer at the surface. More than a thousand successful devices have been fabricated and tested after an investigation that included the fabrications of several tens of thousands of test devices. The acoustic mirror was designed to have a reflection coefficient closest to unity near the frequency of operation. The acoustic mirror frequency response was simulated to provide assurance of the frequency range coverage given a fixed number of alternating pairs of W and SiO_2. Finite element modeling was

also performed to predict the electric field of an electrode configuration consisting of two long electrodes positioned on the top of the ZnO with a gap between them. Simulations showed that the electric field within the gap between the electrodes was primarily laterally oriented while the electric field directly beneath the electrodes was shown to be reduced in magnitude with an orientation normal to the surface of the ZnO.

To verify the thickness shear mode operation of the devices, I investigated the experimentally extracted acoustic velocity and the effects of water loading on the resonance. Without these tests it is difficult to adequately determine that a resonance is necessarily TSM. I have presented evidence of a TSM wave through exposure of the device to deionized water, comparison of extracted acoustic velocity with theoretical acoustic velocity, and varying the piezoelectric film thickness to yield respective changes in the frequency response.

I have further provided an investigation of two antibody immobilization techniques on planar ZnO surfaces. Several hundred surfaces were analyzed using water contact angle measurements, atomic force microscopy, and fluorescence microscopy to determine the surface characteristics and antibody surface coverage. I found that protocols employing both GPS and MTS are effective in immobilizing antibodies to the ZnO surface, but that MTS offers greater surface coverage, on average. The protocols yielded uniform and repeatable surface coverage using both methods which are necessary requirements for biosensor functionalization. Functionalization of crystalline ZnO surfaces is becoming an increasingly important topic as new biosensor platforms are being developed with this material. It was concluded that the MTS protocol offered superior results for functionalizing ZnO-based sensors due to the fact that it is a

commercially available chemical and provides high antibody surface coverage with good uniformity.

I have further demonstrated here results for a novel acoustic biosensor system that exhibits all the qualities required for advances in proteomics research. Specifically, this system offers the potential for extraordinary sensitivity due to its operation in the several GHz range. Given frequency shifts in the tens of kHz for a few ng/mL levels of detection, improvement in general noise levels offers the potential to achieve several orders of magnitude improvement on the limit of detection. Further, the system is a simple array design that can be mass produced with existing industrial microelectronic fabrication equipment to reduce manufacturing costs and allow for real-time multiplexed sensor reporting. This last point has obvious molecular micro-array implications which provide the capability of implementing testing redundancy (reducing false positives and false negatives) as well as rapid multi-target monitoring.

Any sensor platform of high sensitivity must additionally consider that false positives and false negatives significantly hamper the ability to employ such devices for research much less for patient diagnosis. A sensor array technology allows for monitoring of multiple sensors simultaneously which offers both replications of each measurement as well as the capability to identify a multi-protein signature. This is the strongest approach for minimizing false positives and false negatives. The development of such a system could have an impact at multiple levels including proteomic research, post-therapeutic and eventually early detection screening.

As mentioned at the beginning of this dissertation, the findings of this research have led to the following:

- 4 peer-reviewed professional publications
    - 2 first-authored
- 3 conference presentations
- 6 conference posters

Beyond publication of this research in the aforementioned professional journals and conferences, aspects of this research have also been independently selected for circulation by mass media. The American Association for Cancer Research (AACR) independently selected my abstract for a press release to promote the September 2007 Conference on Molecular Diagnostics and Cancer Therapeutic Development, presented in Appendix F. This was picked up by various news organizations, including CNN's Sanjay Gupta, US News & World Report, Forbes, WebMD, Medicine.net, CBC News, various NBC and CBS news affiliates, HealthCentral.com, ScienceDaily, PhysOrg.com, Dentalplans.com and Health Scout. Links for these are also copied in Appendix F. The work was also highlighted in the April 17, 2008, broadcast of CNN's *Next Big Thing*, with Miles O'Brien.

Beyond the outputs of this research, I have also acquired a great deal of practical knowledge peripheral to the field of study. This thesis work would not have been possible without gaining proficiency with the following equipment:

- Scanning electron microscopy (Leo 1530, Leo 1550, Zeiss Ultra60, Hitachi S800)
- Atomic force microscopy (DI 3000)
- X-Ray Diffraction
- Laser Scanning Microscopy (Zeiss LSM 510)
- Wafer probing (Cascade Microtech 9000)

- Microfabrication
    - Photomask design (ADS)
    - Plasma vapor deposition (Unifilm PVD 300)
    - Electron beam evaporation (CVC)
    - Photolithography
    - Ion beam milling
    - Step Profilometer (Tencor Alpha-Step)
    - Wafer dicing
- Immunoassay protocols (ELISA)

and the following software programs:

- Applied Wave Research – Microwave Office (SPICE-based circuit modeling program)
- Advanced Design System (CAD program)
- Cascade Microtech WinCal Software
- MATLAB

Not only was proficiency required for the use of much of the microfabrication equipment, but the Microelectronic Acoustics Group owns and maintains its own fabrication equipment. It would not be an exaggeration to say that at least 15% of all the time spent in the laboratory for this doctoral program was spent on maintaining, modifying and often repairing this equipment. The Unifilm PVD-300, in particular, is a relatively complicated piece of equipment, comprised of more than 15 constantly degrading units including the vacuum chamber itself. I was exclusively in charge of maintaining this instrument for the entirety of my dissertation program, which underwent constant maintenance and had a

massive breakdown at least once a year, on average. In addition to the Unifilm, I was similarly in charge of monitoring and repairing the CVC E-beam evaporator system, the Karl Suss MJB3 Mask Aligner system, and various other pieces of equipment. This is in addition to the ordinary complexities and intricacies associated with using core facilities such as the AFM and the Confocal LSM.

Over the course of this thesis work, I have developed several novel contributions to the field of biosensor microarrays. As summarized in the introduction of this manuscript, they include the following:

1. The development of a novel thickness shear mode bulk acoustic resonator utilizing ZnO;
2. The novel application of an appropriate surface chemistry protocol for functionalization of planar ZnO with monoclonal antibodies;
3. Implementation of these sensors toward detection of clinically relevant cancer biomarkers.

APPENDIX A: MATLAB CODE – MIRROR SIMULATION

```
% mirror.m
% written by Anthony Dickherber, January 2004

%Set frequency range
f = 0:12e4:6e9;
w = 2*pi*f;

NumLayers = 6;
d = zeros(1:6);

%as given by page 56...unknown calculation/derivation/source
%Z0 is the substrate material (Si), Z(odd) is the high acoustic
impedance

%material and Z(even) is the low acoustic impedance material
%NOTE: Impedances are normalized by the active area of the device
Z0 = .5;   %Si Substrate Z=0.5
%ZH = .7837;   %AlN is 1.0672
%ZL = .4549;   %SiO2 is 0.4183

CenterFreqofInterest = 2e9;

%material parameters for high and low acoustic impedance materials
rhoo = 2332;    %bulk Si density, from Auld
rhoL = 2200;     %density SiO2 = 2200 (fused silica from Auld)

%rhoH = 8200;    %Ta2O5, from Shawn's thesis
%rhoH = 7450;    %for LiTaO3
%rhoH = 4700;    %for LiNbO3
%rhoH = 3986;    %for Al2O3
rhoH = 19200;   %for W (from Auld)

C44o = 7.956e10; %c44 for Si (from Auld)
C44L = 3.12e10; %c44 for SiO2 (fused silica from Auld)

%C44H = 5.69e10;  %c44 for Ta2O5
%C44H = 9.4e10;    %c44 for LiTaO3
%C44H = 6.0e10;   %c44 for LiNbO3
%C44H = 14.5e10;  %c44 for Al2O3
C44H = 13.4e10;   %c44 for W  (crystalline from Auld)

%Calculate the normalization factor for impedance values
Ro = sqrt(rhoo*C44o);
NormFact = Ro/Z0;

%normalize impedance values of low and high impedance materials
ZH = sqrt(rhoH*C44H)/NormFact;
ZL = sqrt(rhoL*C44L)/NormFact;

%using the values for stiffness coeff. and density on page 62
VH = sqrt(C44H/rhoH);      %[m/s]
```

```
VL = sqrt(C44L/rhoL);      %[m/s]

%define thicknesses found on page 98 of thesis (lambda/4)
dH = 1/4*(VH/CenterFreqofInterest) %[m]
dL = 1/4*(VL/CenterFreqofInterest) %[m]

%calculate wave number for both regions
kH = w/VH;
kL = w/VL;

%Set up the Impedance matrix
Zeq = zeros(NumLayers-1,length(f));

%calculate equivalent impedance of stack shown on page 56 figure 3.8
%using equation 3.11 found on page 55 of Shawn's thesis

%Calculate impedance for first layer due to Z0
if mod(NumLayers,2)>0
    Zeq(1,:) = ZL*((Z0 + i*ZL.*tan(kL*d(1))./(ZL +
i*Z0.*tan(kL*d(1))));
    disp('1 Low')
else
    Zeq(1,:) = ZH*((Z0 + i*ZH*tan(kH*d(1))./(ZH + i*Z0*tan(kH*d(1))));
    disp('1 High')
end

%Calculate impedance for the rest of the layers
for n = 2:(NumLayers-1)
    if mod(n,2) > 0
        Zeq(n,:) = ZH*((Zeq(n-1,:) + i*ZH*tan(kH.*dH))./(ZH + i.*Zeq(n-
1,:).*tan(kH.*dH)));
        disp('High')
    else
        Zeq(n,:) = ZL*((Zeq(n-1,:)+i*ZL*tan(kL*dL))./(ZL+i.*Zeq(n-
1,:).*tan(kL*dL)));
        disp('Low')
    end
end

%Zeq(2,:) =
ZL*((Zeq(1,:)+i*ZL*tan(kL*dL))./(ZL+i.*Zeq(1,:).*tan(kL*dL)));
%Zeq(3,:) =
ZH*((Zeq(2,:)+i*ZH*tan(kH*dH))./(ZH+i.*Zeq(2,:).*tan(kH*dH)));

Zin = ZL*((Zeq(NumLayers-1,:) + i*ZL.*tan(kL*d(6))./(ZL +
i*Zeq(NumLayers-1,:).*tan(kL*d(6))));

S11 = (Zin-1)./(Zin+1);

plot(f,abs(S11))
```

APPENDIX B: ELECTRODE CONFIGURATIONS IMPLEMENTED

Four mask designs were required to reach the electrode design implemented as a biosensor. These are referred to as LFE0, LFE1, LFE2 and LFE3. A final LFE4 mask has been implemented for use with the AcμRay System™, though testing is still on-going regarding this configuration. Provided in this appendix is a full record of all electrode geometries tried.

LFE0

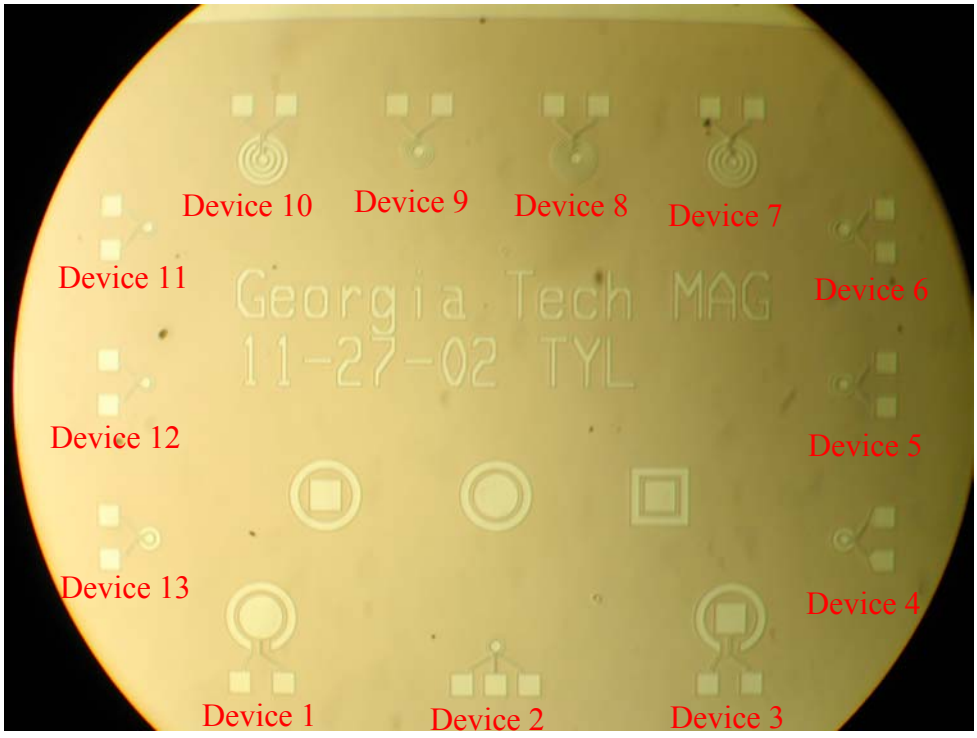

Figure 1. LFE 0 Die, measuring 4mm x 5mm and containing 13 electrode configurations for LFE. Mask designed to fit 204 dice per 3" wafer.

Device 1

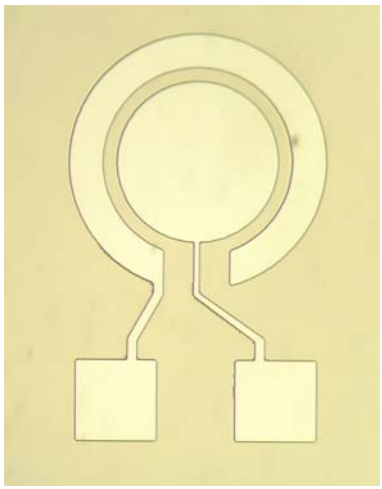

Outer Diameter: 325 μm
Inner Diameter: 240 μm
Center Diameter: 205 μm
Outer Gap: 84 μm
Lead width: 6 μm

Device 2

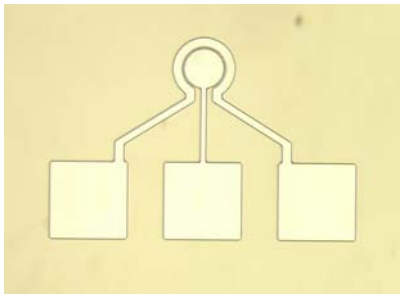

Outer Diameter: 82 μm
Inner Diameter: 60 μm
Center Diameter: 50 μm
Outer Gap: 25 μm

Device 3

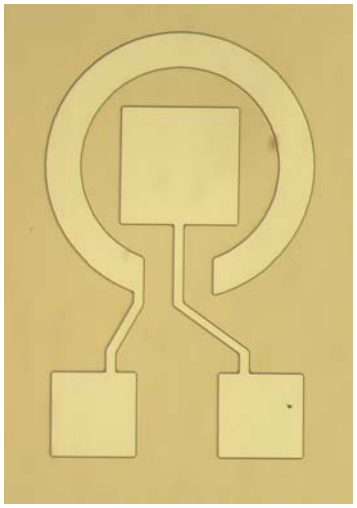

Outer Diameter: 325 μm
Inner Diameter: 240 μm
Square Width: 144 μm
Outer Gap: 85 μm
Lead Width: 6 μm

Device 4

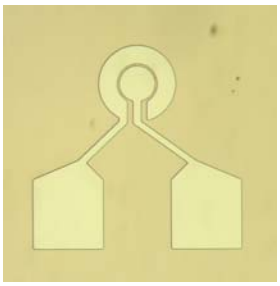

Outer Diameter: 112.5 µm
Inner Diameter: 58.75 µm
Center Diameter: 51 µm
Outer Gap: 28.75 µm
Lead Width: 6 µm

Device 5

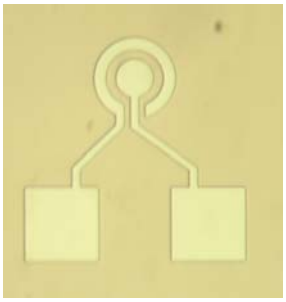

Outer Diameter: 112.5 µm
Inner Diameter: 78.75 µm
Center Diameter: 52.5 µm
Outer Gap: 28.75 µm
Lead Width: 6 µm

Device 6

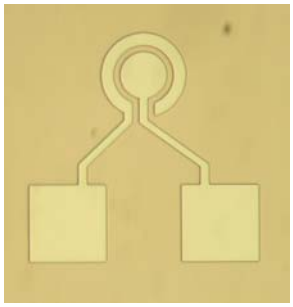

Outer Diameter: 112.5 µm
Inner Diameter: 80 µm
Center Diameter: 62 µm
Outer Gap: 28.75 µm
Lead Width: 6 µm

Device 7

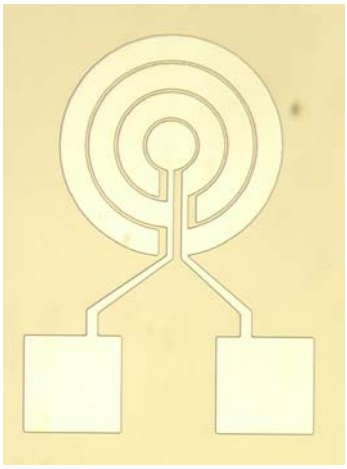

4 Outer Diameter: 206 µm
4 Inner Diameter: 180 µm
3 Outer Diameter: 163 µm
3 Inner Diameter: 120 µm
2 Outer Diameter: 112 µm
2 Inner Diameter: 58.75 µm
1 Diameter: 52.5 µm
Lead Gap: 7.5 µm
End Gap: 6 µm
Lead Width: 6 µm

Device 8

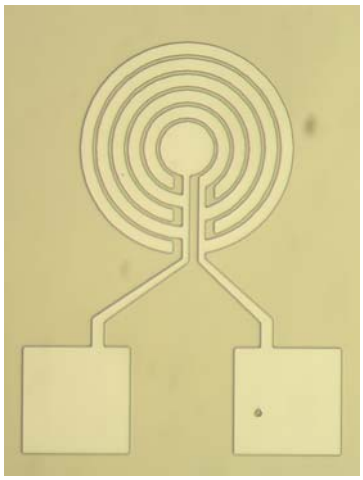

6 Outer Diameter: 205 µm
6 Inner Diameter: 180 µm
5 Outer Diameter: 170 µm
5 Inner Diameter: 150 µm
4 Outer Diameter: 140 µm
4 Inner Diameter: 120 µm
3 Outer Diameter: 110 µm
3 Inner Diameter: 90 µm
2 Outer Diameter: 80 µm
2 Inner Diameter: 60 µm
1 Diameter: 50 µm
Lead Gap: 10 µm
End Gap: 10 µm
Lead Width: 6 µm

Device 9

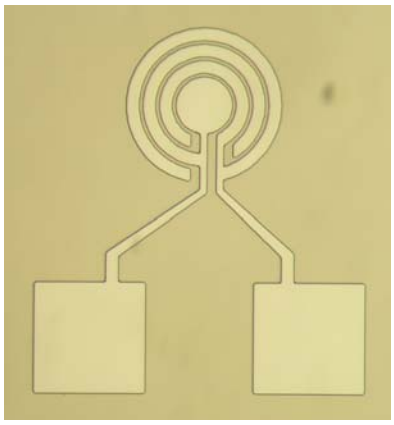

4 Outer Diameter: 142 µm
4 Inner Diameter: 120 µm
3 Outer Diameter: 110 µm
3 Inner Diameter: 90 µm
2 Outer Diameter: 80 µm
2 Inner Diameter: 60 µm
1 Diameter: 50 µm
Lead Gap: 10 µm
End Gap: 8 µm
Lead Width: 6 µm

Device 10

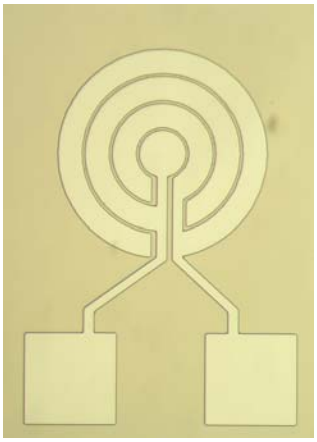

4 Outer Diameter: 230 µm
4 Inner Diameter: 180 µm
3 Outer Diameter: 172 µm
3 Inner Diameter: 120 µm
2 Outer Diameter: 112 µm
2 Inner Diameter: 60 µm
1 Diameter: 52 µm
Lead Gap: 6 µm
End Gap: 6 µm
Lead Width: 12 µm

Device 11

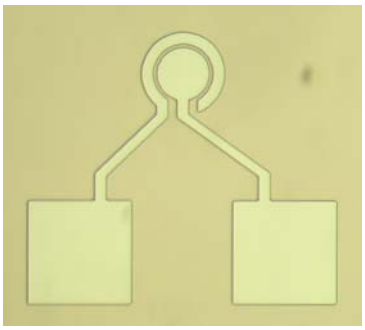

Outer Diameter: 82 μm
Inner Diameter: 60 μm
Center Diameter: 50 μm
Outer Gap: 28 μm
Lead Width: 10 μm

Device 12

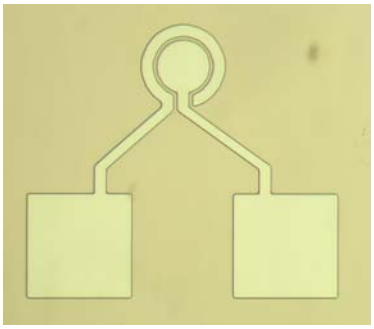

Outer Diameter: 82 μm
Inner Diameter: 60 μm
Center Diameter: 50 μm
Outer Gap: 20 μm
Lead Width: 10 μm

Device 13

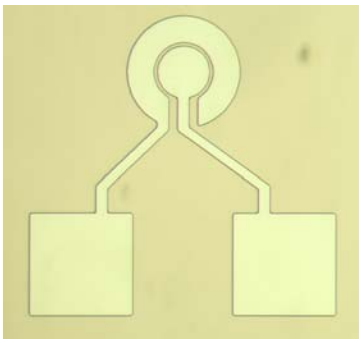

Outer Diameter: 104 μm
Inner Diameter: 60 μm
Center Diameter: 50 μm
Outer Gap: 28 μm
Lead Width: 10 μm

LFE1

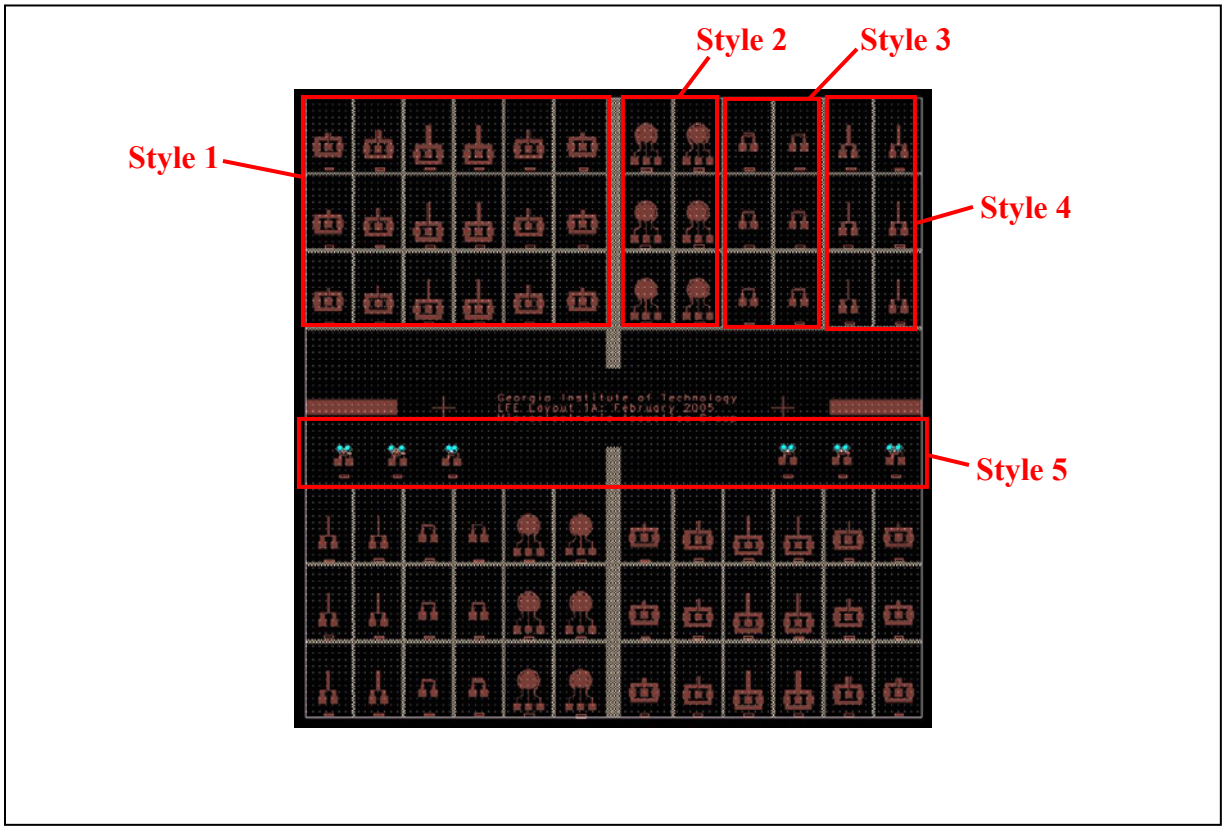

Figure 2. LFE I Die which includes 42 different electrode configurations that could be superimposed to form a 2-layer electrode configuration for more efficient LFE. Die measures 10 mm x 10 mm, arranged to fit 36 dice per photo-mask.

Style 1

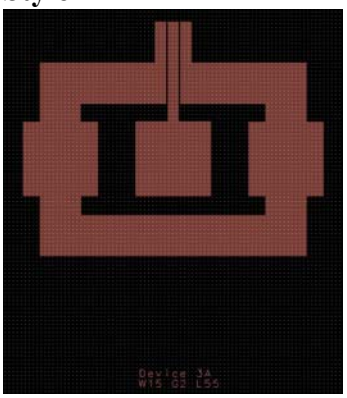

Electrode width = 10, 15, 25 µm
Electrode gap = 2, 3, 4, 5 µm
Electrode length = 55, 110, 250 µm

Style 2

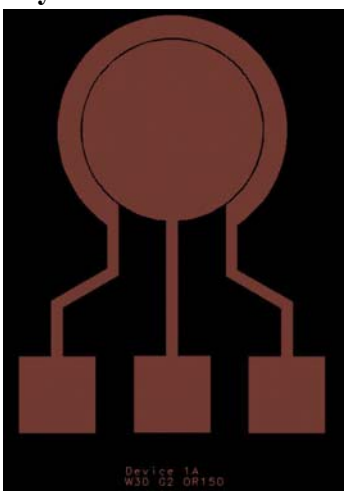

Outer electrode width (Signal) = 20, 30, 50 μm
Outer electrode diameter = 150 μm
Electrode Gap = 2, 3, 4, 5 μm

Style 3

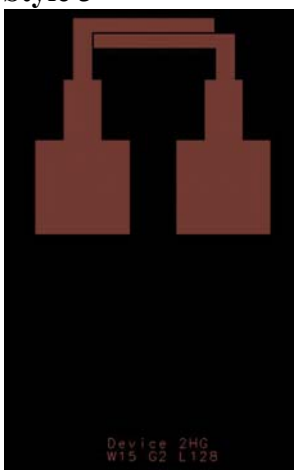

Electrode Width = 15 μm
Electrode Gap = 2, 3, 5 μm
Electrode Length = 128 μm

Style 4

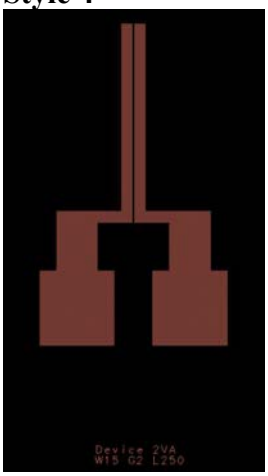

Electrode width = 15 μm
Electrode gap = 2, 3, 5 μm
Electrode length = 250 μm

Style 5

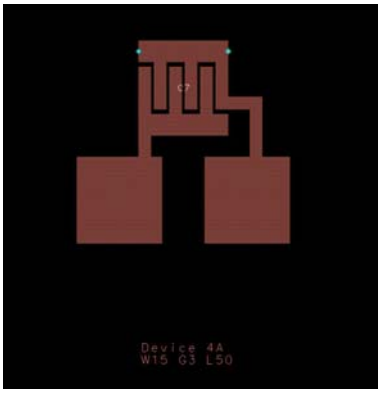

Electrode width = 10, 15, 20, 25 μm
Electrode gap = 2, 3, 4, 5 μm
Electrode length = 50, 150 μm
# of finger pairs = 3, 5

LFE2

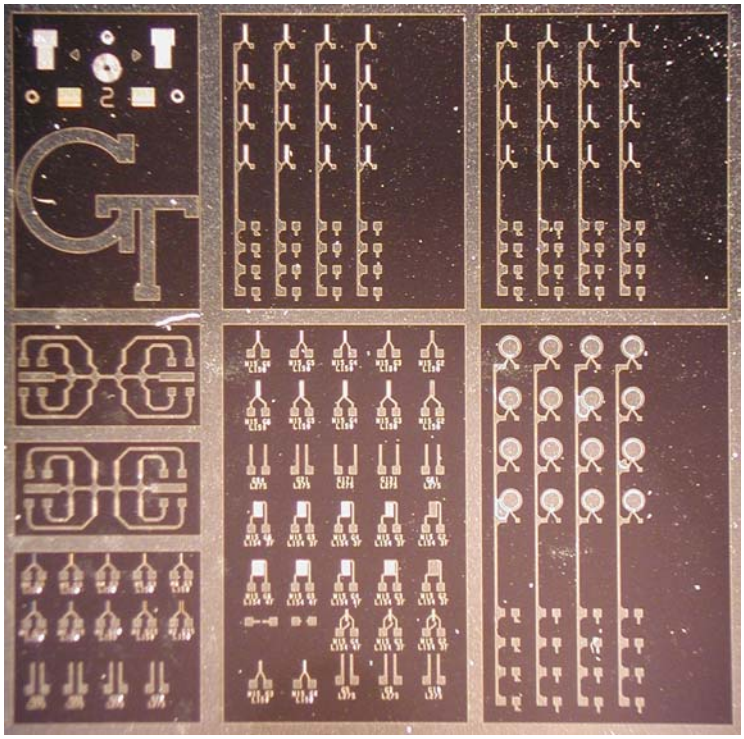

Figure 3. LFE II Die which includes 45 individual electrode configurations and 5 arrayed electrode configurations accounting for an additional 64 devices. Die measures 10 mm x 10 mm, arranged to fit 36 dice per photo-mask.

2-Finger

Electrode width = 15 μm
Electrode gap = 2, 3, 4, 5, 6 μm
Electrode length = 150 μm

3-Finger

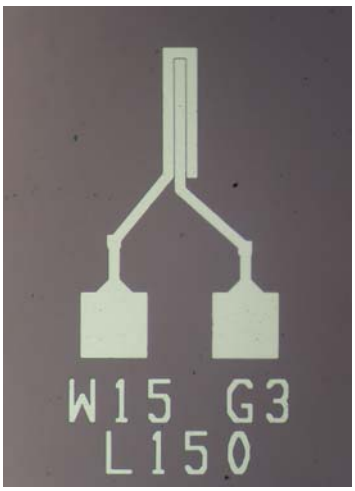

Electrode width = 15 μm
Electrode gap = 2, 3, 4, 5, 6 μm
Electrode length = 150 μm

IDT Electrode

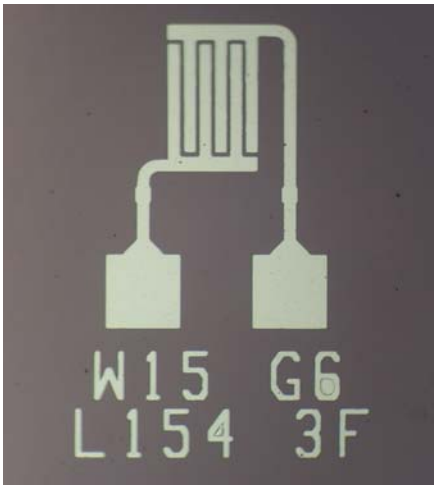

Both 3- and 4-pair IDTs
Electrode width = 15 μm
Electrode gap = 2, 3, 4, 5, 6 μm
Electrode length = 150 μm

Thin 2-Finger

Electrode width = 2, 3, 4, 5 μm
Electrode gap = 3, 10, 15, 20, 25, 35 μm
Electrode length = 150 μm

Slab Electrode

Electrode width = 25 μm
Electrode gap = 3, 5, 10, 21, 61, 94, 131, 171 μm
Electrode length = 275 μm

8-Device Array

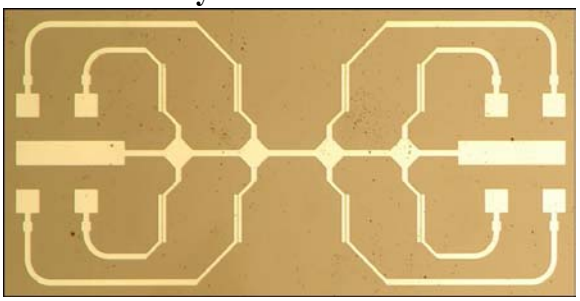

Both 2- and 3-Finger Design
Electrode width = 15 μm
Electrode gap = 3 μm
Electrode length = 150 μm

LFE3

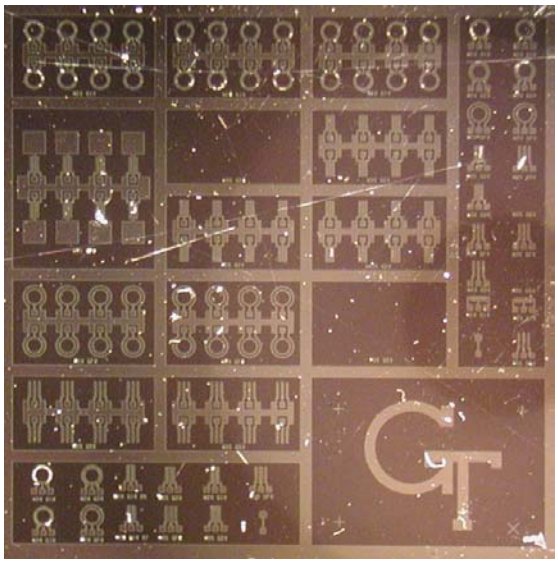

Figure 4. LFE III Die comprising 26 individual devices and 11 8-device arrays. Die measures 10 mm x 10 mm and is arranged to fit 36 die per 3-inch wafer on photo-mask.

Style 1

Electrode Width = 10, 20 μm
Electrode Gap = 10, 20, 40 μm

Style 2

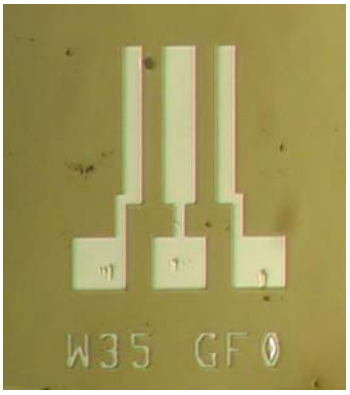

Electrode Width = 20, 35 μm
Electrode Gap = 10, 20, 40, 50 μm

Style 3

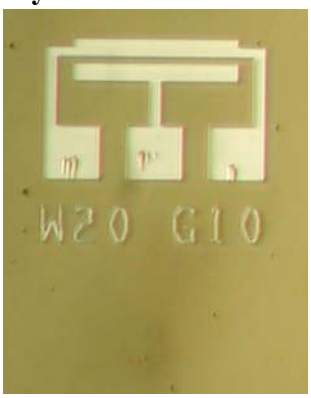

Electrode Width = 20 μm
Electrode Gap = 10 μm

Array Style 1

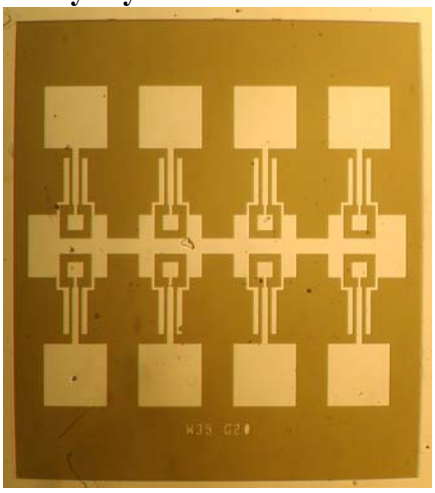

Electrode Width = 35 μm
Electrode Gap = 20 μm
Large squares are surfaces for subsequent wire-bonding

Array Style 2

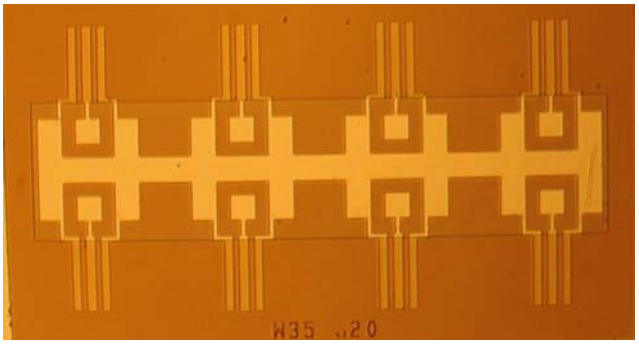

Electrode Width = 35 μm
Electrode Gap = 20, 50 μm

Array Style 3

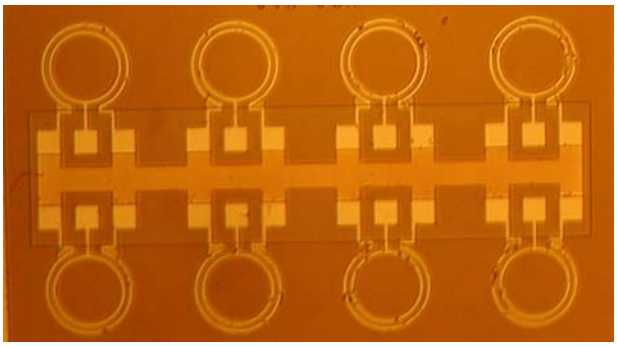

Electrode Width = 20 µm
Electrode Gap = 10, 40 µm

LFE4

4-Device Array

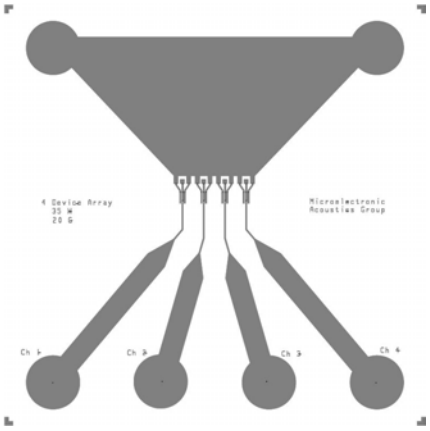

3-Finger Design
Electrode width = 35 µm
Electrode gap = 20 µm
Overall area = 10 mm x 10 mm

8-Device Array

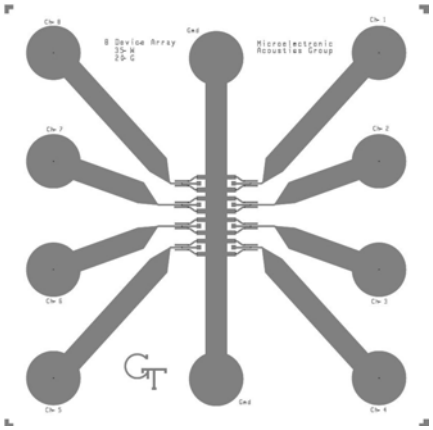

3-Finger Design
Electrode width = 35 µm
Electrode gap = 20 µm
Overall area = 10 mm x 10 mm

APPENDIX C: PHOTOLITHOGRAPHY PROCEDURE

The following materials were used for the photolithography process outlined below:

1. Laurell Technologies Corporation Model WS-200-4NPP Spin Coater
2. Karl Suss MJB3 Mask Aligner
3. Thermolyne Type 1900 Hot Plate

Photolithography Procedure:

1. Rinse the wafer with the following: TCE (Trichloroethylene), Acetone, Methanol, Isopropanol, DI H_2O.
2. Blow both sides dry with N_2 gas stream to remove moisture
3. Warm wafer on a heater plate for ~ 1 minute over 100ºC to remove all moisture
4. Load wafer on vacuum chuck of spin coater. Dispense enough 98% HMDS by pipette to cover entire wafer. Spin the wafer with 98% HMDS at 4000 rpm for 30 seconds at maximum acceleration.
5. Soft bake the wafer immediately on hot plate at ~ 180 C for 30 seconds.
6. Cool wafer on cooling block for 1 minute.
7. Load wafer back on vacuum chuck of spin coater. Dispense enough Shipley's 1805 (S1805) photoresist by pipette to cover entire wafer. Spin the wafer with S1805 at 4000 rpm for 30 seconds at maximum acceleration. This should yield a layer of photoresist ~0.5 μm thick uniformly across the wafer, which is adequate for feature sizes greater than 0.8 μm.
8. Soft bake the wafer immediately on hot plate at ~ 180ºC for 60 seconds.

9. Cool wafer on cooling block for 1 minute. This is a critical step.
10. Mount wafer on vacuum chuck of Karl Suss MJB3 mask aligner. Verify wafer is flat on chuck. Load relevant photomask into mask holder of mask aligner and align wafer beneath the mask appropriately. (Physical contact of the wafer with the photomask was essential for adequate yield with the system used)
11. Expose wafer to ~60 mJ of 365 nm UV light. (The system used for these experiments was calibrated to 4 mW, which required 15 seconds exposure time)
12. Remove wafer from the mask aligner and submerge in Chlorobenzene bath for 90 seconds.
13. Completely dry wafer using N_2 gas stream to remove all chlorobenzene. DO NOT expose surface to DI H_2O or any other liquids before next step.
14. Prepare developer solution (5 parts DI H_2O to 1 part Microposit 351 concentrated developer). Submerge wafer in developer solution and manually agitate for 35 – 45 seconds, or until photoresist die begins to "burst out." A practiced eye should be able to discern the point at which the appropriate features of the mask design have been fully resolved (i.e. all undesireable photoresist has been removed) but not over-developed.
15. Immediately rinse the wafer in a stream of DI H_2O.
16. Completely dry wafer using N_2 gas stream to remove water.
17. Hard bake wafer for an additional 60 seconds on hot plate. This also ensures that all water is evaporated from the surface.

APPENDIX D: FUNCTIONALIZATION PROTOCOL

The following equipment was used for the surface functionalization protocol outlined below:

1. Branson Model 2510 Ultrasonic Bath
2. Nitrogen glove box
3. Unifilm PVD-300 Sputtering System – Ion mill tool
4. VWR Scientific Products Standard Shaker
5. VWR Scientific Products mini vortexer
6. VWR 25 mL centrifuge tubes

Crosslinker Immobilization

1. Prepare the 4% MTS primary crosslinking solution by mixing 1 part MTS solution (Fluka) to 24 parts dry Toluene (99.5% A.C.S., Sigma Aldrich) in a sufficiently large centrifuge tube. Mix solution thoroughly using vortexer at greater than medium level for more than 30 seconds.
2. Deposit enough of 4% MTS crosslinker solution into appropriate sealed containers to accommodate samples. (For the purposes of these experiments, 3-4 mL was deposited in to 50 mL centrifuge tubes from VWR which accommodated 1 cm × 1 cm wafer chips)

3. Rinse the ZnO coated surfaces with the following: TCE (Trichloroethylene), Acetone (VWR, BDH), Methanol (ultra, J.T. Baker), Isopropanol (VWR, BDH), DI H_2O (Aristar Plus, VWR, BDH).
4. Blow both sides dry with N_2 gas stream to remove moisture
5. Warm samples on a heater plate for ~ 1 minute over 100ºC to remove all moisture
6. Load samples using carbon tape to secure them onto platform surface to be placed on planet 5 of the Unifilm PVD-300 sputtering system.
7. Using loadlock, load platform onto planet 5 of the Unifilm system.
8. Run program to ion mill surfaces using 9 mA beam current for 5 minutes.
9. IMMEDIATELY submerge each ZnO coated sample individually into containers with 4% MTS crosslinker solution and immediately seal. It is EXTREMELY IMPORTANT to minimize exposure time of the samples to air after removing them from the vacuum environment of the ion mill before submerging them in MTS solution.
10. Allow samples to incubate for 24 hours.
11. Prepare 1 mM GMBS (Fluka) solution in ethanol (95%, Fisher) at least 2 hours prior to using. 1mM GMBS solution was allowed to mix for 2 hours on a shake table at medium speed, or until all granules of GMBS were no longer visible in the solution. Again prepare enough of 1 mM GMBS solution into appropriate sealed containers to accommodate samples. (3-4 mL in 50 mL centrifuge tubes)
12. Remove samples from 4% MTS solution and rinse using stream of ethanol for several seconds.

13. Submerge samples in a small buoyant container with sufficient ethanol to cover the samples and place in ultrasonic bath for 5 minutes.
14. Remove sample from sonication bath and deposit in 1 mM GMBS solution and seal. Allow samples to incubate for 24 hours.
15. Remove samples from 1 mM GMBS solution and rinse using stream of ethanol for several seconds.
16. Submerge samples in a small buoyant container with sufficient ethanol to cover the samples and place in ultrasonic bath for 5 minutes.
17. Samples are now prepared for IgG immobilization.

Antibody Immobilization

18. Immediately after ethanol sonication, dry samples with N_2 gas stream and deposit 200 μg/mL solution of IgG antibodies by pipette onto surface of sample. (For the experiments described in this thesis, 30 μL was sufficient)
19. Allow Ab solution to incubate on surface for 4 hours.
20. Rinse surface with PBS buffer stream.
21. Samples are now functionalized and ready for exposure to liquid sample for detection.

APPENDIX E: MATLAB CODE – PIEZOELECTRIC TA_2O_5

```
%Calculations defined for Z directed propagation li][0 0 1]
%Assumed Class of 2mm for Ta2O5
%Written by Christopher Corso

% syms lx ly lz;
% lLj = [0 0 0; 0 0 0; 0 0 1; 0 1 0; 1 0 0; 0 0 0]; %Set this according
        to direction of propagation
% liJ= [0,0,0,0,1,0;0,0,0,1,0,0;0,0,1,0,0,0]; %Also set this according
       to direction of propagation

syms c11 c12 c13 c23 c33 c44 c55 c66 e14 e25 e36 e15 e24 e33 e32 e31
     lex ley lez epsxx epsyy epszz;
% stiffness= [c11,c12,c13,0,0,0; c12,c11,c23,0,0,0; c13,c23,c33,0,0,0;
             0,0,0,c44,0,0; 0,0,0,0,c55,0; 0,0,0,0,0,c66]; %Stiffness
             Tensor for Orthorhombic

% lj=[0; 0; 1]; %Set this according to direction of propagation
% li=[0 0 1]; %Set this according to direction of propagation
% Efieldj=[lex; ley; 0]; %direction of electric field in x y plane
% Efieldi=[lex ley 0]; %direction of electric field in x y plane

piezoiL=[0,0,0,e14,0,0;0,0,0,0,e25,0;0,0,0,0,0,e36]; %defined for class
        222
piezoKj=[0,0,0;0,0,0;0,0,0;e14,0,0;0,e25,0;0,0,e36]; %defined for class
        222

% permittivity=[epsxx, 0, 0; 0, epsyy, 0; 0, 0, epszz]; %Perittivity
% top=piezoKj*Efieldj*Efieldi*piezoiL;
% bottom=Efieldi*permittivity*Efieldj;
% piez=top/bottom;
% stiffened=stiffness+piez;
% christoffel=liJ*stiffened*lLj

%Above Calculations Redone for Assumed class 2mm Ta2O5
%

%Declaration of euler angles for rotation of matrices
rotation=1;       % 1 if rotation to be carried out, 0 if not
phi=0;            % clockwise rotation around z axis
theta=-275.216;   % clockwise rotation around new y axis
psi=0;            % clockwise rotation around new z axis

%Declaration of rest of variables
syms lx ly lz;
lLj = [0 0 0; 0 0 0; 0 0 1; 0 1 0; 1 0 0; 0 0 0]; %Set this according
to direction of propagation
liJ= [0,0,0,0,1,0;0,0,0,1,0,0;0,0,1,0,0,0]; %Also set this according to
direction of propagation

%lLj = [1 0 0; 0 0 0; 0 0 0; 0 0 0; 0 0 1; 0 1 0]; %Set this according
to direction of propagation
%liJ= lLj'; %Also set this according to direction of propagation
```

```
syms c11 c12 c13 c23 c33 c44 c55 c66 e14 e25 e36 e15 e24 e33 e32 e31
     lex ley lez epsxx epsyy epszz;

stiffness= [c11,c12,c13,0,0,0; c12,c11,c23,0,0,0; c13,c23,c33,0,0,0;
           0,0,0,c44,0,0; 0,0,0,0,c55,0; 0,0,0,0,0,c66]; %Stiffness
           Tensor for Orthorhombic

%lj=[0; 0; 1]; %Set this according to direction of propagation
%li=[0 0 1]; %Set this according to direction of propagation

Efieldj=[1; 0; 0]; %Arbitrary direction of electric field
Efieldi=[1 0 0]; %Arbitrary direction of electric field

%piezoiL=[0,0,0,0,e15,0;0,0,0,e24,0,0;e31,e32,e33,0,0,0]; %defined for
         class 222
%piezoKj=[0,0,e31;0,0,e32;0,0,e33;0,e24,0;e15,0,0;0,0,0]; %defined for
         class 222
permittivity=[epsxx, 0, 0; 0, epsyy, 0; 0, 0, epszz]; %Perittivity

if rotation==1;
    Mphi= [cosd(phi)^2 sind(phi)^2 0 0 0 sind(2*phi); sind(phi)^2
           cosd(phi)^2 0 0 0 -sind(2*phi); 0 0 1 0 0 0; 0 0 0
           cosd(phi) -sind(phi) 0; 0 0 0 sind(phi) cosd(phi) 0; -
           sind(2*phi)/2 sind(2*phi)/2 0 0 0 cosd(2*phi)];
    Mtheta= [cosd(theta)^2 0 sind(theta)^2 0 -sind(2*theta) 0; 0 1 0 0
           0 0; sind(theta)^2 0 cosd(theta)^2 0 sind(2*theta) 0; 0 0 0
           cosd(theta) 0 sind(theta); sind(2*theta)/2 0 -
           sind(2*theta)/2 0 cosd(2*theta) 0; 0 0 0 -sind(theta) 0
           cosd(theta)];
    Mpsi= [cosd(psi)^2 sind(psi)^2 0 0 0 sind(2*psi); sind(psi)^2
           cosd(psi)^2 0 0 0 -sind(2*psi); 0 0 1 0 0 0; 0 0 0
           cosd(psi) -sind(psi) 0; 0 0 0 sind(psi) cosd(psi) 0; -
           sind(2*psi)/2 sind(2*psi)/2 0 0 0 cosd(2*psi)];
    MphiPrime=Mphi';
    MthetaPrime=Mtheta';
    MpsiPrime=Mpsi';
    aphi= [cosd(phi) sind(phi) 0; -sind(phi) cosd(phi) 0; 0 0 1];
    atheta= [cosd(theta) 0 -sind(theta); 0 1 0; sind(theta) 0
           cosd(theta)];
    apsi= [cosd(psi) sind(psi) 0; -sind(psi) cosd(psi) 0; 0 0 1];
    aphiPrime=aphi';
    athetaPrime=atheta';
    apsiPrime=apsi';

    stiffnessrotated=Mpsi*Mtheta*Mphi*stiffness*MphiPrime*MthetaPrime*Mp
           siPrime;

    piezoiLrotated=apsi*atheta*aphi*piezoiL*MphiPrime*MthetaPrime*MpsiPr
           ime;

    permittivityrotated=apsi*atheta*aphi*permittivity*aphiPrime*athetaPr
           ime*apsiPrime;

    piezoKjrotated=conj(piezoiLrotated');
    top=piezoKjrotated*Efieldj*Efieldi*piezoiLrotated;
    bottom=Efieldi*permittivityrotated*Efieldj;
```

```
    piez=top/bottom;
    stiffened=stiffnessrotated+piez;
    christoffel=liJ*stiffened*lLj
else
    top=piezoKj*Efieldj*Efieldi*piezoiL;
    bottom=Efieldi*permittivity*Efieldj;
    piez=top/bottom;
    stiffened=stiffness+piez;
    christoffel=liJ*stiffened*lLj
end
```

APPENDIX F: AMERICAN ASSOCIATION OF CANCER RESEARCHERS PRESS RELEASE

A New Technology for Cancer Screening Listens for the Signs of Cancer

ATLANTA – Cancer-sensing devices built as cheaply and efficiently as wristwatches – using many of the same operating principles – could change the way clinicians detect, treat and monitor cancer in patients. Researchers from the Georgia Institute of Technology have created an acoustic sensor that can report the presence of small amounts of mesothelin, a molecule associated with a number of cancers including mesothelioma, as they attach to the sensor's surface.

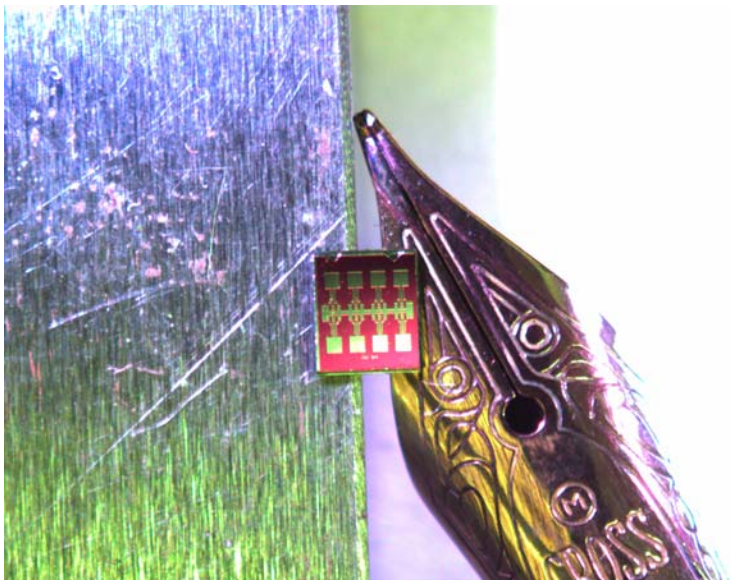

According to the researchers, the study is a proof of principle, demonstrating a technique that might work for the detection of nearly any biomarker – a collective term for a molecular signal that denotes the presence of disease. They present their findings today in Atlanta, Georgia at the American Association for Cancer Research's 2nd Annual International Conference on Molecular Diagnostics in Cancer Therapeutic Development.
"It is one thing to be able to identify biomarkers for a disease, but it is another to be able to find them in blood quickly and easily at very low concentrations," said Anthony Dickherber, a graduate student in the School of Electrical and Computer Engineering at Georgia Tech. "We envision that, one day, doctors can use an array of our sensors as a sort of laboratory in their office, where they could use a quick blood sample to detect or monitor the signs of cancer."

According to Dickherber, such a device would be a boon to healthcare practice, allowing physicians to screen patients for signs of disease before opting for more expensive or invasive diagnostic techniques. Responding to the growing need for such sensors in both research and clinical practice, Dickherber, along with fellow Georgia Tech graduate student Christopher Corso and research adviser William D. Hunt, Ph.D., conceived of and developed the ACµRay™ (pronounced *ak´-u-rā*) chip, standing for ACoustic micro-arRAY – a device that shares more in common with an inexpensive wristwatch than the sort of cutting edge molecule-sorting apparatuses currently used by researchers and clinical laboratory technicians.

The array consists of a series of electrodes deposited on the surface of a thin film of zinc oxide, which allows the device to resonate, or vibrate, at a specific frequency when a current is applied, much like the quartz timing devices used in many clocks and watches. "The sensor itself is built on a base of silicon, like a computer chip, and could be mass-produced using very well known and inexpensive microelectronic fabrication techniques," Dickherber said.

To turn this array into a sensor, the Georgia Tech researchers coated the zinc oxide surface with mesothelin-specific antibodies generated in the lab of Ira Pastan, M.D., at the National Cancer Institute. These molecules are engineered versions of the antibodies the immune system creates to identify foreign intruders, such as microbial parasites. In this study, the researchers coated the sensor with antibodies for mesothelin, a cell-surface protein that is highly expressed in mesothelioma, ovarian cancer, pancreatic cancer and other malignancies.

When the mesothelin binds to an antibody, the added mass changes the frequency at which the acoustic wave passes between the electrodes on the surface of the device. The device is able to "hear" the pitch change due to nanomolar concentrations of mesothelin (just a few molecules amid billions) binding to antibodies on the chip. The technology has the potential of detecting biomarkers in even lower concentrations than those tested, Dickeherber said.

"It is really an elegant engineering solution to a very complicated problem," said Hunt, a professor of electrical and computer at Georgia Tech and lead researcher on the project. "With refinement, this technology could readily lead to an inexpensive, ubiquitous technology for researchers, physicians and the clinical laboratory."

This research is supported by grants from the U.S. Army Medical Research & Materiel Command Prostate Cancer Research Program, the National Science Foundation, The V Foundation, the National Cancer Institute and the Georgia Cancer Coalition.

>>>>>

AACR 2007 Conference on Molecular Diagnostics in Cancer Therapeutic Development

September 17-20th, Atlanta, Ga.

Coverage for Tony Dickherber, Christopher Corso, and William Hunt "A New Technology for Cancer Screening Listens for the Signs of Cancer"*

From our press release:
RxPG News
http://www.rxpgnews.com/research/A-new-technology-for-cancer-screening-listens-for-the-signs-of-cancer_64056.shtml

Dentalplans.com
http://www.dentalplans.com/articles/25102/

PhysOrg.com
http://www.physorg.com/news109349930.html

ScienceDaily
http://www.sciencedaily.com/releases/2007/09/070918144313.htm

Original Stories:

WebMD (Dan DeNoon)
"Sensor Hears Cancer's Call; Tiny Biosensors Detect 'Song' of Cancer Markers, Say Researchers"
http://www.webmd.com/cancer/news/20070918/sensor-hears-cancers-call

From the WebMD story above:
Medicine.net
http://www.medicinenet.com/script/main/art.asp?articlekey=83974

From the Amanda Gardner HealthDay story "Tiny Sensor Could Spot Cancer Early":

CBC News
http://www.cbc.ca/cp/HealthScout/070918/6091806AU.html

Health Central.com
http://www.healthcentral.com/newsdetail/408/608331.html

WFIE 14 Indiana (NBC affiliate)
http://www.14wfie.com/Global/story.asp?S=7094493&nav=3w6r

LEX 18 Kentucky (NBC affiliate)
http://www.lex18.com/Global/story.asp?S=7094493&nav=EQls

Forbes
http://www.forbes.com/forbeslife/health/feeds/hscout/2007/09/18/hscout608331.html

US News & World Report
http://health.usnews.com/usnews/health/healthday/070918/tiny-sensor-could-spot-cancer-early.htm

Dentalplans.com
http://www.dentalplans.com/articles/25095/

Health Scout
http://www.healthscout.com/news/1/608331/main.html

HealthCentral.com
http://www.healthcentral.com/newsdetail/408/608331.html

KOLD News Arizona (CBS Affiliate)
http://www.kold.com/global/story.asp?s=7094493

CNN News Room

September 19, 2007 Wednesday
SHOW: CNN NEWSROOM 3:00 PM EST
Bail Set For O.J. Simpson; Ahmadinejad to Visit Ground Zero?; Al Sharpton's Planned Protest in Jena, Lousiana
BYLINE: Joe Johns, Paul Vercammen, Deborah Feyerick, Susan Roesgen, Ed Lavandera, Don Lemon, Fredricka Whitfield, Jeffrey Toobin, Sanjay Gupta, Susan Lisovicz, Wolf Blitzer
SECTION: NEWS; International

WHITFIELD: Straight ahead, a high tech computer chip smaller than a penny that can detect cancer. Details on that straight ahead in "THE NEWSROOM".

WHITFIELD: A computer chip could one day make diagnosing cancer as easy as telling time.

Here's CNN's chief medical correspondent, Dr. Sanjay Gupta.

DR. SANJAY GUPTA, CNN CORRESPONDENT: This is something that really fascinates me quite a bit. This is a little chip that I'm holding up here. I'm actually holding it in a pair of tweezers this thing is so small. It's called the ACuRay and it's not something that's going to be widely available quite yet. But researchers have been focusing on this particular chip as a way to detect cancer very, very early.

Again, it's called the ACuRay. You can take at it there. What it is specifically is 140 different electrodes actually bound together by zinc oxide. The theory a simple one -- basically, if you have cancer molecules in your blood and you wash your blood over the sensor, the way that those cancer molecules bind to this

ACuRay gives off a certain resonance, a certain frequency that can be measured. If you have cancer molecules, it's going to sound different than if you don't have cancer molecules in your blood. The whole idea is that you want to detect cancer as early as possible.

Now what does this all mean?

There could be a day when doctors have several different little devices like this in their office and you walk in, you give a drop of blood and they immediately screen to tell if you have any cancer molecules in your bloodstream. It could be used, perhaps, in the future for infectious diseases, as well.

Again, as I mentioned, it's not something we may see in our lifetimes as a general way of practicing, but this whole idea you might be able to find cancer early, earlier than ever before, before it shows up on a C.T. scan or an MRI, when it's just a few still a few molecules in your blood is sort of the holy grail of cancer detection and screening.

Could this be the answer?

Possibly one day. It's something that we're certainly going to keep an eye on -- back to you.

LEMON: All right, Sanjay.

It's time now to check in with CNN's Wolf Blitzer.

WHITFIELD: Yes, in "THE SITUATION ROOM" -- what do you have on tap?

WOLF BLITZER, HOST, "THE SITUATION ROOM": All right, guys, thanks very much.

The Republican presidential candidate, Rudy Giuliani, has a message for MoveOn.org -- bring it on. He talks about his high profile spat with the liberal anti-war group in an exclusive one-on-one interview with our chief national correspondent, John King. That's coming up.

Also, Reverend Jesse Jackson says Democratic presidential candidate Barack Obama -- and I'm quoting now -- "is acting like he's white." We'll show you what's behind that controversial comment.

Also, carefree lives in the face of unimaginable suffering. There are some disturbing newly released images of the men and women who ran the Nazi Auschwitz death camp. All that and a lot more coming up right here in "THE SITUATION ROOM" -- back to you.

LEMON: All right, Wolf, we'll be watching.

Thank you. WHITFIELD: All right, the closing bell and a wrap of the action on Wall Street straight ahead.

REFERENCES

[1] E. Dominguez and S. Alcock, "Sensing technologies for contaminated sites and groundwater," *Biosensors and Bioelectronics*, vol. 17, pp. 625-633, 2002.

[2] B. M. Paddle, "Biosensors for chemical and biological agents of defence interest," *Biosensors and Bioelectronics*, vol. 11, pp. 1079-1113, 1996.

[3] D. D. Stubbs, S. H. Lee, and W. D. Hunt, "Investigation of Cocaine Plumes Using Surface Acoustic Wave Immunoassay Sensors," *Anal. Chem.*, vol. 75, pp. 6231-6235, 2003.

[4] N. C. Institute, "Cancer Facts & the War on Cancer," 2008.

[5] A. Jemal, R. Siegel, E. Ward, T. Murray, J. Xu, and M. J. Thun, "Cancer Statistics, 2007," *CA Cancer J Clin*, vol. 57, pp. 43-66, 2007.

[6] R. Etzioni, N. Urban, S. Ramsey, M. McIntosh, S. Schwartz, B. Reid, J. Radich, G. Anderson, and L. Hartwell, "The Case for Early Detection," *Nature Reviews: Cancer*, vol. 1, pp. 243-252, 2003.

[7] Niroshan Ramachandran, D. N. Larson, P. R. H. Stark, E. Hainsworth, and J. LaBaer, "Emerging tools for real-time label-free detection of interactions on functional protein microarrays," *FEBS Journal*, vol. 272, pp. 5412-5425, 2005.

[8] M. Uttamchandani and S. Q. Yao, "Peptide Microarrays: Next Generation biochips for Detection, Diagnostics and High-Throughput Screening," *Current Pharmaceutical Design*, vol. 14, pp. 000-000, 2008.

[9] J. Wang, "Electrochemical biosensors: Towards point-of-care cancer diagnostics," *Biosensors and Bioelectronics*, vol. 21, pp. 1887-1892, 2006.

[10] S. A. Soper, K. Brown, A. Ellington, B. Frazier, G. Garcia-Manero, V. Gau, S. I. Gutman, D. F. Hayes, B. Korte, J. L. Landers, D. Larson, F. Ligler, A. Majumdar, M. Mascini, D. Nolte, Z. Rosenzweig, J. Wang, and D. Wilson, "Point-of-care biosensor systems for cancer diagnostics/prognostics," *Biosensors and Bioelectronics*, vol. 21, pp. 1932-1942, 2006.

[11] S. Kumar, A. Mohan, and R. Guleria, "Biomarkers in cancer screening, research and detection: present and future: a review," *Biomarkers: Biochemical Indicators Of Exposure, Response, And Susceptibility To Chemicals*, vol. 11, pp. 385-405, 2006.

[12] T. J. Kindt, R. A. Goldsby, B. A. Osborne, and J. Kuby, *Immunology*, 6th ed. New York: W.H. Freeman, 2007.

[13] X. Fan, I. M. White, S. I. Shopova, H. Zhu, J. D. Suter, and Y. Sun, "Sensitive optical biosensors for unlabeled targets: A review," *Analytica Chimica Acta*, vol. 620, pp. 8-26, 2008.

[14] X. Gao, Y. Cui, R. M. Levenson, L. W. K. Chung, and S. Nie, "In vivo cancer targeting and imaging with semiconductor quantum dots," *Nat Biotech*, vol. 22, pp. 969-976, 2004.

[15] D. A. Hall, J. Ptacek, and M. Snyder, "Protein microarray technology," *Mechanisms of Ageing and Development*, vol. 128, pp. 161-167, 2007.

[16] I. Abdulhalim, M. Zourob, and A. Lakhtakia, "Surface plasmon resonance for biosensing: A mini-review," *Electromagnetics*, vol. 28, pp. -, 2008.

[17] M. Uttamchandani and S. Q. Yao, "Peptide Microarrays: Next Generation Biochips for Detection, Diagnostics and High-Throughput Screening," *Current Pharmaceutical Design*, vol. 14, 2008.
[18] C. Z. Rosen, B. V. Hiremath, and R. E. Newnham, *Piezoelectricity*. New York: American Institute of Physics, 1992.
[19] L. Woo Wai, S. Yonghua, and K. Eun Sok, "Lateral-field-excitation acoustic resonators for monolithic oscillators and filters," *Frequency Control Symposium, 1996. 50th., Proceedings of the 1996 IEEE International.*, pp. 558-562, 1996.
[20] J. F. Rosenbaum, *Bulk acoustic wave theory and devices*. Boston: Artech House, 1988.
[21] J. Kondoh, Y. Okiyama, S. Mikuni, Y. Matsui, H. Yatsuda, and M. Nara, "Development of SH-SAW Sensing System for Liquids," presented at Frequency Control Symposium, 2007 Joint with the 21st European Frequency and Time Forum. IEEE International, 2007.
[22] E. Berkenpas, S. Bitla, P. Millard, and M. P. da Cunha, "Pure shear horizontal SAW biosensor on langasite," *Ieee Transactions on Ultrasonics Ferroelectrics and Frequency Control*, vol. 51, pp. 1404-1411, 2004.
[23] D. W. Branch and S. M. Brozik, "Low-level detection of a Bacillus anthracis simulant using Love-wave biosensors on 36 degrees YX LiTaO3," *Biosensors & Bioelectronics*, vol. 19, pp. 849-859, 2004.
[24] T. Kogai and H. Yatsuda, "3F-3 Liquid Sensor Using SAW and SH-SAW on Quartz," presented at Ultrasonics Symposium, 2006. IEEE, 2006.
[25] G. Sauerbrey, "Use of quartz vibrator for weighing thin films on a microbalance," *Z. Physik*, vol. 155, pp. 17, 1959.
[26] K. K. Kanazawa and J. G. Gordon, "Frequency of a Quartz Microbalance in Contact with Liquid," *Analytical Chemistry*, vol. 57, pp. 1770-1771, 1985.
[27] K. K. Kanazawa, "QCM physical theory extended to include liquid immersion," Honolulu, HI, USA, 1999.
[28] W. D. Hunt, D. D. Stubbs, and S. H. Lee, "Time-dependent Signatures of Acoustic Wave Biosensors," *Proceedings of the IEEE*, vol. 91, pp. 12, 2003.
[29] D. L. Smith, *Thin-film deposition : principles and practice*. New York: McGraw-Hill, 1995.
[30] S. L. Pinkett, W. D. Hunt, B. P. Barber, and P. L. Gammel, "Determination of ZnO temperature coefficients using thin film bulk acoustic wave resonators," *Ultrasonics, Ferroelectrics and Frequency Control, IEEE Transactions on*, vol. 49, pp. 1491- 1496, 2002.
[31] K. M. Lakin, G. R. Kline, and K. T. McCarron, "Development of miniature filters for wireless applications," *IEEE Transactions on Microwave Theory and Techniques*, vol. 43, pp. 2933-2939, 1995.
[32] A. Shons, F. Dorman, and J. Najarian, "An immunospecific microbalance," *J Biomed Mater Res*, vol. 6, pp. 565-70, 1972.
[33] X. L. Su and Y. Li, "A self-assembled monolayer-based piezoelectric immunosensor for rapid detection of Escherichia coli O157:H7," *Biosens Bioelectron*, vol. 19, pp. 563-74, 2004.

[34] Z. Y. Wu, G. L. Shen, S. P. Wang, and R. Q. Yu, "Quartz-crystal microbalance immunosensor for Schistsoma-japonicum-infected rabbit serum," *Anal Sci*, vol. 19, pp. 437-40, 2003.
[35] C. D. Corso, D. D. Stubbs, S. H. Lee, M. Goggins, R. H. Hruban, and W. D. Hunt, "Real-time detection of mesothelin in pancreatic cancer cell line supernatant using an acoustic wave immunosensor," *Cancer Detect Prev*, 2006.
[36] J. V. Atanasoff and P. J. Hart, "Dynamical determination of the elastic constants and their temperature coefficients for quartz," *Physical Review*, vol. 59, pp. 85-96, 1941.
[37] R. Bechmann, "Parallel Field Excitation of Thickness Modes of Quartz Plates," *Frequency Control, 14th Annual Symposium on. 1960*, pp. 68-88, 1960.
[38] E. R. Hatch and A. Ballato, "Lateral-Field Excitation of Quartz Plates," *Ultrasonics Symposium, 1983*, pp. 512-515, 1983.
[39] A. W. Warner, "Use of Parallel-Field Excitation in the Design of Quartz Crystal Units," *Frequency Control, 17th Annual Symposium on. 1963*, pp. 248-266, 1963.
[40] W. Pinkham, M. Wark, S. Winters, L. French, D. J. Frankel, and J. F. Vetelino, "A lateral field excited acoustic wave pesticide sensor," *Ultrasonics Symposium, 2005 IEEE*, vol. 4, pp. 2279-2283, 2005.
[41] H. Yihe, L. A. French, Jr., K. Radecsky, M. Pereira da Cunha, P. Millard, and J. F. Vetelino, "A lateral field excited liquid acoustic wave sensor," *IEEE Transactions on Ultrasonics, Ferroelectrics and Frequency Control*, vol. 51, pp. 1373-80, 2004.
[42] C. York, L. A. French, P. Millard, and J. F. Vetelino, "A lateral field excited acoustic wave biosensor," *Ultrasonics Symposium, 2005 IEEE*, vol. 1, pp. 44-49, 2005.
[43] Y. Arntz, J. D. Seelig, H. P. Lang, J. Zhang, P. Hunziker, J. P. Ramseyer, E. Meyer, M. Hegner, and G. Ch, "Label-free protein assay based on a nanomechanical cantilever array," *Nanotechnology*, pp. 86, 2003.
[44] A. Ballato, E. R. Hatch, M. Mizan, and T. J. Lukaszek, "Lateral Field Equivalent Networks and Piezocoupling Factors of Quartz Plates Driven in Simple Thickness Modes," *Ultrasonics, Ferroelectrics and Frequency Control, IEEE Transactions on*, vol. 33, pp. 385-393, 1986.
[45] F. Hook, B. Kasemo, T. Nylander, C. Fant, K. Sott, and H. Elwing, "Variations in Coupled Water, Viscoelastic Properties, and Film Thickness of a Mefp-1 Protein Film during Adsorption and Cross-Linking: A Quartz Crystal Microbalance with Dissipation Monitoring, Ellipsometry, and Surface Plasmon Resonance Study," *Anal. Chem.*, vol. 73, pp. 5796-5804, 2001.
[46] A. Sellborn, M. Andersson, C. Fant, C. Gretzer, and H. Elwing, "Methods for research on immune complement activation on modified sensor surfaces," *Colloids and Surfaces B: Biointerfaces*, vol. 27, pp. 295-301, 2003.
[47] A. Jansoff, H.-J. Galla, and C. Steinem, "Piezoelectric Mass-Sensing Devices as Biosensors - An Alternative to Optical Biosensors?," *Angewandte Chemie International Edition*, vol. 39, pp. 29, 2000.
[48] W. E. Newell, "Face-mounted piezoelectric resonators," *Proceedings of the IEEE*, vol. 53, pp. 575-581, 1965.

[49] K. Wasa, S. Hayakawa, and T. Hada, "Excitation of Shear Mode Elastic Waves in Co-Sputtered ZnO Films," *Sonics and Ultrasonics, IEEE Transactions on*, vol. 21, pp. 298-299, 1974.
[50] S. V. Krishnaswamy, B. R. McAvoy, W. J. Takei, and R. A. Moore, "Oriented ZnO Films for Microwave Shear Mode Transducers," *Ultrasonics Symposium, 1982*, pp. 476-479, 1982.
[51] J. S. Wang and K. M. Lakin, "Sputtered C-Axis Inclined ZnO Films for Shear Wave Resonators," *Ultrasonics Symposium, 1982*, pp. 480-483, 1982.
[52] M. Link, M. Schreiter, J. Weber, R. Gabl, D. Pitzer, R. Primig, W. Wersing, M. B. Assouar, and O. Elmazria, "c-axis inclined ZnO films for shear-wave transducers deposited by reactive sputtering using an additional blind," *Journal of Vacuum Science & Technology A: Vacuum, Surfaces, and Films*, vol. 24, pp. 218-222, 2006.
[53] M. Link, M. Schreiter, J. Weber, R. Primig, D. Pitzer, and R. Gabl, "Solidly mounted ZnO shear mode film bulk acoustic resonators for sensing applications in liquids," *Ultrasonics, Ferroelectrics and Frequency Control, IEEE Transactions on*, vol. 53, pp. 492-496, 2006.
[54] P. Wei, Y. Hongyu, K. Jae Wan, Z. Hao, and K. Eun Sok, "Self-aligned lateral field excitation film acoustic resonator with very large electromechanical coupling [FBAR]," *Frequency Control Symposium and Exposition, 2004. Proceedings of the 2004 IEEE International*, pp. 558-561, 2004.
[55] B. A. Auld, *Acoustic fields and waves in solids*, 2nd ed. Malabar, Fla.: R.E. Krieger, 1990.
[56] T. Nomura and M. Okuhara, "Frequency shifts of piezoelectric quartz crystals immersed in organic liquids," *Analytica Chimica Acta*, vol. 142, pp. 4, 1982.
[57] D. Erickson, S. Mandal, A. H. J. Yang, and B. Cordovez, "Nanobiosensors: optofluidic, electrical and mechanical approaches to biomolecular detection at the nanoscale," *Microfluidics and Nanofluidics*, vol. 4, pp. 33-52, 2008.
[58] P. Boyle, "Prostate specific antigen (PSA) testing as screening for prostate cancer: the current controversy," *Ann Oncol*, vol. 9, pp. 1263-4, 1998.
[59] H. J. de Koning and F. H. Schroder, "PSA screening for prostate cancer: the current controversy," *Ann Oncol*, vol. 9, pp. 1293-6, 1998.
[60] M. McCarthy, "PSA screening said to reduce prostate-cancer deaths, or does it?," *Lancet*, vol. 351, pp. 1563, 1998.
[61] J. S. Jones and E. Klein, "Four no more: The 'PSA Cutoff Era' is Over," *Cleveland Clinic Journal of Medicine*, vol. 75, pp. 30-32, 2008.
[62] S.-L. Yao and G. Lu-Yao, "Understanding and Appreciating Overdiagnosis in the PSA Era," *J. Natl. Cancer Inst.*, vol. 94, pp. 958-960, 2002.
[63] K. Lin, R. Lipsitz, T. Miller, and S. Janakiraman, "Benefits and harms of prostate-specific antigen screening for prostate cancer: an evidence update for the U.S. Preventive Services Task Force," *Ann Intern Med*, vol. 149, pp. 192-9, 2008.
[64] C. B. R. Group, "Early Detection Research Network: Fourth Report," National Cancer Institute 2008.
[65] W. D. Hunt, D. D. Stubbs, and L. Sang-Hun, "Time-dependent signatures of acoustic wave biosensors," *Proceedings of the IEEE*, vol. 91, pp. 890-901, 2003.

[66] K. Lange, F. Bender, A. Voigt, H. Gao, and M. Rapp, "A Surface Acoustic Wave Biosensor Concept with Low Flow Cell Volumes for Label-Free Detection," *Anal. Chem.*, vol. 75, pp. 5561-5566, 2003.
[67] J. Kaitila, M. Ylilammi, J. Molarius, J. Ella, and T. Makkonen, "ZnO based thin film bulk acoustic wave filters for EGSM band," presented at Ultrasonics Symposium, 2001 IEEE, 2001.
[68] Y. Giwan, P. Jae-Don, and P. Hee-Dae, "Characterization of ZnO-based FBAR devices for RF applications," presented at Microwave and Millimeter Wave Technology, 2000, 2nd International Conference on. ICMMT 2000, 2000.
[69] M. Linh, L. Jae-Young, P. Van-Su, and Y. Giwan, "Design and Fabrication of ZnO-Based FBAR Microwave Devices for Mobile WiMAX Applications," *Microwave and Wireless Components Letters, IEEE*, vol. 17, pp. 867-869, 2007.
[70] S. L. Pinkett, W. D. Hunt, B. P. Barber, and P. L. Gammel, "Determination of ZnO temperature coefficients using thin film bulk acoustic wave resonators," *IEEE Trans Ultrason Ferroelectr Freq Control*, vol. 49, pp. 1491-6, 2002.
[71] S. Pinkett, W. Hunt, B. Barber, and P. Gammel, "Broadband characterization of zinc oxide-based solidly mounted resonators," presented at Frequency Control Symposium and PDA Exhibition, 2002. IEEE International, 2002.
[72] A. Ballato, "Bulk and Surface Acoustic Wave Excitation and Network Representation," presented at 28th Annual Symposium on Frequency Control. 1974, 1974.
[73] R. W. Cernosek, S. J. Martin, A. R. Hillman, and H. L. Bandey, "Comparison of lumped-element and transmission-line models for thickness-shear-mode quartz resonator sensors," *Ultrasonics, Ferroelectrics and Frequency Control, IEEE Transactions on*, vol. 45, pp. 1399-1407, 1998.
[74] K. M. Lakin, G. R. Kline, and K. T. McCarron, "High-Q microwave acoustic resonators and filters," *Microwave Theory and Techniques, IEEE Transactions on*, vol. 41, pp. 2139-2146, 1993.
[75] D. K. Cheng, *Field and wave electromagnetics*. Reading, Mass.: Addison-Wesley, 1989.
[76] S. L. Pinkett, "Techniques to facilitate the fabrication of ZnO-based thin film bulk acoustic wave devices," 2003, pp. xvi, 286 leaves.
[77] Y. Nakagawa and T. Okada, "Material Constants of New Piezoelectric Ta2o5 Thin-Films," *Journal of Applied Physics*, vol. 68, pp. 556-559, 1990.
[78] J. H. Hu and R. G. Gordon, "Textured Aluminum-Doped Zinc-Oxide Thin-Films from Atmospheric-Pressure Chemical-Vapor Deposition," *Journal of Applied Physics*, vol. 71, pp. 880-890, 1992.
[79] Y. Kashiwaba, F. Katahira, K. Haga, T. Sekiguchi, and H. Watanabe, "Hetero-epitaxial growth of ZnO thin films by atmospheric pressure CVD method," *Journal of Crystal Growth*, vol. 221, pp. 431-434, 2000.
[80] S. Y. Myong, S. J. Baik, C. H. Lee, W. Y. Cho, and K. S. Lim, "Extremely transparent and conductive ZnO:Al thin films prepared by photo-assisted metalorganic chemical vapor deposition (photo-MOCVD) using AlCl3(6H(2)O) as new doping material," *Japanese Journal of Applied Physics Part 2-Letters*, vol. 36, pp. L1078-L1081, 1997.

[81] K. Ogata, T. Kawanishi, K. Maejima, K. Sakurai, S. Fujita, and S. Fujita, "Improvements of ZnO qualities grown by metal-organic vapor phase epitaxy using a molecular beam epitaxy grown ZnO layer as a substrate," *Japanese Journal of Applied Physics Part 2-Letters*, vol. 40, pp. L657-L659, 2001.
[82] K. Haga, T. Suzuki, Y. Kashiwaba, H. Watanabe, B. P. Zhang, and Y. Segawa, "High-quality ZnO films prepared on Si wafers by low-pressure MO-CVD," *Thin Solid Films*, vol. 433, pp. 131-134, 2003.
[83] D. M. Bagnall, Y. F. Chen, Z. Zhu, T. Yao, S. Koyama, M. Y. Shen, and T. Goto, "Optically pumped lasing of ZnO at room temperature," *Applied Physics Letters*, vol. 70, pp. 2230-2232, 1997.
[84] K. Iwata, P. Fons, S. Niki, A. Yamada, K. Matsubara, K. Nakahara, T. Tanabe, and H. Takasu, "ZnO growth on Si by radical source MBE," *Journal of Crystal Growth*, vol. 214, pp. 50-54, 2000.
[85] M. A. L. Johnson, S. Fujita, W. H. Rowland, W. C. Hughes, J. W. Cook, and J. F. Schetzina, "MBE growth and properties of ZnO on sapphire and SiC substrates," *Journal of Electronic Materials*, vol. 25, pp. 855-862, 1996.
[86] Y. Nakanishi, A. Miyake, H. Kominami, T. Aoki, Y. Hatanaka, and G. Shimaoka, "Preparation of ZnO thin films for high-resolution field emission display by electron beam evaporation," *Applied Surface Science*, vol. 142, pp. 233-236, 1999.
[87] S. H. Bae, S. Y. Lee, B. J. Jin, and S. Im, "Pulsed laser deposition of ZnO thin films for applications of light emission," *Applied Surface Science*, vol. 154, pp. 458-461, 2000.
[88] T. J. Bukowski, K. McCarthy, F. McCarthy, G. Teowee, T. P. Alexander, D. R. Uhlmann, J. T. Dawley, and B. J. J. Zelinski, "Piezoelectric properties of sol-gel derived ZnO thin films," *Integrated Ferroelectrics*, vol. 17, pp. 339-347, 1997.
[89] J. G. E. Gardeniers, Z. M. Rittersma, and G. J. Burger, "Preferred orientation and piezoelectricity in sputtered ZnO films," *Journal of Applied Physics*, vol. 83, pp. 7844-7854, 1998.
[90] Y. Zhang, G. Du, D. Liu, X. Wang, Y. Ma, J. Wang, J. Yin, X. Yang, X. Hou, and S. Yang, "Cyrstal growth of undoped ZnO films on Si substrates under different sputtering conditions," *Journal of Cyrstal Growth*, vol. 243, pp. 439-443, 2002.
[91] J. B. Lee, S. H. Kwak, and H. J. Kim, "Effects of surface roughness of substrates on the c-axis preferred orientation of ZnO films deposited by r.f. magnetron sputtering," *Thin Solid Films*, vol. 423, pp. 262-266, 2003.
[92] D. J. Kang, J. S. Kim, S. W. Jeong, Y. Roh, S. H. Jeong, and J. H. Boo, "Structural and electrical characteristics of R.F. magnetron sputtered ZnO films," *Thin Solid Films*, vol. 475, pp. 160-165, 2005.
[93] H. W. Kim and N. H. Kim, "Structural studies of room-temperature RF magnetron sputtered ZnO films under different RF powered conditions," *Materials Science and Engineering B*, vol. 103, pp. 297-302, 2003.
[94] R. Ondo-Ndong, G. Ferblantier, M. Al Kalfioui, A. Boyer, and A. Foucaran, "Properties of RF magnetron sputtered zinc oxide thin films," *Journal of Crystal Growth*, vol. 255, pp. 130-135, 2003.

[95] J. B. Lee, H. J. Kim, S. G. Kim, C. S. Hwang, S. H. Hong, Y. H. Shin, and N. H. Lee, "Deposition of ZnO thin films by magnetron sputtering for a film bulk acoustic resonator," *Thin Solid Films*, vol. 435, pp. 179-185, 2003.
[96] H. W. Kim and N. H. Kim, "Influence of the substrate on the structural properties of sputter-deposited ZnO films," *Physica Status Solidi a-Applied Research*, vol. 201, pp. 235-238, 2004.
[97] X. H. Li, A. P. Huang, M. K. Zhu, S. L. Xu, J. Chen, H. Wang, B. Wang, and H. Yan, "Influence of substrate temperature on the orientation and optical properties of sputtered ZnO films," *Materials Letters*, vol. 57, pp. 4655-4659, 2003.
[98] P. F. Fewster, *X-ray scattering from semiconductors*, 2nd ed. River Edge, NJ: Imperial College Press, 2003.
[99] S. Kakio, Y. Shimatai, and Y. Nakagawa, "Shear-horizontal-type surface acoustic waves on quartz with Ta2O5 thin film," *Japanese Journal of Applied Physics Part 1-Regular Papers Short Notes & Review Papers*, vol. 42, pp. 3161-3165, 2003.
[100] Y. Nakagawa and Y. Gomi, "Ta2o5-on-Fused-Quartz Temperature-Compensated Saw Delay-Lines," *Ieee Transactions on Ultrasonics Ferroelectrics and Frequency Control*, vol. 33, pp. 331-332, 1986.
[101] Y. Nakagawa, Y. Gomi, and T. Suzuki, "Deposition of Ta2o5 Thin-Film and Application to Saw Devices," *Japanese Journal of Applied Physics Part 1-Regular Papers Short Notes & Review Papers*, vol. 24, pp. 25-27, 1985.
[102] K. Tominaga, R. Muhammet, I. Kobayashi, and M. Okada, "Preparation of (111)-Oriented Beta-Ta2o5 Thin-Films by Chemical Vapor-Deposition Using Metalorganic Precursors," *Japanese Journal of Applied Physics Part 2-Letters*, vol. 31, pp. L585-L587, 1992.
[103] C. Chaneliere, J. L. Autran, R. A. B. Devine, and B. Balland, "Tantalum pentoxide (Ta2O5) thin films for advanced dielectric applications," *Materials Science and Engineering: R: Reports*, vol. 22, pp. 269-322, 1998.
[104] Y. Nakagawa and Y. Gomi, "New piezoelectric Ta₂O₅ thin films," *Applied Physics Letters*, vol. 46, pp. 139-40, 1985.
[105] Y. Nakagawa, Y. Gomi, and T. Okada, "Deposition of new piezoelectric Ta_2O_5 thin films and their surface acoustic-wave properties," *Journal of Applied Physics*, vol. 61, pp. 5012-17, 1987.
[106] S. Kakio, M. Nozawa, and Y. Nakagawa, "Propagation characteristics of shear-horizontal-type surface acoustic wave on langasite with Au of Ta/sub 2/O/sub 5/ thin film," 2004.
[107] Y. Nakagawa and T. Okada, "Material constants of new piezoelectric Ta₂O₅ thin films," *Journal of Applied Physics*, vol. 68, pp. 556-9, 1990.
[108] A. Pham, A. Mathis, J. Laskar, A. F. Peterson, and L. Hayden, "Membrane probe technology for non-destructive thin-film material characterization," 1998.
[109] L. Li, T. Abe, and M. Esashi, "High sensitive, miniaturized plano-convex quartz crystal microbalance fabricated by reactive ion etching and melting photoresist," presented at TRANSDUCERS, Solid-State Sensors, Actuators and Microsystems, 12th International Conference on, 2003, 2003.

[110] Y. Hu, L. A. French, Jr., K. Radecsky, M. P. DaCunha, P. Millard, and J. F. Vetelino, "A lateral field excited liquid acoustic wave sensor," presented at 2003 IEEE Symposium on Ultrasonics, Orono, ME, USA, 2003.
[111] G. S. Ruff, A. Z. Wang, and W. D. Hunt, "Design and Development of Resonance Frequency Tracking Software Using LabVIEW," *The Journal of Young Investigators*, vol. 19, 2008.
[112] S. J. Updike and G. P. Hicks, "Enzyme Electrode," *Nature*, vol. 214, pp. 986-988, 1967.
[113] J. P. Chambers, B. P. Arulanandam, L. L. Matta, A. Weis, and J. J. Valdes, "Biosensor recognition elements," *Curr Issues Mol Biol*, vol. 10, pp. 1-12, 2008.
[114] H. P. Roost, M. F. Bachmann, A. Haag, U. Kalinke, V. Pliska, H. Hengartner, and R. M. Zinkernagel, "Early high-affinity neutralizing anti-viral IgG responses without further overall improvements of affinity," *Proceedings of the National Academy of Sciences of the United States of America*, vol. 92, pp. 1257-1261, 1995.
[115] C. Branden and J. Tooze, *Introduction to Protein Structure*, vol. 1, 2nd ed: Garland Science, 1999.
[116] G. M. Edelman, B. A. Cunningham, W. E. Gall, P. D. Gottlieb, U. Rutishauser, and M. J. Waxdal, "The covalent structure of an entire gammaG immunoglobulin molecule," *Proc Natl Acad Sci U S A*, vol. 63, pp. 78-85, 1969.
[117] S. K. Bhatia, L. C. Shriver-Lake, K. J. Prior, J. H. Georger, J. M. Calvert, R. Bredehorst, and F. S. Ligler, "Use of thiol-terminal silanes and heterobifunctional crosslinkers for immobilization of antibodies on silica surfaces," *Anal Biochem*, vol. 178, pp. 408-13, 1989.
[118] L. C. Shriver-Lake, B. Donner, R. Edelstein, K. Breslin, S. K. Bhatia, and F. S. Ligler, "Antibody immobilization using heterobifunctional crosslinkers," *Biosensors & Bioelectronics*, vol. 12, pp. 1101-1106, 1997.
[119] I. Luzinov, D. Julthongpiput, A. Liebmann-Vinson, T. Cregger, M. D. Foster, and V. V. Tsukruk, "Epoxy-terminated self-assembled monolayers: Molecular glues for polymer layers," *Langmuir*, vol. 16, pp. 504-516, 2000.
[120] V. V. Tsukruk, I. Luzinov, and D. Julthongpiput, "Sticky Molecular Surfaces: Epoxysilane Self-Assembled Monolayers," *Langmuir*, vol. 15, pp. 3029-3032, 1999.
[121] S. Krishnamoorthy, T. Bei, E. Zoumakis, G. P. Chrousos, and A. A. Iliadis, "Morphological and binding properties of interleukin-6 on thin ZnO films grown on (100) silicon substrates for biosensor applications," *Biosens Bioelectron*, vol. 22, pp. 707-14, 2006.
[122] S. D. Jayasena, "Aptamers: an emerging class of molecules that rival antibodies in diagnostics," *Clin Chem*, vol. 45, pp. 1628-50, 1999.
[123] T. Hermann and D. J. Patel, "Adaptive recognition by nucleic acid aptamers," *Science*, vol. 287, pp. 820-5, 2000.
[124] S. Spiegelman, "Ribonucleic acid. I. The test-tube synthesis of a viral nucleic acid. II. The development and use of molecular hybridization," *Jama*, vol. 230, pp. 1036-42, 1974.

[125] K. B. Mullis and F. A. Faloona, "Specific synthesis of DNA in vitro via a polymerase-catalyzed chain reaction," *Methods Enzymol*, vol. 155, pp. 335-50, 1987.
[126] A. D. Ellington and J. W. Szostak, "In vitro selection of RNA molecules that bind specific ligands," *Nature*, vol. 346, pp. 818-22, 1990.
[127] C. Tuerk and L. Gold, "Systematic evolution of ligands by exponential enrichment: RNA ligands to bacteriophage T4 DNA polymerase," *Science*, vol. 249, pp. 505-10, 1990.
[128] D. L. Robertson and G. F. Joyce, "Selection in vitro of an RNA enzyme that specifically cleaves single-stranded DNA," *Nature*, vol. 344, pp. 467-8, 1990.
[129] R. Stoltenburg, C. Reinemann, and B. Strehlitz, "SELEX--A (r)evolutionary method to generate high-affinity nucleic acid ligands," *Biomolecular Engineering*, vol. 24, pp. 381-403, 2007.
[130] Z. S. Wu, M. M. Guo, S. B. Zhang, C. R. Chen, J. H. Jiang, G. L. Shen, and R. Q. Yu, "Reusable Electrochemical Sensing Platform for Highly Sensitive Detection of Small Molecules Based on Structure-Switching Signaling Aptamers," *Anal. Chem.*, vol. 79, pp. 2933-2939, 2007.
[131] Y. Xiao, A. A. Lubin, A. J. Heeger, and K. W. Plaxco, "Label-free electronic detection of thrombin in blood serum by using an aptamer-based sensor," *Angewandte Chemie International Edition*, vol. 44, pp. 5456 - 5459, 2005.
[132] S. Balamurugan, A. Obubuafo, S. A. Soper, and D. A. Spivak, "Surface immobilization methods for aptamer diagnostic applications," *Analytical and Bioanalytical Chemistry*, vol. 390, pp. 1009-1021, 2008.
[133] C. D. Corso, A. Dickherber, and W. D. Hunt, "An investigation of antibody immobilization methods employing organosilanes on planar ZnO surfaces for biosensor applications," *Biosens Bioelectron*, 2008.
[134] L. Yang and Y. Li, "AFM and impedance spectroscopy characterization of the immobilization of antibodies on indium-tin oxide electrode through self-assembled monolayer of epoxysilane and their capture of Escherichia coli O157:H7," *Biosens Bioelectron*, vol. 20, pp. 1407-16, 2005.
[135] A. Tlili, A. Abdelghani, K. Aguir, M. Gillet, and N. Jaffrezic-Renault, "Adsorption characteristics of self-assembled thiol and dithiol layer on gold," *Materials Science & Engineering C-Biomimetic and Supramolecular Systems*, vol. 27, pp. 620-624, 2007.
[136] G. Gauglitz, "Direct optical sensors: principles and selected applications," *Analytical & Bioanalytical Chemistry*, vol. 381, pp. 141-155, 2005.
[137] A. Leung, P. M. Shankar, and R. Mutharasan, "A review of fiber-optic biosensors," *Sensors and Actuators B: Chemical*, vol. 125, pp. 688-703, 2007.
[138] G. Proll, L. Steinle, F. Proll, M. Kumpf, B. Moehrle, M. Mehlmann, and G. Gauglitz, "Potential of label-free detection in high-content-screening applications," *J Chromatogr A*, vol. 1161, pp. 2-8, 2007.
[139] N. P. Jonathan S. Daniels, "Label-Free Impedance Biosensors: Opportunities and Challenges," *Electroanalysis*, vol. 19, pp. 1239-1257, 2007.
[140] X. D. Wang, J. H. Song, and Z. L. Wang, "Nanowire and nanobelt arrays of zinc oxide from synthesis to properties and to novel devices," *Journal of Materials Chemistry*, vol. 17, pp. 711-720, 2007.

[141] M. A. Cooper and V. T. Singleton, "A survey of the 2001 to 2005 quartz crystal microbalance biosensor literature: applications of acoustic physics to the analysis of biomolecular interactions," *Journal of Molecular Recognition*, vol. 20, pp. 154-184, 2007.
[142] K. Lange, B. E. Rapp, and M. Rapp, "Surface acoustic wave biosensors: a review," *Anal Bioanal Chem*, 2008.
[143] R. Hassan, T. Bera, and I. Pastan, "Mesothelin: A New Target for Immunotherapy," *Clin Cancer Res*, vol. 10, pp. 3937-3942, 2004.
[144] K. Chang and I. Pastan, "Molecular cloning of mesothelin, a differentiation antigen present on mesothelium, mesotheliomas, and ovarian cancers," *Proceedings of the National Academy of Sciences of the United States of America*, vol. 93, pp. 136-140, 1996.
[145] T. K. Bera and I. Pastan, "Mesothelin Is Not Required for Normal Mouse Development or Reproduction," *Mol. Cell. Biol.*, vol. 20, pp. 2902-2906, 2000.
[146] M. Ho, M. Onda, Q. C. Wang, R. Hassan, I. Pastan, and M. O. Lively, "Mesothelin is shed from tumor cells," *Cancer Epidemiology Biomarkers & Prevention*, vol. 15, pp. 1751-1751, 2006.
[147] P. Argani, C. Iacobuzio-Donahue, B. Ryu, C. Rosty, M. Goggins, R. E. Wilentz, S. R. Murugesan, S. D. Leach, E. Jaffee, C. J. Yeo, J. L. Cameron, S. E. Kern, and R. H. Hruban, "Mesothelin is overexpressed in the vast majority of ductal adenocarcinomas of the pancreas: identification of a new pancreatic cancer marker by serial analysis of gene expression (SAGE)," *Clin Cancer Res*, vol. 7, pp. 3862-8, 2001.
[148] N. G. Ordonez, "Application of mesothelin immunostaining in tumor diagnosis," *Am J Surg Pathol*, vol. 27, pp. 1418-28, 2003.
[149] K. Chang, I. Pastan, and M. C. Willingham, "Frequent expression of the tumor antigen CAK1 in squamous-cell carcinomas," *Int J Cancer*, vol. 51, pp. 548-54, 1992.
[150] R. Hassan and M. Ho, "Mesothelin targeted cancer immunotherapy," *European Journal of Cancer*, vol. 44, pp. 46-53, 2008.
[151] R. Hassan, A. T. Remaley, M. L. Sampson, J. Zhang, D. D. Cox, J. Pingpank, R. Alexander, M. Willingham, I. Pastan, and M. Onda, "Detection and quantitation of serum mesothelin, a tumor marker for patients with mesothelioma and ovarian cancer," *Clin Cancer Res*, vol. 12, pp. 447-53, 2006.
[152] D. A. Armbruster, "Prostate-specific antigen: biochemistry, analytical methods, and clinical application," *Clin Chem*, vol. 39, pp. 181-195, 1993.
[153] M. B. Gretzer and A. W. Partin, "PSA Levels and the Probability of Prostate Cancer on Biopsy," *European Urology Supplements*, vol. 1, pp. 21-27, 2002.
[154] I. M. T. Javier Hernández, "Prostate-specific antigen: A review of the validation of the most commonly used cancer biomarker," *Cancer*, vol. 101, pp. 894-904, 2004.
[155] I. M. Thompson, D. P. Ankerst, C. Chi, P. J. Goodman, C. M. Tangen, M. S. Lucia, Z. Feng, H. L. Parnes, and C. A. Coltman, Jr., "Assessing prostate cancer risk: results from the Prostate Cancer Prevention Trial," *J Natl Cancer Inst*, vol. 98, pp. 529-34, 2006.

[156] B. Djavan, A. Zlotta, C. Kratzik, M. Remzi, C. Seitz, C. C. Schulman, and M. Marberger, "PSA, PSA density, PSA density of transition zone, free/total PSA ratio, and PSA velocity for early detection of prostate cancer in men with serum PSA 2.5 to 4.0 L," *Urology*, vol. 54, pp. 517-522, 1999.

[157] S. Berry, D. Coffey, P. Walsh, and L. Ewing, "The Development of human benign prostatic hyperplasia with age," *Journal of Urology*, vol. 132, pp. 474-479, 1984.

[158] H. B. Carter, C. H. Morrell, J. D. Pearson, L. J. Brant, C. C. Plato, E. J. Metter, D. W. Chan, J. L. Fozard, and P. C. Walsh, "Estimation of Prostatic Growth Using Serial Prostate-specific Antigen Measurements in Men with and without Prostate Disease," *Cancer Res*, vol. 52, pp. 3323-3328, 1992.

[159] S. Loeb, K. A. Roehl, W. J. Catalona, and R. B. Nadler, "Prostate Specific Antigen Velocity Threshold for Predicting Prostate Cancer in Young Men," *The Journal of Urology*, vol. 177, pp. 899-902, 2007.

[160] H. B. Carter, D. W. Chan, J. D. Pearson, H. A. Guess, Z. Waclawiw, P. C. Walsh, and E. J. Metter, "Prostate-specific antigen variability in men without prostate cancer: effect of sampling interval on prostate-specific antigen velocity," *Urology*, vol. 45, pp. 591-596, 1995.

[161] O. Gustafsson, E. Mansour, U. Norming, A. Carlsson, M. TÃ¶rnblom, and C. R. Nyman, "Prostate-specific Antigen (PSA), PSA Density and Age-adjusted PSA Reference Values in Screening for Prostate Cancer: A Study of a Randomly Selected Population of 2,400 Men," *Scandinavian Journal of Urology and Nephrology*, vol. 32, pp. 373 - 377, 1998.

[162] M. Benson, I. Whang, C. Olsson, D. McMahon, and W. Cooner, "The use of prostate specific antigen density to enhance the predictive value of intermediate levels of serum prostate specific antigen," *Journal of Urology*, vol. 147, pp. 817-821, 1992.

[163] W. J. Catalona, J. A. Beiser, and D. S. Smith, "SERUM FREE PROSTATE SPECIFIC ANTIGEN AND PROSTATE SPECIFIC ANTIGEN DENSITY MEASUREMENTS FOR PREDICTING CANCER IN MEN WITH PRIOR NEGATIVE PROSTATIC BIOPSIES," *The Journal of Urology*, vol. 158, pp. 2162-2167, 1997.

[164] E. S. Leman, G. W. Cannon, B. J. Trock, L. J. Sokoll, D. W. Chan, L. Mangold, A. W. Partin, and R. H. Getzenberg, "EPCA-2: A Highly Specific Serum Marker for Prostate Cancer," *Urology*, vol. 69, pp. 714-720, 2007.

[165] N. Hara, T. Kasahara, T. Kawasaki, V. Bilim, K. Obara, K. Takahashi, and Y. Tomita, "Reverse transcription-polymerase chain reaction detection of prostate-specific antigen, prostate-specific membrane antigen, and prostate stem cell antigen in one milliliter of peripheral blood: value for the staging of prostate cancer," *Clin Cancer Res*, vol. 8, pp. 1794-9, 2002.

[166] R. E. Reiter, I. Sato, G. Thomas, J. Qian, Z. Gu, T. Watabe, M. Loda, and R. B. Jenkins, "Coamplification of prostate stem cell antigen (PSCA) and MYC in locally advanced prostate cancer," *Genes Chromosomes Cancer*, vol. 27, pp. 95-103, 2000.

[167] M. A. Rubin, M. Zhou, S. M. Dhanasekaran, S. Varambally, T. R. Barrette, M. G. Sanda, K. J. Pienta, D. Ghosh, and A. M. Chinnaiyan, "alpha-Methylacyl

coenzyme A racemase as a tissue biomarker for prostate cancer," *Jama*, vol. 287, pp. 1662-70, 2002.
[168] S. V. Harden, H. Sanderson, S. N. Goodman, A. A. W. Partin, P. C. Walsh, J. I. Epstein, and D. Sidransky, "Quantitative GSTP1 Methylation and the Detection of Prostate Adenocarcinoma in Sextant Biopsies," *J. Natl. Cancer Inst.*, vol. 95, pp. 1634-1637, 2003.
[169] W. H. Lee, R. A. Morton, J. I. Epstein, J. D. Brooks, P. A. Campbell, G. S. Bova, W. S. Hsieh, W. B. Isaacs, and W. G. Nelson, "Cytidine methylation of regulatory sequences near the pi-class glutathione S-transferase gene accompanies human prostatic carcinogenesis," *Proc Natl Acad Sci U S A*, vol. 91, pp. 11733-7, 1994.
[170] W. H. Lee, W. B. Isaacs, G. S. Bova, and W. G. Nelson, "CG island methylation changes near the GSTP1 gene in prostatic carcinoma cells detected using the polymerase chain reaction: a new prostate cancer biomarker," *Cancer Epidemiol Biomarkers Prev*, vol. 6, pp. 443-50, 1997.
[171] J. B. de Kok, G. W. Verhaegh, R. W. Roelofs, D. Hessels, L. A. Kiemeney, T. W. Aalders, D. W. Swinkels, and J. A. Schalken, "DD3PCA3, a Very Sensitive and Specific Marker to Detect Prostate Tumors," *Cancer Res*, vol. 62, pp. 2695-2698, 2002.
[172] M. J. G. Bussemakers, A. van Bokhoven, G. W. Verhaegh, F. P. Smit, H. F. M. Karthaus, J. A. Schalken, F. M. J. Debruyne, N. Ru, and W. B. Isaacs, "DD3::A New Prostate-specific Gene, Highly Overexpressed in Prostate Cancer," *Cancer Res*, vol. 59, pp. 5975-5979, 1999.
[173] C. Stephan, K. Jung, M. Lein, P. Sinha, D. Schnorr, and S. A. Loening, "Molecular forms of prostate-specific antigen and human kallikrein 2 as promising tools for early diagnosis of prostate cancer," *Cancer Epidemiol Biomarkers Prev*, vol. 9, pp. 1133-47, 2000.
[174] C. Stephan, K. Jung, T. Nakamura, G. M. Yousef, G. Kristiansen, and E. P. Diamandis, "Serum human glandular kallikrein 2 (hK2) for distinguishing stage and grade of prostate cancer," *Int J Urol*, vol. 13, pp. 238-43, 2006.
[175] J. A. Magee, T. Araki, S. Patil, T. Ehrig, L. True, P. A. Humphrey, W. J. Catalona, M. A. Watson, and J. Milbrandt, "Expression Profiling Reveals Hepsin Overexpression in Prostate Cancer," *Cancer Res*, vol. 61, pp. 5692-5696, 2001.
[176] C. Stephan, G. M. Yousef, A. Scorilas, K. Jung, M. Jung, G. Kristiansen, S. Hauptmann, T. Kishi, T. Nakamura, S. A. Loening, and E. P. Diamandis, "Hepsin is highly over expressed in and a new candidate for a prognostic indicator in prostate cancer," *J Urol*, vol. 171, pp. 187-91, 2004.
[177] T. Steuber, M. F. O'Brien, and H. Lilja, "Serum Markers for Prostate Cancer: A Rational Approach to the Literature," *European Urology*, vol. 54, pp. 31-40, 2008.
[178] M. Onda, M. Willingham, S. Nagata, T. K. Bera, R. Beers, M. Ho, R. Hassan, R. J. Kreitman, and I. Pastan, "New monoclonal antibodies to mesothelin useful for immunohistochemistry, fluorescence-activated cell sorting, Western blotting, and ELISA," *Clin Cancer Res*, vol. 11, pp. 5840-6, 2005.
[179] C. D. Corso, A. Dickherber, P. Shah, A. Migdal, M. W. Datta, S. Datta, and W. D. Hunt, "Development of a simple inexpensive bulk acoustic wave nanosensor for

cancer biomarkers: Detection of secreted sonic hedgehog from prostate cancer cells," presented at 2006 Annual Meeting of the AACR, Washington D.C., 2006.
[180] J. r. Janata, *Principles of chemical sensors*. New York: Plenum Press, 1989.

VITA

ANTHONY J. DICKHERBER

Anthony Dickherber was born in Fairfax, Virginia. As the son of a foreign service officer, he grew up attending international schools in Tunisia, Pakistan and the Philippines. He received his B.S. and M.S. in Electrical & Computer Engineering from Georgia Institute of Technology in 1999 and 2002, respectively, in Atlanta, GA. He worked for 4 years as a communications research engineer for the Georgia Tech Research Institute before deciding to return to pursue his doctoral degree in bioengineering. While at Georgia Tech, he received a US Army Medical Research & Materiel Command Prostate Cancer Research Program Pre-doctoral Training Award, the Sam Nunn Security Program Pre-Doctoral Fellowship and a graduate certificate in Public Policy. He also served as director of the Bioscience & Bioengineering Unified Graduate Student Group, chair of the Biotechnology Technology Forum, and as an inaugural member of the Bioengineering Graduate Student Advisory Committee.